Charles University in Prague
Faculty of Mathematics and Physics

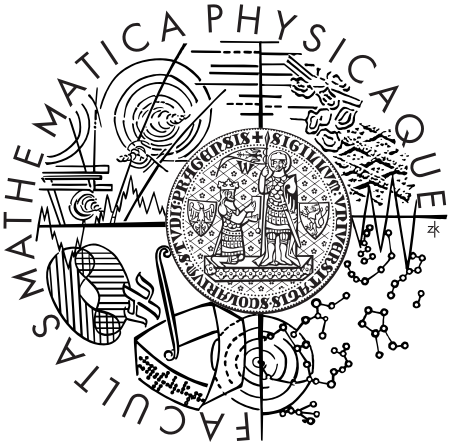

NUMERICAL MODELLING OF THE MANTLE WEDGE

Martin Kukačka

Prague, 2008

Supervisor: doc. RNDr. Ctirad Matyska, DrSc.

This research has been carried out at:

Department of Geophysics
Faculty of Mathematics and Physics
V Holešovičkách 2
180 00 Praha 8
Czech Republic

Author's e-mail address: *martin.kukacka@mff.cuni.cz*

Missprints corrected 6. 10. 2008.

Contents

Used Notation

α	thermal expansion coefficient
c_p	specific heat at constant pressure
$\boldsymbol{D}$	deviatoric part of stress tensor
$\dot{\boldsymbol{e}}$	strain tensor
η	dynamic viscosity
$\boldsymbol{g}$	gravity acceleration
k	thermal conductivity
κ	thermal diffusivity
Q	heat
p	pressure
ρ	density
σ	second invariant of deviatoric stress tensor
t	time
T	temperature
$\boldsymbol{\tau}$	stress tensor
$\boldsymbol{v}$	velocity
$\boldsymbol{I}$	identity tensor δ_{ij}
$\boldsymbol{n}$	normal vector
L^2	Lebesgue space of functions for which $\int_\Omega \lvert v\rvert^2 \mathrm{d}\Omega$ is finite
∇	gradient
$\nabla\cdot$	divergence
Ω	domain
$\partial\Omega$	domain boundary
:	total scalar product $\boldsymbol{x} : \boldsymbol{y} = x_{ij}y_{ij}$

Chapter 1

Introduction

Subduction zones are regions where the oceanic crust and the upper part of the oceanic lithosphere return to the Earth's mantle. These zones are known as convergent boundaries of the lithospheric plates and together with the oceanic ridges, the divergent boundaries, are the fundamental features of the Earth's surface. In the last decades, a lot of effort has been made to understand the processes shaping the Earth and its surface but there are still large unknowns. Nowadays, we generally do understand that the Earth's surface is perpetually moving, however, particular effects and observations are still waiting for a much better understanding. Particularly, the computer modelling shed more light on the convection in the Earth's mantle and processes in the subduction zones are often referred as a subduction factory (Eiler, 2003).

1.1 Plate Tectonics

Although the plate tectonics is a relatively new scientific discipline introduced in early 1960s, the idea that the continents have not always been fixed in their positions was first suggested by Abraham Ortelius (1537 – 1598), the Dutch cartographer, in 1596. Ortelius, the author of the first modern atlas Thesaurus Geographicus, suggested that America was torn away from Europe and Africa by earthquakes and floods because he simply noticed the remarkable coincidence of the coastlines of these three continents.

Later, the idea was reused by Antonio Snider-Pellegrini, who concluded that the separation of America from Europe was caused by the Great Flood (Snider-Pellegrini, 1858). He believed that native Americans are direct descendants of Adam and Eve, while all others are descendants of Noah.

However, the first geoscientist, who had been fighting for the concept of moving continents for all his life, was Alfred Wegener, the German meteorologist. Wegener (1929) considered not only the fit of continent margins but also a whole bunch of facts such as the apparent wandering of the magnetic poles, the discovery of fossils and their distribution, and the similar sequence of rocks at different locations. His theory of the continental drift stated that the continents simply plough through the oceanic floor. The significant

weakness of the proposed theory was the lack of moving force. Wegener believed that the Earth's rotation forces the continents to move and as they plough through the ocean, they produce mountains on their edges.

This theory was not widely accepted and Wegener became famous mainly by his expeditions to Greenland. The last one, in 1930, celebrated the scientific success because the Wegener's group successfully measured the thickness of the ice sheet over the Greenland, but was fatal for its leader: Wegener froze to death on April 1, 1930, while returning to the base camp on the west coast of Greenland. Shortly after his death new evidences supporting the idea of the movable Earth's surface appeared and that is why Wegener is regarded as the pioneer of the plate tectonic theory despite his wrong explanation of the movement source.

The first one suggesting the right explanation was Arthur Holmes, the Scottish geologist, presenting the idea of convective cells in which convective currents of rocks rise beneath the crust, cool down, and fall back into the Earth's mantle (Holmes, 1945). Currently, the theory of plate tectonics, which is widely accepted, provides the same explanation of the processes near the Earth's surface. This theory states that the Earth's surface is broken into several plates which move relatively to each other. Their movement is a consequence of the thermal convection in the Earth's mantle. There are several major developments which plate tectonics is based on:

- Polar reversals and sea-floor spreading: When magma cools and solid volcanic rocks are formed, the Earth's magnetic orientation shapes the orientation of magnetic minerals inside the rocks. In the beginning of 1960s, it was recognized that the oceanic floor, whose main portion is iron-rich basalt composed of a strongly magnetic mineral magnetite, is divided into strips of normal and reversal magnetic orientation that are parallel with mid-ocean rifts (Vine and Matthews, 1963). The term sea-floor spreading was introduced by Dietz (1961).

- The age of the oceanic crust: No older than 200 million years oceanic crust was reported. The sedimentary layer is very thin. If the oceanic floor were four milliard years old as was thought originally, the layer of sediments would be much thicker.

- Concentration of deep earthquakes: In stable continental regions, the seismicity is limited to the crust, the uppermost layer of the Earth, mostly to the uppermost 20 km (Stern, 2002). Deep earthquakes are concentrated in distinct zones that begin at ocean trenches and incline landward and downward into the Earth. These zones, which may extent up to depths of 700 km, are known as Wadati-Benioff zones (see Figure 1.1) since they were named in honour of two seismologists who discovered them (Wadati, 1935; Benioff, 1954).

These findings together with all the other pieces of knowledge not mentioned in this brief introduction contributed to recognize the importance of mid-ocean ridges in the process of sea-floor spreading. The plate tectonic theory states that the oceanic crust and a part of the upper mantle is created at mid-oceanic ridges and consumed in so-called subduction zones at trenches.

Some questions of plate tectonics, however, remain to be explained (Jacoby, 2001). The objections against plate tectonics were summarized by Pratt (2000). One of mysteries, which have not been explained yet, is an increase in observed surface heat flow in backarc regions. As pointed by Uyeda (1986), it is hard to understand how the subduction of a cold slab could result in zones of high surface heat flow in backarc regions, which extend to several hundreds kilometres (Hyndman et al., 2005) and any satisfactory numerical model reproducing a similar pattern in surface heat flow has not been built yet (Currie et al., 2004b). Another mystery is exhumation of rocks from great depths (sometimes exceeding 100 km). Although several explanations have been proposed (Platt, 1993), none of them explains this phenomenon in all details, and exhumation processes are therefore extensively studied by numerical simulations (Gerya et al., 2002). Surprisingly, also the key parameter affecting the slope of Wadati-Benioff zones has not been identified yet and thus the reason for different dips observed in different subduction zone is waiting for clear explanation (Cruciani et al., 2005) and the numerical modelling likely will give the answer in the near feature (Manea and Gurnis, 2007).

1.2 Outline of the Thesis

Since direct measurements in a deep interior of the Earth are not possible[1], numerical modelling is employed in order to understand how "the subduction factory works". In recent years, a number of numerical models has increased and both dynamic and kinematic models are in use. A fundamental problem in both types of model is how to describe a contact between the subducting slab and the overriding lithosphere. Obviously, the contact plays an important (perhaps decisive) role in the subduction process but all current numerical models handle it rather artificially – usually the geometry of the subducting slab is prescribed either in the whole model domain (kinematic models) or in shallow depths (by prescribing a fault in dynamic models). In this way, a part of the flow field is imposed to the results a priori, but the position of the contact should be rather an outcome of the numerical simulations.

The aim of this study is to formulate a numerical model of a generic subduction zone in which the contact would be modelled in a more consistent way. Such a model might be used to find a rheology, which would produce sinking lithospheric plates naturally, without any a priory information about the position of the contact. The self-consistent formation of the subduction zones is important, although shapes of the subducting plates are well known from seismic measurements, since non-symmetric downwelling observed in the Earth's interior is the main difference of the thermal convection in the Earth from a classical Rayleigh-Bernard convection (King, 2001). The fact that actual shapes of the subducting plates are relatively well determined by seismic tomography may be utilized to validate numerical models a posteriori.

[1]Most direct observations of a flow in the deeper interior are provided by seismic tomography (van der Hilst et al., 1997).

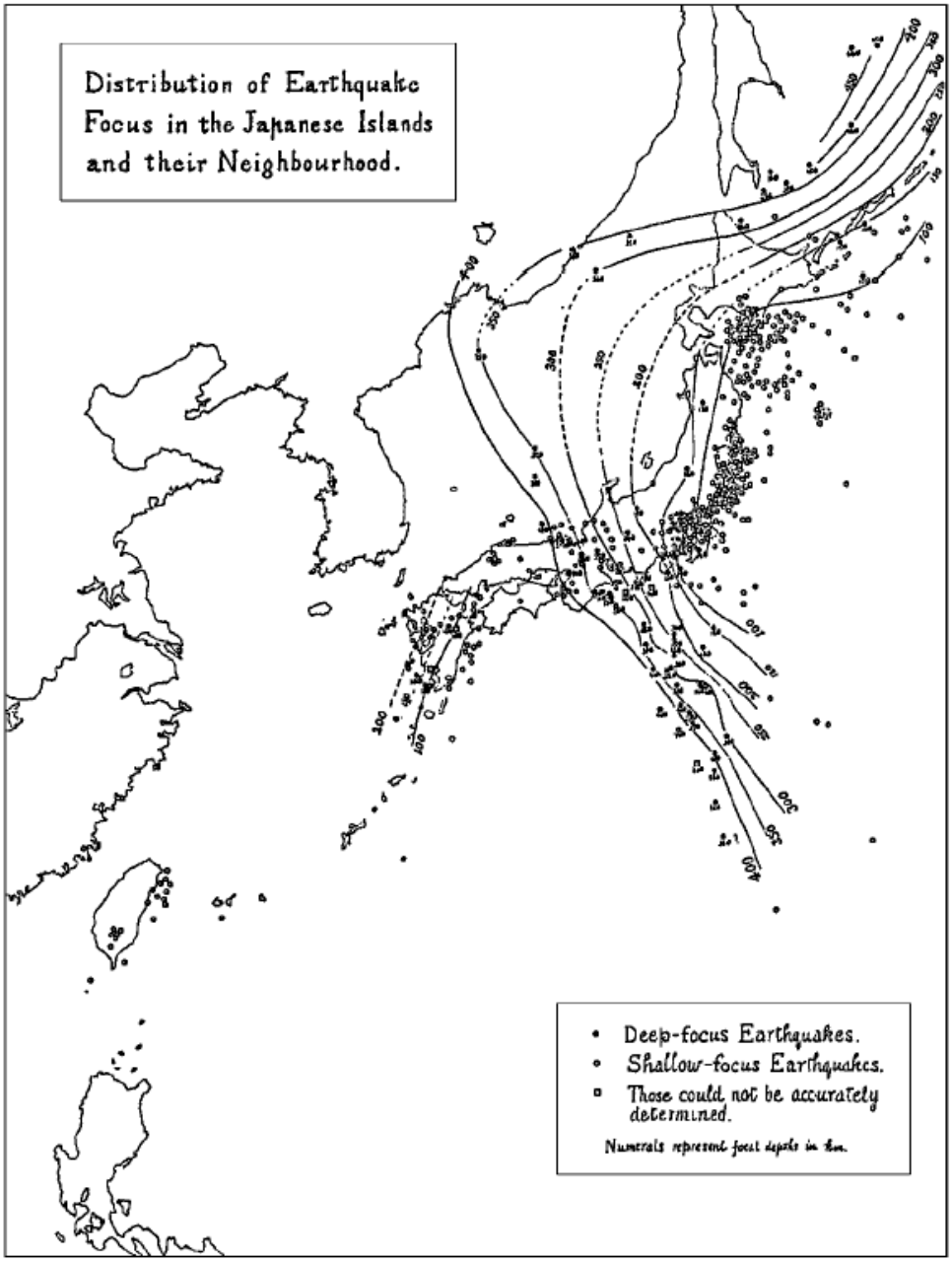

Figure 1.1: The distribution of earthquakes and lines of equal focal depth for intermediate and deep earthquakes in the Japan islands according to Wadati (1935); based on 62 deep and 28 intermediate events recorded between 1924 and 1934.

Chapter 2

Subduction

Subduction[1] is one of the most studied processes in plate tectonics as it plays a key role in the plate tectonics theory. Generally, the idea of a subducting slab, which is plunged under an overriding plate, is widely accepted, but the mechanism how these two plates interact together has not been understood yet in details. There are a lot of observations that may be used to construct and validate subduction models; however, different data are of different importance and credibility. The most important data that constraint subduction models are reviewed in the next sections.

2.1 Subduction Zone Geometry

Subduction zones are convergent plate boundaries where the oceanic lithosphere sinks into the mantle. It is believed that the primary source of the movement is negative buoyancy of the subducting oceanic plates. This force presumably drives the whole mantle convection, and therefore, the term *slab pull* was introduced by Forsyth and Uyeda (1975). For most subducting plates observed velocities are between 5 and 13 cm/year (Jarrad, 1986), however, slower (e.g. convergence rate 2 cm/year at Lesser Antilles) as well as much faster (24 cm/year at northern part of Tonga arc (Bevis et al., 1995)) subducting plates have been reported.

The dip angle, under which the subducting oceanic plate sinks into the mantle, is derived from the slope of Wadati-Benioff zone. Typically, the subduction zone exhibits two different dip angles: smaller at a shallow portion and bigger at greater depths. An upper zone with an average dip of 33° extends to depths of $70 - 100$ km, and a lower zone with an average dip about 60° extends up to 700 km (Benioff, 1954). In some cases (e.g. Nazca plate descending beneath central and northern Peru), the dip angle in shallow depths is as small as 10° (Barazangi and Isacks, 1979). According to Jarrad (1986), there is a significant difference in the average deep dip angle (derived from the slope of Wadati-

[1]The term "subduction" was used for the first time by the Swiss geologist Andre Amstutz, who studied geological settings in the Alps, in 1951 in order to name an abrupt descent of lithosphere (*sub*=under, *ducere*=to pull).

Benioff zones in depths between 100 and 400 km) in the case that the overriding plate is either a continental plate (average dip 40°) or an oceanic one (66°).

Even if Jarrad (1986) concluded there is a lack of significant statistical correlations between the deep slab dip angle and many different subduction parameters, including its age and convergence rate, he found that the strain regime in the overlying mantle seems to be correlated with the age of subducting lithosphere and divided subduction zones into several classes. The end members, strongly extensional subduction and strongly compressional subduction, represent subduction of old (so-called Mariana type), respectively young (so-called Chilean type) lithosphere. Chilean type of subduction is characterized by shallower dip angles, while Mariana type subduction plates sink under steeper dip angles. The difference is explained by the fact that the older lithosphere is colder and denser[2] than the underlying asthenosphere and therefore sinks readily (Cloos, 1993). Unlike that, the young lithosphere is less dense and resists to subduction.[3] The lack of clear correlation among observed dip angles, slab age, and convergence rates has been confirmed recently and therefore it was supposed that forces supplemental to the negative buoyancy of the slab should play a role (Cruciani et al., 2005).

The difference in the observed subduction dip angles is sometimes referred as a difference between eastward and westward dipping (Marotta and Mongelli, 1998; Doglioni et al., 1999). This feature is remarkable particularly in Pacific, where west-oriented subduction zones (e.g. Tonga-Kermadec, Mariana, New Hebrides) are steeper and deeper (down to 670 km), whereas east-directed subduction zones (North Chile, Peru) are considerably less steep and shallow. The relation between the average deep dip and the direction of subduction might be explained by the global westward motion of the lithosphere with respect to the underlying mantle[4] (Čadek and Ricard, 1992), the effect which is not fully understood but seems to be significant (Ricard et al., 1991). Although this phenomenon could be true, King (2001) emphasized that it is not easy to separate the effect of dip direction from other factors mainly because many of eastward dipping subducting plates are being overridden by continental plates.

The basic idea of a shallow portion of subduction zones is illustrated in Figure 2.1. Close to the sinking slab, there is a volcanic front, which is located where the slab reaches depths of about 100 km (Gill, 1981; England et al., 2004). The location of volcanic front is similar in many subduction zones[5] and is tightly correlated with the existence of an aseismic gap in these depths (Hanuš and Vaněk, 1985). Although the spatial correlation of the aseismic

[2]Density contrast between 80 million years old oceanic lithosphere capped by a 7-km thick basaltic crust and the asthenosphere is about 40 kg/m^3. Additionally, the subduction zone metamorphism transforms the basaltic crust to denser eclogite, so if the eclogite formation is extensive, the density contrast may increase up to 80 kg/m^3.

[3]The youngest lithosphere which is denser than the underlying asthenosphere is about 10 million years old. It is therefore likely that very young subducting plates are not driven by the negative buoyancy (King, 2001).

[4]The sum of plate motion vectors in the hot spot reference frame exhibits westward component about 2 cm/year.

[5]The depth of the slab beneath volcanoes is 124 ± 38 km according to Gill (1981), and Tatsumi (1986) gave a quite similar value 110 ± 38 km.

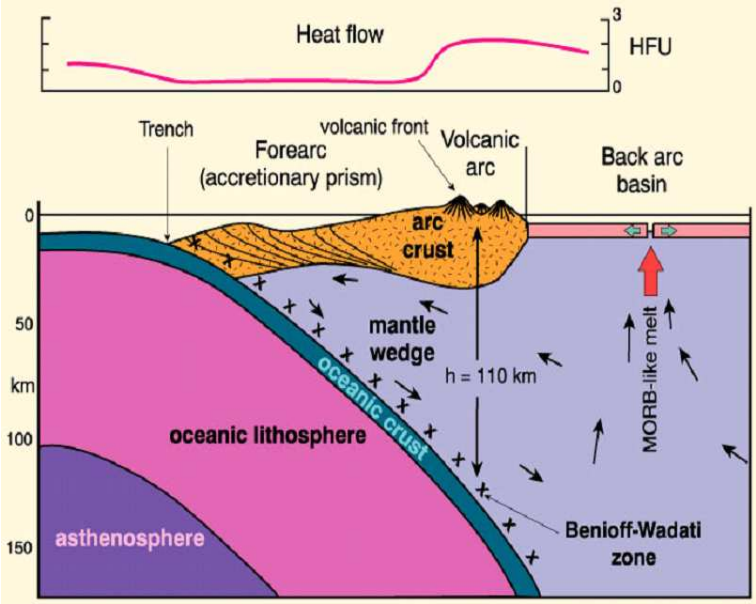

Figure 2.1: Schematic cross section through a typical island arc after Gill (1981), HFU means heat flow unit; 1 HFU = 41.9 mWm^{-2} (= 1 μcalcm^{-2}s^{-1}).

gap and the calc-alkaline volcanism was recognized[6] longer time ago (Hanuš and Vaněk, 1978; Gill, 1981), the exact processes of magma formation and particularly its transport remain still contentious (van Keken, 2003). The current view is that it is controlled by dehydration processes and partial melting in the slab and the adjacent wedge and the recent studies on dihedral angle[7] seem to explain why the magma may be formed at these depths (Mibe et al., 1999; Ono et al., 2002). The region between the trench and the volcanic front is referred as a forearc[8], while the region behind the volcanic front is called backarc.

2.2 Other Observations

A number of different observations about subduction zones is known (Stern, 2002) and it might be hard to judge which are global characteristics and which are local effects not so important in the global understanding of the subduction process. Here it is reviewed what seems to be important in order to construct a reasonable numerical model of the

[6]The aseismic gap, i.e. the part of the subducted slab, where no teleseismically recorded earthquakes (with magnitude greater than 4.0) are localized, is interpreted as a partially melted zone (Špičák et al, 2004).

[7]The water released from the hydrous minerals in the subducted oceanic crust is trapped in junctions between grains and efficient percolation is possible only if the angle at the triple junctions, so-called dihedral angle, is less than 60°. The dihedral angle depends on the pressure and the critical value is reached at pressures $3 - 5$ GPa.

[8]Usually a depression filled with sediments.

subducting slab and the adjacent mantle wedge.

2.2.1 Seismic Tomography

The seismic tomography is a quite young method which helps to gain an insight into the seismic velocity structure of the Earth mantle for about 25 years. In almost all major subduction zones, the tomographic inversions have revealed $100 - 200$ km thick plates of increased seismic velocities (Bijwaard et al., 1998). Some of them sink into the lower mantle although they do not seem to reach the mantle core boundary (van der Hilst et al., 1997). The shape of subduction plates may be complex in some cases; e.g. flattening of the Tonga subduction plate has been observed at 670 km discontinuity (van der Hilst, 1995). The increase in P-wave velocity is up to +6% (Zhao et al., 1997; Zhao and Kayal, 2000). Simultaneously it was revealed that the overlying regions usually exhibit decrease in P-wave velocity up to -6%. These low velocity zones are visible beneath the active volcanoes and extend to depths of $150 - 200$ km in the mantle wedge (see Figure 2.2). The zones of low seismic velocities in the wedge are assumed to be a general seismological feature of all subduction zones which is related to volcanism (Zhao et al., 1994).

The similar patterns may be observed also in seismic attenuation:[9] most of slabs and forearcs exhibit a high Q factor, while mantle wedges beneath the volcanic front exhibit a low Q factor (Schurr et al., 2003; Stachnik, 2004; Abers et al., 2006). This is in a good agreement with the older findings, since low Q factors in backarcs is a phenomenon known from the beginning of the plate tectonics (Oliver and Isacks, 1967; Baranzagi et al., 1973).

The results of seismic tomography may be used to infer some more information about temperatures and material properties of the lithosphere. The attenuation factor Q for different frequencies ω may be expressed as

$$\frac{1}{Q} \sim \omega^{\alpha} \exp\left(\frac{-\alpha H}{RT}\right), \tag{2.1}$$

where H is the activation enthalpy, T is the temperature, R is the gas constant, and α is a constant. The viscosity of rocks is thermally activated and exhibits similar Arrhenius dependence on the temperature (see Section 2.3 for details)

$$\eta \sim \eta_0 \exp\left(\frac{H}{RT}\right), \tag{2.2}$$

and thus, the relation between the attenuation and the viscosity is

$$\frac{\eta}{\eta_0} = \left(\frac{Q}{Q_0}\right)^{\frac{1}{\alpha}}, \tag{2.3}$$

[9] Anelasticity in minerals in expressed in term of so-called quality factor Q which is defined as a ratio of the elastic energy stored in the system and the energy loss per unit cycle $Q^{-1} = \Delta E/2\pi E$ (Aki and Richards, 1980). A low Q implies high attenuation of seismic waves.

where $\alpha = 0.23$ is determined from observations and experiments (Karato and Spetzler, 1990).

While the global average value of the quality factor Q_0 in the asthenosphere is about 200 (Dziewonski and Anderson, 1981), values of Q factor in mantle wedge (for P waves) are between 70 and 150 (Barazangi and Isacks, 1971), which according to equation (2.3) gives a decrease in the viscosity in the wedge to $0.01 - 0.28$ of the reference viscosity in the asthenosphere. Since a change in Q affects also the seismic velocities, the relation between seismic wave velocity, Q factor, and viscosity may be expressed (Karato, 2003) in the form

$$\frac{\delta V}{V_0} \cong \frac{ART_0^2}{H} \log \frac{\eta}{\eta_0} - \frac{F}{Q_0} \left(\left(\frac{\eta_0}{\eta} \right)^{\alpha} - 1 \right), \qquad F = \frac{1}{2} \cot \left(\frac{\pi \alpha}{2} \right), \tag{2.4}$$

where δV is a deviation in seismic velocity V_0 and A is a constant. This relation predicts a decrease in the viscosity of the mantle wedge from 0.02 (if $\delta V/V_0 = 0.02$) to 0.0008 ($\delta V/V_0 = 0.05$) of the reference viscosity. Therefore, the seismic tomography results are interpreted as clear evidence of a substantial viscosity decrease in the mantle wedge beneath backarcs (Karato, 2003; Billen and Gurnis, 2001). Because the tomography of P wave velocity is more accurate than the tomography of attenuation factor Q, it is supposed that the viscosity decrease is more likely three or four orders.

The quality of the tomographic inversions greatly improves if the boundaries with high velocity contrasts such as the Moho discontinuity[10] are included into the model a priory. In recent inversions (Koulakov et al., 2006), the additional information, such as temperature in the slab and the mantle wedge and the composition given by mineral physics, are also taken into account. These additional constraints together with the starting model of seismic velocities are of crucial importance due to principal non-uniqueness of the inversion problems.

2.2.2 Seismic Wave Anisotropy

In many subduction zones, the anisotropy of shear waves[11] has been observed, e.g. beneath Chile (Bock et al., 1998), Japan (Long and van der Hilst, 2005), Oregon (Currie et al., 2004a), and Kamchatka (Peyton et al., 2001). Iidaka and Obara (1995) reported that the anisotropic zone under Japan is located in the mantle wedge above the surface of the subducting slab and corresponds to the low-Q zone obtained from the seismic tomography. The pattern of anisotropy is diverse: In Tonga and Izu-Bonin, the fast directions are roughly parallel to the motion of the Pacific plate; however, in Japan Sea and western

[10] Zhao et al. (1994) used the Conrad and the Moho discontinuities whose positions were determined from shallow earthquakes and the upper boundary of the subducting plate, which was in this case assumed to be a very sharp discontinuity (Zhao and Hasegawa, 1993).

[11] A shear wave passing though an anisotropic body splits into two components which travel at different velocities. The splitting is characterized by the polarization direction of the shear wave arriving first (known as fast direction) and the time delay between the two shear waves. Usually S phases from local earthquakes and teleseismic core phases like SKS or PKS are used in analysis of anisotropy in subduction regions.

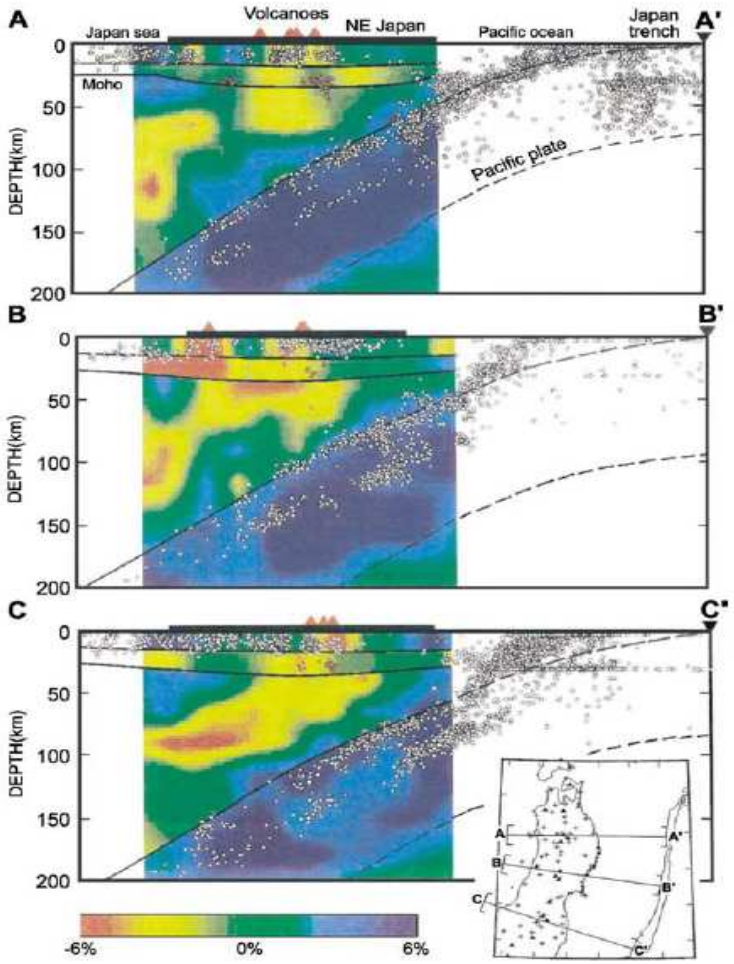

Figure 2.2: Cross-sections of P wave velocity distribution under the Japan islands according Zhao (2001). Circles indicate earthquakes that occurred within a 40 km width along the profile, triangles indicate active volcanoes. Thick lines indicate the boundaries between different domains used as a priory constraints in the tomographic inversion.

Honsu, the fast direction axis is approximately parallel to the trench (Fischer et al., 1998), which is also observed at Nazca plate (Bock et al., 1998). Moreover, detailed studies have revealed a complex anisotropy structure under Japan where the fast direction changes from the trench-parallel (close to the trench) to subduction parallel far away from the trench (Nakajima and Hasegawa, 2004; Long and van der Hilst, 2005).

The complex anisotropy structure in subducting regions cannot be easily explained and, particularly, the trench-parallel fast direction is still a puzzling question. At least three different explanations were proposed: Iidaka and Obara (1995) explained the trench-parallel fast direction as a consequence of melt-filled cracks in the mantle wedge.[12] The

[12]This type of anisotropy is caused by the lens like shape of cracks filled by fluid and is referred as SPO,

other two explanations deal with *lattice preferred orientation*[13] (LPO). Zhang and Karato (1995) found that olivine LPO is such that under large strains *a*-axis (the seismically fast direction) tends to align the flow direction (unlike that, under low and moderate strains *a*-axis aligns parallel to the direction of maximum extension and that is why subduction-parallel fast directions are not so surprising) and consequently, it was concluded that the flow in the mantle wedge must be more complex than a simple subduction-induced two-dimensional corner flow. Russo and Silver (1994) investigated the anisotropy under the Nazca plate, where the plate motion is almost parallel to the trench and where trench-parallel fast directions are observed, and suggested there must be a lateral flow around whole South America. Although such a trench-parallel flow has been simulated in physical analogue model (Buttles and Olson, 1998), the lack of evidence for such a flow has been reported in the particular case of South America (Helffrich et al., 2002). Finally, third possible explanation is based on the most recent results of LPO research: Several new types of LPO in olivine have been identified (Jung at al, 2006). One of them, so-called B-type olivine, may explain trench-parallel splitting with a simple 2-D flow in the wedge, since in this fabric, the seismically fast direction is normal to the flow plane. B-type olivine fabric is stable under conditions (low temperatures, high shear stress, and sufficient hydration) that have been predicted in the cold nose of the mantle wedge by numerical modelling (Kneller et al., 2005; Lassak et al., 2006; Kneller et al., 2007) and has been also documented in natural peridotite samples (Mizukami et al., 2004). On the other hand, the 3-D modelling has shown that the variations of anisotropy in Mariana and Chilean subduction zones may be a consequence of significant three-dimensional flow (Kneller and van Keken, 2007), so actually the explanation of anisotropy variations in subduction regions is not clear and the real source is likely a mixture of all effects (Long and van der Hilst, 2006).

2.2.3 Surface Heat Flow

An important quantity, which needs to be used to constrain numerical models of the mantle wedge, is surface heat flow since it is a direct measurable manifestation of the temperature state of the lithosphere. In the oceanic lithosphere, the highest surface heat flow is at the mid-ocean ridges and it decreases with increasing age of the lithosphere. The simplest possible mathematical model, the half space model, tries to explain the cooling of the lithosphere. The surface heat flow is roughly inversely proportional to the square root of lithospheric age (Le Pichon et al., 1973), however, this observation is valid just for younger lithosphere. For lithosphere older than approximately 70 million years surface heat flow decreases slowly than the half space model predicts. Therefore, other models were proposed and so-called GDH1 (Stein and Stein, 1992) is used nowadays as the best fitting one.

shape-preferred orientation (Fouch and Rondenay, 2006).

[13]Preferred crystallographic orientation adopted by the constituent minerals in response to the applied deformation.

The thermal state of the oceanic lithosphere reaching the trench is important because it controls the depths of the deepest seismicity occurring in a particular subduction zone (Stein and Stein, 1996). The average values of surface heat flow are 128 $\mathrm{mWm^{-2}}$ for 5 million years, 80 $\mathrm{mWm^{-2}}$ for 20 million years, 66 $\mathrm{mWm^{-2}}$ for 60 million years, and 53 $\mathrm{mWm^{-2}}$ for 100 million years old lithosphere. The measurements in forearc clearly showed that surface heat flow is low, typically 30 – 40 $\mathrm{mWm^{-2}}$ (Ziagos et al., 1985; Springer and Förster, 1998; Hyndman et al., 1995), however, in some rare cases it could be as low as 15 $\mathrm{mWm^{-2}}$ (Grevemeyer et al., 2005).[14] Unlike forearcs, backarc regions are usually much hotter and values about 70 – 80 $\mathrm{mWm^{-2}}$ are reported (e.g. Hyndman and Lewis, 1999). The extent of anomalously high surface heat flow zone in backarcs may vary but usually is hundreds of kilometres (see Table 2.1) and, moreover, elevated surface heat flow occurs also in backarcs where no recent extension is reported as shown in Figure 2.3 (Hyndman et al., 2005; Currie and Hyndman, 2006). Between the forearc and the backarc very high heat flow values are observed since a volcanic front sits there. The transition between the cold forearc and the hot backarc is sharp: a considerable increase in surface heat flow is observed in a narrow zone maximally 50 km in width (Bostock et al., 2002); Lewis et al. (1988) observed even a sharp transition in 20 km width zone in the Juan de Fuca subduction plate.

In some backarcs, spreading at rates about $5 - 10$ cm/year is observed[15] (Taylor and Martinez, 2003) so high heat flow values are not surprising there. However, there is a number of backarcs, where extension is not reported (or just a few mm/year at maximum (Hyndman et al., 2005)) and a noticeable increase in surface heat flow is there observed as well. An excellent example of this remarkable feature is the Cascadia subduction zone (see Figure 2.4). The high surface heat flow zone extends there up to 550 km. The anomalously high surface heat flow above this subduction zone is there even more evident because the backarc is adjacent to a cold cratonic lithosphere, where the average measured surface heat flow is as low as 42 $\mathrm{mWm^{-2}}$ (Rudnick et al., 1998). Moreover, a slight increase in the heat flow with a decreasing distance from the cold craton has been reported, but it has been attributed to the radiogenic heat production (Hyndman and Lewis, 1999).

Although the increase in surface heat flow seems to be an important feature of all backarcs[16], not too much attention has been paid to it in subduction zone modelling (although spreading in backarc basins has been numerically modelled (Kincaid and Hall, 2003)) and if so, then models were not successful in reproducing such a pattern in surface heat flow (Eberle et al., 2002; Currie et al., 2004b).

[14] These extremely low heat flow values for Costa Rica/Nicaragua ($20 - 25$ million years old) crust being subducted is explained by hydrothermal circulation in the upper oceanic crust.

[15] The best known examples are the Lau Basin in the Tonga-Kermadec subduction zone and the West Mariana Ridge.

[16] Despite being emphasized as a common feature quite recently by Hyndman et al. (2005), the fact has actually been known for more than 30 years (Blackwell, 2005).

backarc name	backarc width [km]	number of samples	surface heat flow [mWm^{-2}]
Northern Cordillera	650	23	76±21
Cascadia	500	73	75±15
Mexico	>200	6	72±17
Central Andes	400	17	85±16
Aleutian (Bering Sea)	>900	31	75±18
Kamchatka (Okhotsk)	>800	82	70±18
Korea	>750	78	69±16
Sunda (Borneo)	>900	76	76±18

Table 2.1: Constraints on the thermal structure of backarcs with no thermally-significant extension. Compiled from various sources by The Geological Society of America (repository data item 2005030).

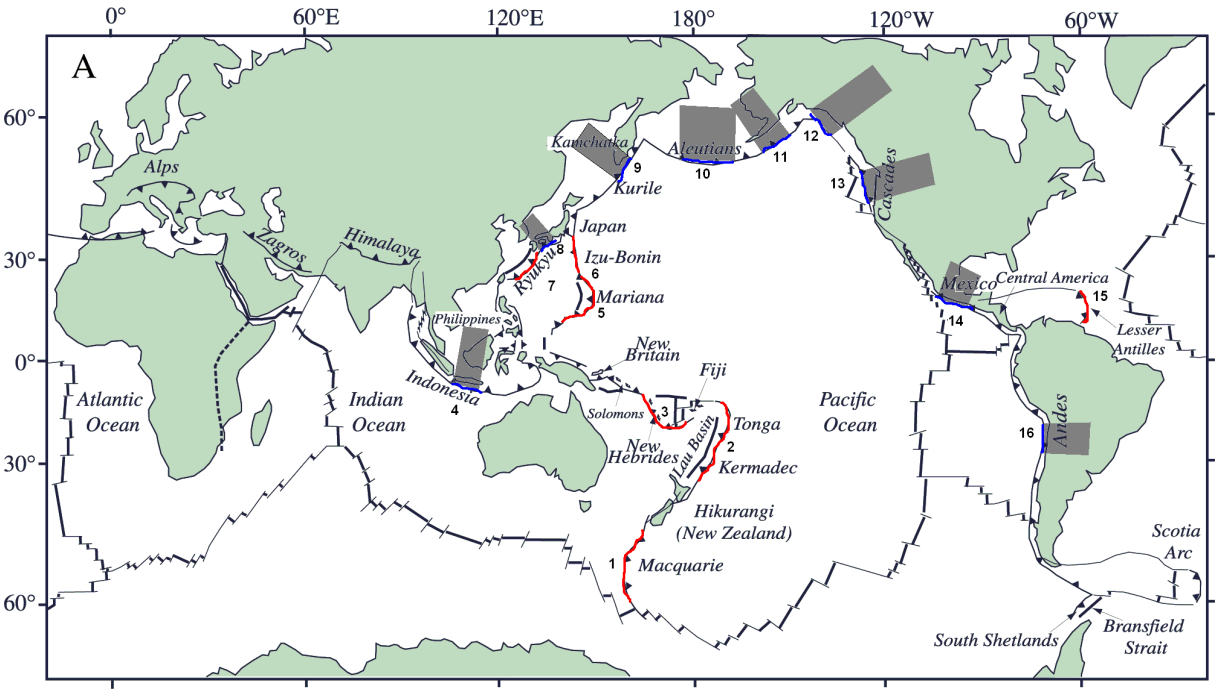

Figure 2.3: Examples of subduction zones (blue) with nonextensional backarcs with elevated high heat flow (gray areas) and subduction zones (red) in whose backarcs spreading is observed. Data compiled from Hyndman et al. (2005) and Leat and Larter (2003). 1. MacQuarie, 2. Tonga-Kermadec, 3. Vanuatu (New Hebrides), 4. Borneo, 5. Mariana, 6. Izu-Bonin, 7. Ryukyu, 8. Korea, 9. Okhotsk sea, 10. Bering Sea, 11. Alaska, 12. Northern Cordilliera, 13.Cascadia, 14. Mexico, 15. Lesser Antilles, 16. Central Andes.

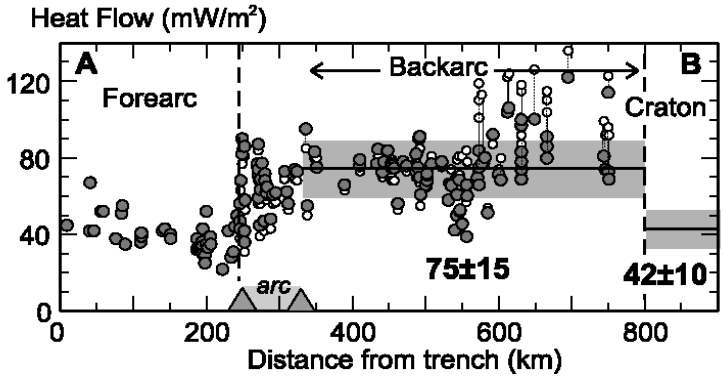

Figure 2.4: Measured heat flow data in the backarc of the Cascadia subduction zone (according to Currie and Hyndman (2006)).

2.2.4 Serpentinization of Forearcs

Subducting sediments and oceanic crust contain presumably a considerable amount of water either capped in cracks and pores or chemically bound in hydrous minerals. Water carried with subduction is expected to be released from the descending slab and cause hydration of the overlying forearc mantle wedge (Peacock, 1993). At shallow depths, water is released by compaction of the sediments[17], while at greater depths a number of dehydration reactions occur and the continuous dehydration along the subducting slab is both expected (Schmidt and Poli, 1998; Rüpke at al, 2004) and numerically modelled (Iwamori, 1998, 2007). The importance of water content in subducted rocks has been discussed for a long time, since water lowers the melting temperatures of rocks and may cause melting in a relatively cool mantle wedge (Gill, 1981). However, the continuous input of water into the mantle wedge is important also from another point: an addition of water into dry mantle wedge minerals (olivine and orthopyroxene) results in a number of hydrous minerals, primarily serpentinites (antigorite, chrysotile, and fine grained lizardite) and talc. Serpentinites are know to have a low density and, what seems to be even more important, significantly reduced strength, which could have a great impact on mantle wedge flow (Gerya et al., 2002).

Serpentinization of mantle wedge forearcs has been reported from many subduction zones, including Mariana (D'Antonio and Kirsten, 2004), Cascadia (Bostock et al., 2002; Brocher et al., 2003), and central Japan (Kamiya and Kobayashi, 2000), and it is generally accepted that extensive serpentinization is a common feature of most, if not all, forearcs (Hyndman and Peacock, 2003). Geophysical evidence is primarily based on anomalously low seismic velocities, which were assumed by Raleigh (1967). As discussed in the previous section, surface heat flow in forearcs is low, which suggests temperatures about 400 °C at depths of about 40 km, and under such conditions P wave velocity in a dry mantle

[17]Analysis of results of P and S wave tomography shows that liquid exists in cracks to a depth of about 60 km (Nakajima et al., 2005).

is greater than 8.2 km/s. Seismic tomography, however, revealed P wave velocities as low as 6.9 km/s in some of these regions (Kamiya and Kobayashi, 2000). Since the linear relationship between P wave velocity of partially serpentinized peridotites and the degree of serpentinization (i.e. water content) has been observed by experiments (Carlson and Miller, 2003), the degree of serpentinization of mantle wedges may be estimated; according to Hyndman and Peacock (2003), serpentinization is about 50 – 60 % in highly serpentinized forearcs (e.g. Central Andes, Cascadia, Izu-Bonin) and about 20% in less serpentinized forearc (Alaska). Forearcs exhibit also other signs supporting the idea of serpentinization such as increased Poisson's ratio[18], high conductivity (Wannamaker et al., 1989) and the presence of serpentinites is proved also by results from drilling projects (D'Antonio and Kirsten, 2004) or geochemical evidence (Guillot et al., 2000).

Serpentinization greatly impacts the rheology: it was demonstrated that 10% serpentinized dunite (peridotite) has strength equal to that of the pure serpentinite (Escartin et al., 2001). Moreover, the most stable serpentinite mineral, antigorite, is stable to temperatures about 700 °C even at high pressures[19], so the whole forearc mantle wedge is likely to be very weak and it could have a significant influence of the mantle wedge flow.

2.2.5 Exhumation

During the subduction, the oceanic crust sinks into the depths where high pressure causes metamorphic changes in the subducted material. These high pressure metamorphosed rocks, such as eclogite, are, however, found at the Earth's surface: for instance, Tsujimori et al. (2006b) provided a review of worldwide occurrences of lawsonite eclogites (high-pressure low-temperature metamorphic rocks). Particularly, the exhumation of eclogite, which is denser (3.5 g/cm^3) than the surrounding peridotite (3.3 g/cm^3), is still a fundamental problem in tectonics.[20] The importance of substantially denser eclogite was recognized yet by Holmes (1931) who hypothesized that the oceanic crust sinking into the mantle[21] should produce eclogite, which then provides the sufficient mechanism for the

[18]The Poisson's ratio is related to the ratio between P and S seismic velocities: $\sigma = \frac{1}{2}\frac{(V_P/V_S)^2-2}{(V_P/V_S)^2-1}$. Laboratory experiments give values $\sigma = 0.26$ ($V_P/V_S = 1.76$) for dry peridotites, $\sigma = 0.3$ ($V_P/V_S = 1.87$) for 15% serpentinized peridotites, and $\sigma = 0.38$ ($V_P/V_S = 2.27$) for pure serpentinite (Hyndman and Peacock, 2003). For instance, Kamiya and Kobayashi (2000) reported that the low velocity zone in the subduction zone in central Japan may be divided into two parts: the mantle wedge near the upper boundary of the subducting slab with the Poisson's ratio higher than 0.3 (in depths between $20 - 75$ km) and the rest of descending plate with the Poisson's ratio about 0.25, which gives clear indication of wedge serpentinization.

[19]Ulmer and Trommsdorf (1995) reported antigorite breakdown at pressures about 7.5 GPa, while other studies observed it at a lower pressure of about 4.5 – 5.5 GPa (Wunder and Schreyer, 1997).

[20]Eclogites were the source of controversy for almost one century. Even if the fact that eclogite is a high-pressure equivalent of gabbro was guessed from the beginning of the twentieth century, the Moho discontinuity was misinterpreted as a sharp transition between gabbro and eclogite, and a hypothetical eclogite layer in the crust was sought as late as 1970. See Godard (2001) for a historical review.

[21]Although the overall idea of motion presented by Holmes was not correct from the current point of view, as he, not knowing about the role of ocean rifts, assumed ascending currents beneath continents (because he assumed a high temperature at the continent roots caused by the radiogenic heat), he was

continental drift. Nowadays, there is a good agreement that the crustal rocks are buried into the mantle by subduction, but the processes of the metamorphosed rocks uplift have not been yet understood well.

The exhumation is fast, i.e. the exhumation rates are comparable to plate motion rates. The youngest[22] eclogite found at the Earth' surface, exhumed from a depth of about 75 km, is about 4 millions years old, which suggests the exhumation rates of order cm per year (Baldwin et al., 2004). On the other hand, it seems that the exhumation rate does not correlate with the convergence rate: while the subduction rate of the Adriatic plate beneath Europe was about 2 cm/year and the exhumation rate observed in Western Alps was 1.3 cm/year, in the Himalaya, the convergence rate was estimated to 10 – 18 cm/year and the exhumation rate was just around 0.5 cm/year (Guillot et al., 2001). A commonly observed feature of eclogite at the surface is the simultaneous presence of serpentinite, which was reported from many places, e.g. Alps (Hermann et al., 2000), Himalaya (Guillot et al., 2000) and a classical example of high-pressure low-temperature eclogite in serpentinite-matrix is from California (Tsujimori et al., 2006a). It is supposed that serpentinite plays a critical role in eclogite exhumation due to lowering the bulk density: antigorite serpentinites have a density about 2.75 g/cm^3 and are therefore extremely buoyant with respect to the surrounding peridotites and eclogites. The exhumed rocks are usually a mixture of serpentinites and eclogites (for example in Alps, the exhumed rocks containing approximately 65% of variably serpentinized peridotites (of density 3.2 g/cm^3), 30% serpentinites (2.8 g/cm^3) and 5% eclogites (3.5 g/cm^3) with the density of about 3.1 g/cm^3 have been reported (Hermann et al., 2000)) and thus its total density is lower that the density of the peridotite. Another essential point is that the eclogite exhumation takes place within the serpentinite stability field (Ulmer and Trommsdorf, 1995) and therefore it is suggested that serpentinites may act as carriers of the eclogite blocks (Hermann et al., 2000). Since serpentinites exhibit also a significantly lower viscosity[23] than dry rocks, it was suggested that they might act as lubricants in the exhumation processes (Guillot et al., 2000, 2001).

Various mechanisms of high-pressure and ultrahigh-pressure metamorphic rocks exhumation, including a corner flow in the tip of the forearc wedge, have been suggested. In his review, Platt (1993) came to the conclusion that the only effective force for the exhumation of rocks from the depths of about 100 km to the base of the crust is buoyancy. The corner flow was modelled in its simplest form as 1-D problem (Schwartz et al., 2001; Gerya and Stöckert, 2002; Raimbourg et al., 2007): the narrow channel of serpentinite of a constant width L along the plate-wedge interface is assumed (see Figure 2.5). At the plate-wedge interface the velocity is given by the subduction rate v_0 and at the hanging wall no-slip boundary condition is used.

pretty close to our understanding in what is the source of the motion. It might be surprising that *zones of subsidence* (subduction zones) foreseen by Holmes even before the discovery of Wadati-Benioff zones were ignored by the supporters of the continental drift theory.

[22]Timing of the exhumation is derived from the partition of parent-daughter radiotopic isotopes.

[23]Le Pichon et al. (1997) expected values about 10^{20} Pas for serpentinites in contrast to 10^{23} Pas for dry peridotites. Schwartz et al. (2001) assumed values ranging from 10^{19} Pas for completely serpentinized peridotite to 10^{21} Pas for 12% serpentinized mantle (both at 550°C).

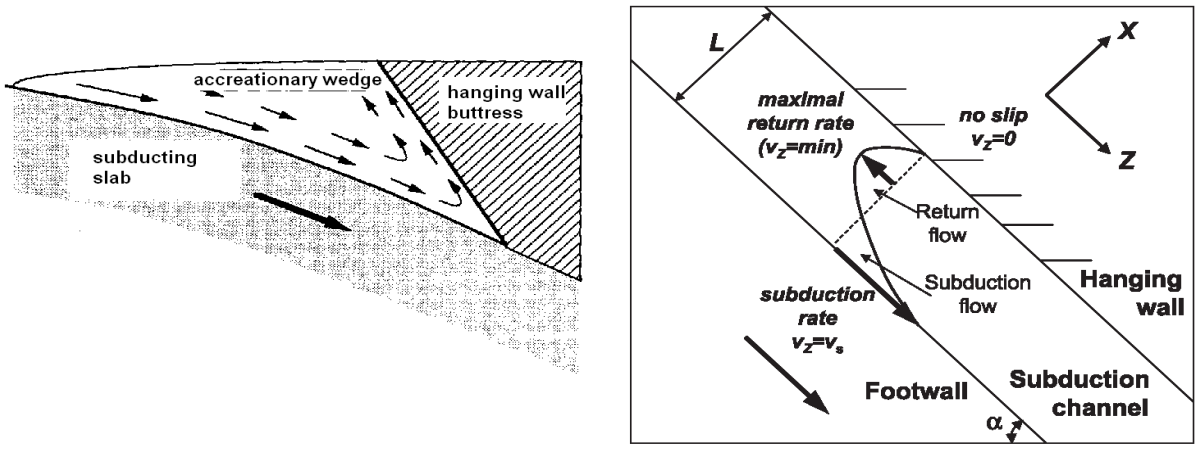

Figure 2.5: Left: the corner flow was first proposed in sediments only, i.e. just in the accreationary wedge (Cloos, 1982). In order to explain the exhumation from depths of about $80 - 100$ km, both Guillot et al. (2000) and Schwartz et al. (2001) proposed the serpentinite channel, which should extend to such depths. Right: simplified 1-D model of serpentinite wedge – the wedge forms a channel of a constant width along the plate-wedge boundary.

In the case of constant viscosity, the velocity profile across the channel is then given by the equation

$$v = \frac{1}{2\eta}\frac{\mathrm{d}P}{\mathrm{d}z}\left(x^2 - Lx\right) - \frac{v_0 x}{L} + v_0, \qquad \frac{\mathrm{d}P}{\mathrm{d}z} = \Delta\rho g \sin\delta, \tag{2.5}$$

where δ denotes the dip of the subducting plate and L is the width of the exhumation channel (see Figure 2.5). The velocity in equation (2.5) may be expressed in an analytical form for various of non-linear[24] viscosities η. However, the important fact is that if the density contrast is sufficient and the viscosity is low, an upward flow occurs at least at some portion of the channel. To model an upward flow of $0.1 - 1.0$ cm/year, viscosities around 10^{20} Pas, density contrast of about 0.5 g/cm^3, and a channel with of order 10 km are required, which is roughly in agreement with what might be realistic values (Schwartz et al., 2001).

Although the model predicts the exhumation rates of the same order as those observed, it seems to be oversimplified even in the case of complex rheology employed (Gerya and Stöckert, 2002). Particularly, the no-slip condition on hanging wall boundary and the simplified geometry are a big source of uncertainty.[25] In fact, it assumes the mantle wedge

[24]Particularly power-low rheology used by Gerya and Stöckert (2002).

[25]1-D model obviously must incorporate some simplifications, but the proposed subduction channel model looks a bit suspicious. For instance, there is a hidden assumption on temperature – the model extents to the depth, where temperature, under which serpentinites are stable, is not overreached. This depth, around $60 - 80$ km (Hyndman and Peacock, 2003), is, in fact, an outcome from other subduction-wedge models (e.g. Peacock, 1993), but those do not include a backward flow in the corner in the calculation of the temperature field and it is likely that such a backward flow would affect the temperature field in the wedge. Thus, the 1-D model of exhumation is oversimplified and questionable. The consequences of

to be serpentinized only in the narrow zone along the plate-wedge interface. However, there is a lot of evidence of more extensive serpentinization (Hyndman and Peacock, 2003). That is why numerical models should include the whole mantle wedge rather than just its narrow part which is hypothesized to form an exhumation channel (Giunchi and Ricard, 1999; Gerya et al., 2000; Stöckert and Gerya, 2002; Gerya et al., 2002).

Important information about the exhumation may be inferred from P-T paths of the buried rocks. The record preserved in the rocks is valuable, since different mechanisms of exhumation would result in different retrograde P-T paths. Two main types are distinguished: Alpine-type exhumation is characterized by nearly isothermal decompression and Franciscan-type is characterized by decompression and simultaneous cooling. Alpine-type exhumation usually involves continental crust, while Franciscan type prevails in intra-oceanic subductions (Ernst, 1988). Recently, the Alpine-type exhumation has been found for instance in eclogite samples from southern Mexico (decompression from 1.6 GPa to 0.6 GPa at temperatures about 600°C) (Meza-Figueroa et al., 2003) or in exhumed eclogites in Usagaran belt in Tanzania[26] (decompression from 1.7 GPa to lover crustal levels 0.7 GPa at the temperature 750°C before cooling and further uplift) (Herms, 2004).

2.2.6 Constraints from Key Observations

Key observations about the temperatures in the subduction zone and the overlying wedge come from measurements of surface heat flow since direct temperature measurements are impossible (except for the uppermost part of the crust). Every subduction model should therefore predict low surface heat flow in forearcs regions, where values about 30 – 40 $\mathrm{mWm^{-2}}$ have been reported from a number subduction zones (e.g. Hyndman and Wang, 1995), and relatively high surface heat flow in backarc regions, where uniformly high values about 70 – 80 $\mathrm{mWm^{-2}}$ have been measured in almost all subduction zones (Currie and Hyndman, 2006).

Deductions from the surface heat flow measurements are supported with a variety of other observations. The separation of the mantle wedge overlying the subducting plate into a cold forearc and a hot backarc is noticeable particularly from seismic tomography both in seismic velocities (Zhao et al., 1994) and Q factor (Abers et al., 2006). Low temperatures in forearc are moreover supported with the existence of serpentinite found in the ocean drilling program (D'Antonio and Kirsten, 2004) or in the exhumed material at the Earth's surface (Guillot et al., 2000) as well as in seismic studies of the Poisson's ratio (Kamiya and Kobayashi, 2000).

These additional evidences provide consequently other constraints on numerical models of the forearc: widespread serpentinization (Hyndman and Peacock, 2003) and a low strength of serpentinite (Escartin et al., 2001) indicate that despite being relatively cold, the forearc likely is not stagnant and a substantial flow occurs there which would explain the exhumation of heavy eclogites (Hermann et al., 2000).

---

the exhumation process on the temperature field was demonstrated in 2-D numerical model of Taiwan (Ryukyu subduction zone), where the surface heat flow up to $200\mathrm{mWm^{-2}}$ was observed (Lin, 2000).

[26] Former subduction of an oceanic crust (2 milliard years old).

Unlike the forearc, the backarc is hot. Besides the heat flow data, also xenoliths, the exhumed rocks, provide the additional independent evidence of high temperatures ($\sim$ 1200 °C at 60 km) in the shallow backarc mantle (Currie and Hyndman, 2006). Due to expected high temperatures the backarc is supposed to have a low viscosity as well and a large scale flow occurring there might result in observable geoid anomalies. Since the gravity anomalies exhibit local extreme above major subduction zones, also the influence of the flow associated with subduction on the dynamic topography[27] has been investigated (Billen and Gurnis, 2001; Liu and Bird, 2006; Tosi, 2008). In order to reproduce the observed regional dynamic topography, the low viscosity wedge (LVW) is required and the viscosity contrast between the LVW and the underlying asthenosphere must be at least one order of magnitude (Billen and Gurnis, 2001, 2003).

2.3 Rheology

Rheology of the upper mantle is supposed to be controlled by creep properties of olivine, which is the dominant mineralogical constituent[28] (Ranalli, 1998). Creep properties of olivine aggregates have been studied experimentally and two distinct creep mechanisms were identified at high temperatures: Newtonian and power-law. These creep regimes can be generally described by the steady-state rheological law

$$\dot{e}_{ij} = A\sigma^{n-1} d^{-m} \exp\left(-\frac{H}{RT}\right) \sigma_{ij}, \tag{2.6}$$

where $\dot{e}_{ij}$ is the ij-th component of the strain rate tensor, σ_{ij} is the ij-th component of the deviatoric stress tensor, σ is the second invariant of the deviatoric stress tensor, A is a material constant, d is the grain size, R is the gas constant, and $H = E + pV$ is the activation enthalpy. Since the second invariants of the stress and the strain rate tensors are defined as

$$\sigma = \sqrt{\frac{1}{2}\sigma_{ij}\sigma_{ij}}, \qquad \dot{e} = \sqrt{\frac{1}{2}\dot{e}_{ij}\dot{e}_{ij}}, \tag{2.7}$$

the rheological law is often written as

$$\dot{e} = A\sigma^{n} d^{-m} \exp\left(-\frac{H}{RT}\right). \tag{2.8}$$

Equations (2.6) or (2.8) describe both dislocation power-law rheology with a stress exponent[29] $n > 1$, which is independent on the grain size, and diffusion creep, which is Newtonian (i.e. strain is proportional to stress, $n = 1$) but is inversely proportional to

[27] Dynamic deformation of the Earth's surface.

[28] About 50% by volume.

[29] As the stress exponent increases, the behaviour or deformed rocks approaches that of a perfectly plastic material, i.e. no deformation until the stress reaches the yield stress magnitude and than deformation at constant stress. The stress exponent in mantle materials is usually $n \geq 3$.

the grain size[30]. Measured parameters indicate that diffusion creep is the dominating deformation mechanism under conditions of small grain size, low stress, and high pressure (Kohlstedt et al., 1995). However, there might be large uncertainties in the conclusions on rheology made from experiments since they are carried out at relatively low pressures (mostly under pressure ≤ 300 MPa (e.g. Zimmerman and Kohlstedt, 2004)) and the usual strain rate is $10^{-4} - 10^{-6}$ s^{-1} (Karato and Wu, 1993) in contrast to values $10^{-14} - 10^{-16}$ s^{-1} assumed in the mantle. But perhaps the largest uncertainty comes from poorly constrained activation volume V, which is known only for some olivine aggregates (Ranalli, 1998) and often is neglected as all the measurements are conducted under the same pressure (Zimmerman and Kohlstedt, 2004). If it is measured, the results may be affected by large errors (Karato and Ogawa, 1982).

The dislocation creep is associated with LPO and thus anisotropy of seismic velocities may give a clue which parts of the mantle deform by dislocation creep. Seismic anisotropy is primarily observed in the upper 300 km (Karato and Wu, 1993) and it seems to be likely that in the upper mantle, both creep regimes occur if the grain size is between 0.1 and 10 mm. Unlike the upper mantle, the lower mantle[31] likely deforms by Newtonian diffusion creep (Ranalli, 1998).

An important independent source of viscosity information is postglacial rebound because it does not require any information about the grain size, temperature, and other physical properties like water content, which also affect the rheology. It is based on observation of relative sea level which changes from the last Ice Age due to glacial unloading. The method is broadly employed for radial viscosity determination and it gives an important constraint on the overall viscosity. Kaufmann and Lambeck (2002) presented average values 7×10^{20} Pas for the upper mantle and 2×10^{22} Pas for the lower mantle with no sharp increase across the 670-km seismic discontinuity. Postglacial rebound studies also shown that a layer of non-linear creep at the surface is relatively thin (≤ 200 km) comparing with the thickness of the whole mantle (Karato and Wu, 1993).

Even in the case when the relationship between the stress and the strain is non-linear, the term viscosity is used to describe the material properties. In this case, so-called effective viscosity defined is as $\eta = \sigma/2\dot{e}$ and equation (2.8) may be rewritten in the term of the effective viscosity as

$$\eta = A^{\frac{1}{n}} e^{\frac{1-n}{n}} d^{\frac{m}{n}} \exp\left(\frac{E + pV}{nRT}\right). \tag{2.9}$$

If more than one flow laws apply simultaneously, the total effective viscosity is given by

$$\eta_{\text{eff}} = \frac{1}{\sum \frac{1}{\eta_i}}. \tag{2.10}$$

The rheological properties of rocks are strongly influenced by water content (Hirth and Kohlstedt, 1996, 2003). With respect to the equation (2.10) the flow law for hydrated rocks

[30] $m = 2$ is so-called Nabarro-Herring creep and $m = 3$ so-called Coble creep.
[31] Composed mainly from perovskite, which forms about 70% (Ranalli, 1998).

may be rewritten as

$$\dot{e} = \left(A_d \exp\left(-\frac{H_d}{RT}\right) + A_w C_{OH}^r(T,P) \exp\left(-\frac{H_w}{RT}\right)\right) \sigma^n, \tag{2.11}$$

where C_{OH} is the concentration of hydroxyl ions and subscripts d and w means dry respectively wet conditions (Karato, 2003). Both water content and temperatures cause viscosity reduction and it would be of interest to separate these two effects in order to determine water content in the asthenosphere. The quality factor Q also depends both on temperature and water content and equation (2.1) may be rewritten (Karato, 2003) as

$$\frac{1}{Q} \sim \omega^\alpha \exp\left(\frac{-\alpha H}{RT_{\text{eff}}}\right), \tag{2.12}$$

where T_{eff} is the rheologically effective temperature incorporating the effect of water defined by

$$T_{\text{eff}} = \xi T, \qquad \xi = \frac{1}{1 - \frac{RT}{H^*} \log \frac{A_w C_{OH}^r}{A_d}}. \tag{2.13}$$

In this equation a single value of activation enthalpy H^* is used because differences between H_d and H_w are small. Using the rheologically effective temperature the flow law can be also expressed as

$$\dot{e} \sim \sigma^n \exp\left(\frac{H^*}{RT_{\text{eff}}}\right) \tag{2.14}$$

and hence the relation between Q factor and viscosity (2.3)[32] and the disperse equation (2.4) may be used to express differences in Q factor and seismic velocities observed by seismic tomography in the term of the rheologically effective temperature. For backarc areas the rheologically effective temperature is by about 400°C higher than the temperature in a radially-symmetric Earth model. Karato (2003) concluded that likely only a part of this temperature difference is caused by actual increase in temperature and the rest is caused by high water content.

The diffusion and dislocation creep mechanisms, however, dominate only at high temperatures ($T/T_m \sim 0.5$, where T_m is the melting temperature). At low temperatures ($T/T_m \leq 0.3$), the Peierls creep is observed. The Peierls flow law is expressed by the equation

$$\dot{e} = A \exp\left(-\frac{H}{RT}\left(1 - \frac{\sigma}{\sigma_p}\right)^q\right), \tag{2.15}$$

where A and q are constants and σ_p is the Peierls stress (Kameyama et al., 1999). The Peierls creep is important as it is a stress-limiting deformation mechanism at low temperatures. In numerical models, it is sometimes (van Hunen et al., 2000; Kneller et al., 2005; Čížková et al., 2007) approximated with a strain-rate dependent yield viscosity defined as

$$\eta_y = \sigma_y \dot{e}_y^{-\frac{1}{n_y}} \dot{e}^{\frac{1}{n_y}-1}, \tag{2.16}$$

[32] In the case of power-law rheology a modified relation $\frac{\eta}{\eta_0} = \left(\frac{Q}{Q_0}\right)^{\frac{1}{n\alpha}}$ is to be used.

where σ_y is the yield stress, $\dot{e_y}$ is the yield strain, and n_y is the exponent defining the brittleness of the material.[33]

2.4 Mathematical Models

Numerical modelling of mantle convection is based on our understanding that the driving force is buoyancy. Thus the mantle convection is usually numerically modelled as the Rayleigh-Benard convection[34] and to better reflect material properties of the Earth's mantle, the effects of the non-linear rheology, compressibility and chemical composition are often included (e.g. van Keken, 1993; Matyska and Yuen, 2007). However, there is an important difference between the observed convection in the Earth's mantle and the classical Rayleigh-Benard convection: downwelling associated with the cooling at the colder boundary is always symmetric in the Rayleigh-Benard convection, i.e. the downwelling currents are formed by the thermal boundary layers on both sides. In other words, in the Rayleigh-Benard thermal convection the downwelling descending currents sink into the interior almost vertically and are fed by the cold material from the both sides. This is not true in the Earth, where downwelling limbs, subduction zones, are formed by only one thermal boundary layer (subducting lithosphere), while the other cold boundary layer (overriding lithosphere) remains at the surface. As pointed King (2001), this is a fundamental difference and therefore, a self-consistent formation of subduction zones has been investigated (Bercovici, 2003) and particularly viscosity weakening mechanism have been employed to produce realistic plate tectonics (Tackley, 2000a) since it seems to be more appropriate than applying boundary condition of surface velocity[35] of the overriding lithosphere (Trubitsyn et al., 1999).

Since self consistent generation of plate tectonics with asymmetric downwellings has not been successful yet, different numerical models try to bypass this issue in various ways. Dynamic models usually prescribe a fault at the plates contact up to a certain depth (van Hunen et al., 2000; Čížková et al., 2007) and kinematic models prescribe the velocity of the whole slab (van Keken et al., 2002; Kneller et al., 2005). The models are often focused on the calculation of the temperature distribution in the subducting slab and the adjacent mantle wedge and in this case either kinematic models are used[36] or even simple analytical or semi-analytical solution may be found under some simplifications. The kinematic models usually include a complex, if not realistic, rheology (e.g. Kneller et al., 2007) and allow handling various non-linear effects like shear heating or phase transitions. Since a number of parameters usually influence the calculated results, it may be hard to gain a sufficient

[33]For $n_y = 1$ the maximum viscosity is $\sigma_y/\dot{e}_y$; when $n_y \to \infty$, strain-independent brittle failure is described. In numerical simulations the value $n_y = 5$ is often used.

[34]Convection of isoviscous incompressible fluid bounded by isothermal zero stress boundaries at the top and the bottom. In the case of the Earth, these boundaries are the Earth's surface and the mantle-core boundary.

[35]In fully dynamic models also the surface plate velocity is a result of the simulation.

[36]The attraction of kinematic models consists in the fact that the input of the model is well known – plate velocity, age, and geometry of the subducting plate.

insight and determine which of the studied parameters play a decisive role. In other words, it may be hard to understand the underpinning physics. Unlike that, the mentioned second approach, analytical solution, keeps everything as simple as possible, which may be useful to distinguish between more and less important parameters and that is the reason why it is – perhaps surprisingly – still in use (e.g. England et al., 2004), together with complex fully 3-D models (e.g. Tackley, 2000b; Honda and Saito, 2003; Liu and Bird, 2006; Yoshioka and Murakami, 2007), although the number of 3-D models will likely rapidly increase with the increasing computational power.

A brief review with the focus to the models dealing with a slab-wedge interface is given in next sections.

2.4.1 Analytical Models

The first mathematical model of the temperature distribution in subduction zones considered subduction of the lithosphere into an isothermal mantle (McKenzie, 1969). The model showed how the subducting slab is heated from the adjacent mantle: Considering a semi-infinite slab of width L subducting with a rate V and solving the steady-state heat transfer equation (see Figure 2.6)

$$\rho c_p V \frac{\partial T}{\partial x} = k \left(\frac{\partial^2 T}{\partial x^2} + \frac{\partial^2 T}{\partial y^2} \right), \tag{2.17}$$

where ρ is the density and c_p the heat capacity, leads to a temperature field given by a series

$$T(x,y) = T_m \left(1 + 2 \sum_{n=1}^{\infty} c_n \exp\left(\frac{-\beta_n x}{L} \right) \sin\left(\frac{n\pi y}{L} \right) \right), \tag{2.18}$$

where

$$c_n = \frac{(-1)^n}{n\pi}, \qquad \beta_n = \sqrt{R^2 + n^2\pi^2} - R, \qquad R = \frac{VL\rho c_p}{2k}. \tag{2.19}$$

An important outcome from this model is that the depth, to which an isotherm is advected, is proportional to

$$z_{\max} \sim VL^2 \sin\delta, \tag{2.20}$$

where δ denotes the dip of the subducting plate.[37] The thickness of the slab cannot be measured directly, however, the thermally defined depth of the oceanic floor is proportional to the square root of its age (Stein and Stein, 1992) for a cooling half-space model and consequently one may obtain the relation

$$z_{\max} \sim Vt \sin\delta \tag{2.21}$$

[37] The expression for a maximum distance reached by temperature T_0 is

$$x_0 = -\frac{VL^2\rho c_p}{\pi^2 k} \ln\left(\pi \frac{T_m - T_0}{2T_m} \right).$$

This distance must be multiplied by $\sin\delta$ to be converted to the depth. Consequently, the velocity must be multiplied by $\sin\delta$ in the definition of the thermal parameter as well.

between the maximum depth $z_{\max}$ and the age t of the subducting lithosphere at the trench.

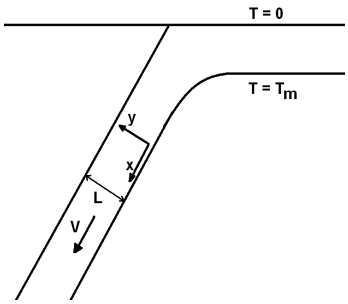

Figure 2.6: Scheme of a simple model of a slab descending into isothermal mantle adopted from Le Pichon et al. (1973). The thickness of the descending slab with velocity V is denoted L and the orientation of the coordinate system is shown.

The term $\Psi = Vt \sin \delta$ is known as a thermal parameter (Schubert et al., 2001) and is simply a product of the age of the subducting plate at the trench and the vertical part of the convergence rate. It is supposed to strongly control the behaviour of subducting plates, particularly their seismicity. The idea is quite simple: the lithosphere is too weak to support seismic failure above some critical temperature and the depth, to which this critical isotherm[38] penetrates the mantle, depends on the thermal parameter. The age of the oceanic lithosphere at the trench, where it starts to subduct, may be determined from magnetic isochrones (Mueller et al., 1997) so this hypothesis may be easily tested. Actually, attempts to correlate the maximum depth of seismicity and the thermal parameter have been started by Molnar et al. (1979), who roughly confirmed the proportional relationship between the length of the seismic zone and the thermal age. Later it was revealed that the proposed linear relationship is valid only when the thermal parameter is less than 2000 km, i.e. in subduction zones where the deepest seismicity is limited roughly by about 260 km (Gorbatov and Kostoglodov, 1997). The relation between the depth of the deepest seismicity and the thermal parameter has been sought as an empirical function $D_m = f(\Psi)$ and the shape of this function (which is roughly linear for $\Psi \leq 2000$ km, flat for $\Psi \in \langle 2000\,\mathrm{km}, 5000\,\mathrm{km} \rangle$, and again linear for $\Psi \geq 5000$ km; see Figure 2.7.) lead to the idea of metastable olivine wedge around the depths of 400 km (Kirby et al., 1996).

Probably because of its simplicity the thermal parameter still attracts an attention. Quite recently Frohlich (2006) derived a simple formula for the temperature T at the

[38] Molnar et al. (1979) suggested that cut-off temperatures increase from about $600 \pm 100\,^{\circ}\mathrm{C}$ at 200 km to $830 \pm 50\,^{\circ}\mathrm{C}$ at 650 km.

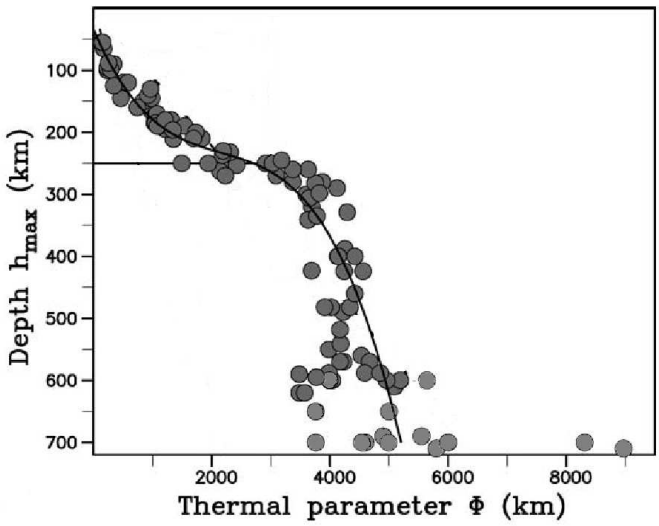

Figure 2.7: The plot of observed deepest seismicity against the thermal parameter Ψ may be expressed as a best fitting polynomial $h_{\max} = 54 + 10^{-1}\Psi + 0.44\,10^{-2}\Psi^2 - 0.37\,10^{-3}\Psi^3 + 0.63\,10^{-5}\Psi^4$. Circles indicate data from individual subduction zones (adopted from Gorbatov and Kostoglodov (1997)). The flattening in the depths of around 300 km presumably corresponds to the exothermic olivine-spinel phase transformation, which releases heat and therefore the temperature of the slab increases there.

depth h in the subduction zone:[39]

$$\frac{T - T_m}{T_0 - T_m} = \mathrm{erf}\left(\sqrt{\frac{h}{2\Psi}\ln\left(1 + \frac{\Psi}{h}\right)}\right) - \mathrm{erf}\left(\sqrt{\frac{h}{2}\left(1 + \frac{h}{\Psi}\right)\ln\left(1 + \frac{\Psi}{h}\right)}\right), \tag{2.22}$$

which gives temperatures reasonably corresponding to some numerical models.

The simple McKenzie's solution, however, does not take into account how the surrounding mantle is cooled by the subducting plate. Even this effect may be treated analytically under the assumption that the overriding mantle flows parallel to the slab surface. Davies (1999) combined this solution with an analytic solution in the case of rigid overriding mantle (which applies at to top) and expressed the temperature analytically along almost the whole slab. This gave a very efficient computational tool for determination of the temperature field near the subduction zones which may be utilized in seismic tomography. A global tomographic model, in which the seismic velocities derived from the temperature

[39]This formula assumes the distribution of the temperature in the oceanic lithosphere to be given by the half-space cooling model, i.e.

$$T(t,z) = T_0 + (T_m - T_0)\mathrm{erf}\left(\frac{z}{2\sqrt{\kappa t}}\right)$$

fields calculated for all major subduction zones using additionally information about their age, has been subsequently constructed (Rhodes and Davies, 2001).

The assumption of flow in the mantle wedge which is parallel to the slab motion seems to be a limitation of the model of Davies (1999). In the mantle wedge, the analytical solution of the corner flow problem (Batchelor, 1967) may be utilized. If the polar coordinates r, θ are defined in such a way that the origin is in the corner of the wedge, the velocity $\boldsymbol{v} = (v_r, v_\theta)$ may be expressed in the terms of the stream function

$$v_r = \frac{1}{r}\frac{\partial \psi}{\partial \theta}, \tag{2.23}$$

$$v_\theta = -\frac{\partial \psi}{\partial r}. \tag{2.24}$$

In the case when the overriding plate has zero velocity and the subducting plate moves with velocity V, the stream function is

$$\psi \sim \frac{rV\left((\delta - \theta)\sin\delta\sin\theta - \delta\theta\sin(\delta - \theta)\right)}{\delta^2 - \sin^2\delta}, \tag{2.25}$$

where θ is measured counter-clockwise from the horizontal base of the overriding plate. This solution assumes Newtonian fluid with a constant viscosity in the wedge. The analytical corner flow solution constitutes a direct link between analytical and numerical solutions since it was used in a model of isoviscous mantle wedge, where a flow field was given by the analytical corner flow solution and a temperature field was calculated numerically (Peacock, 1993; Peacock et al., 1994; Ponko and Peacock, 1995).

2.4.2 Numerical Models

As mentioned before, there are two different types of numerical models. The fully dynamic approach, which has been successful in the explanation of mantle plumes origin, does not produce realistic[40] subduction zones (Tackley, 2000b,c) and therefore additional information (pre-existing faults) allowing to handle the plate-wedge boundary is required in this kind of models. In this work, we are focused to the second approach, kinematic models. It has been shown that under certain conditions, both dynamic and kinematic models give close results if a similar rheology is used (Han and Gurnis, 1999), so it seems quite natural to use kinematic models, particularly, if we are interested in the temperature field in shallow depths (with respect to the thickness of the whole mantle) and if the shape of subducting plate is known. On the other hand, a significant weakness of kinematic models has been named by King (2001): kinematically prescribed slabs behave rigidly since kinematic models are not able to account their internal deformation; the use of kinematic models is limited to shallow portions of the mantle.

[40] Meaning with an oblique dip angles.

Steady-State Mantle Wedge Models

The purpose of kinematic mantle wedge models is to calculate the temperature field at the top of the slab and in the mantle wedge (Peacock, 1996) in order to gain a better understanding of why a chain of volcanoes sits above subducting plates (Gill, 1981). These models started with a semi-numerical model in which only the steady-state heat transfer equation was solved numerically and the flow in the wedge was given by the analytical corner flow solution (Peacock, 1993; Peacock et al., 1994). In the last decade, a number of similar models was published, (e.g. van Keken et al., 2002; Currie et al., 2004b; Kneller et al., 2005; Manea et al., 2005; Peacock et al., 2005). These current wedge models solve both the flow field and the temperature field numerically and, moreover, they are constructed for specific subduction zones rather then for a generic one[41], however the main idea remain the same as in early models of (Peacock, 1993; Peacock et al., 1994). The usual computational domain is shown in Figure 2.8, although in some cases a more complex slab-wedge boundary is assumed[42].

To evaluate the flow the equations of conservation of mass and momentum for an incompressible Boussinesq fluid are solved in the wedge. After the velocity field for the wedge is determined, the steady-state heat transfer equation is solved in the whole domain. These models show that the thermal state of the forearc is strongly controlled by the mantle wedge flow, however, the flow in the wedge is given by the coupling between the prescribed slab and the wedge. If the coupling is strong (i.e. the fault is not taken into account and a prescribed velocity of the slab is used as a boundary condition at the side part of the wedge), an extremely unrealistic ablation occurs in the wedge (Conder, 2005). In contrast to it, if the coupling is weak, a stagnant region in the forearc develops (Abers et al., 2006). That is why even in kinematic models the contact of the subducting plate and the overlying lithosphere must be handled somehow likewise in dynamic models. Several methods may be found in literature: partial coupling between the slab and the wedge[43] (Kneller et al., 2005), inclusion of a non-convecting "cold nose" in the tip the wedge (Abers et al., 2006), or assigning a weak viscosity to the slab top (Conder, 2005).

The calculated temperature field is extremely sensitive to the way how the fault is treated (i.e. to the vigour of the corner flow): it was shown that different fault parameterizations may result in substantial differences of the temperature in the topmost part of the slab about several hundred degrees (Conder, 2005). Since the models are used to answer the question where and how melting occurs in the wedge, it is clear, that correct fault parameterization is of crucial importance. Van Keken et al. (2002) showed that in the case of an old and cold subducting plate, the P-T conditions allow melting only in a thin sedimentary layer at the very top of the subducting slab, while the underlying subducted crust does not melt. Contrary to that, in young subducted lithosphere both the sediments

[41] In the past, models of a generic subduction zone prescribing usually a fixed dip angle value of 26.6° (average value of the shallow dip angle taken between 0 and 100 km depth Jarrad (1986)) were constructed (Peacock, 1993).

[42] Particularly in the case of flat slab subducting beneath Mexico (Manea et al., 2004, 2005).

[43] Only a fraction of the slab velocity in used as a velocity boundary condition of the wedge.

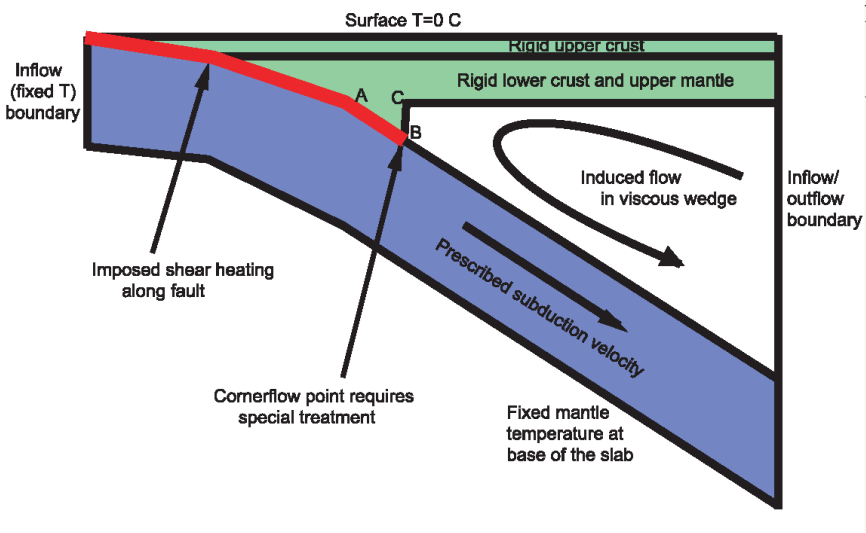

Figure 2.8: Scheme of the geometry of the subduction model. The kinematically prescribed slab induces flow in the mantle wedge below the overriding plate. Taken from van Keken et al. (2002).

and the crust melt.

In the light of uncertainties coming from a fault parameterization, one may ask a question, how robust these predictions are. Fortunately, surface heat flow measured in forearcs may be used to validate the temperature fields, but it turns out that such a constraint is rather weak because the wedge models include also shear heating along the upper boundary of the subducting plate. The rate of shear heating, which is assumed to be produced by the strong deformation along the interface that separates the slab from the overriding plate, is given as a product of downdip velocity and shear stress. General practise is to treat this shear stress as a free parameter in order to fit measured surface heat flow. Thus, the kinematic models offer a sufficient number of parameters for arbitrary model tuning.

Since the kinematic models are dominantly used to infer the temperature state of forearcs, they do not include a large portion of backarcs. The study of Currie et al. (2004b) is the exception directed to hot backarcs, particularly to the Cascadia[44] subduction zone, which tried to explain that globally observed phenomenon (Hyndman et al., 2005). This study came to the conclusion that the traction from subducting slab is not sufficient to induce a wedge flow which would explain high heat flow surface values if the realistic stress- and temperature-dependent rheology is used. Paradoxically, an isoviscous wedge produced a much better fit of surface heat flow data, since a temperature-dependent viscosity tends to focus the flow to a very narrow region close to the subducting slab (see Figure 2.9)

[44]Relatively young and slow lithosphere (about $10-15$ Myr old with a convergence rate 4 cm/y (Heaton and Kanamori, 1984)) subducting under a small dip angle around 30° at shallow depths (Nicholson et al., 2005) and under a dip angle about 60° at greater depths ($\geq$ 100 km) (Jarrad, 1986).

and consequently the rest of the backarc remains cold. That is why the authors concluded that besides the traction from the subducting slab, there must be another reason (perhaps thermal convection) for hot backarcs.

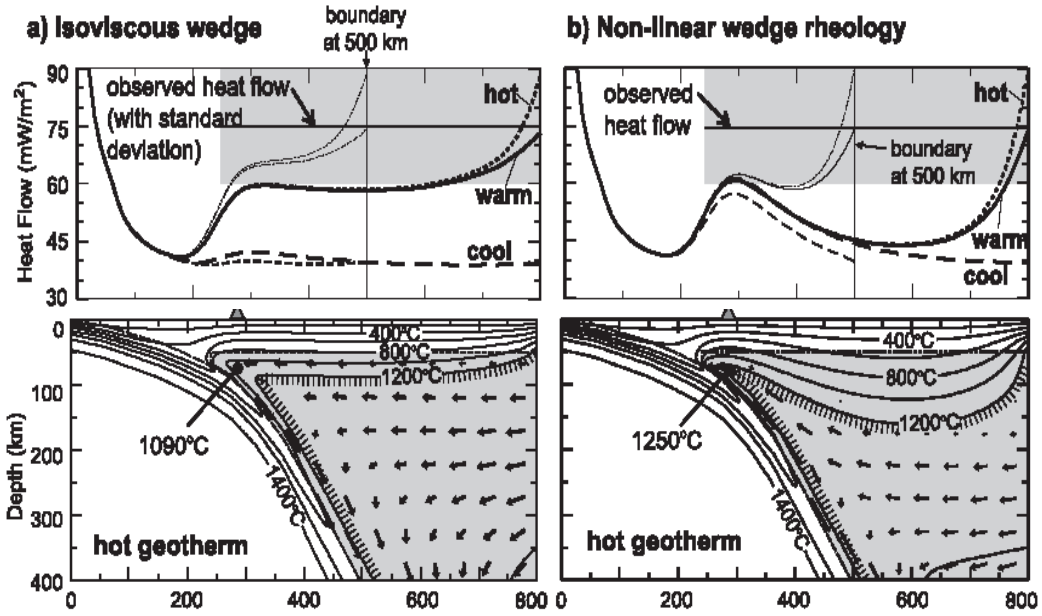

Figure 2.9: The key result of Currie et al. (2004b): the comparison of surface heat flow in the backarc for different continental geotherms (top) in the case of a constant (left) and stress- and temperature-dependent viscosity demonstrates that the zone of elevated surface heat flow is not formed in any case. Temperatures and flow field for the unrealistically hot continental geotherm (surface heat flow 90 $\mathrm{mWm^{-2}}$) is shown (bottom): since the flow is strongly localized to the tip of wedge, the hot backarc is not reproduced. The constant viscosity does not result in such a contraction of the flow and match surface heat flow values better, although not sufficiently.

Other Mantle Wedge Models

Although steady-state wedge models are very popular, unsteady kinematic models are also being investigated. Wang at al. (1995) used a model of Nankai subduction zone to calculate thermal consequences of the Philippine Sea plate (south-western Japan) subduction.[45] The resulting surface heat flow corresponded to the plate which is about 15 million years old and it is consistent with other findings about the age of this young subducting lithosphere. The model, however, prescribed the geometry of the subducting plate in advance during the whole subduction process and set it according to the present day

[45]The most interesting observation regarding the Nankai subduction is an abrupt decrease in surface heat flow, which changes from 130 $\mathrm{mWm^{-2}}$ to 60 $\mathrm{mWm^{-2}}$ along a 60 km distance.

observations so the question, whether or how the dip angle changes during the subduction, was not solved.

Other kinematic models also use the prescribed motion and geometry of the subducting plate (e.g. Stöckert and Gerya, 2002; Honda and Saito, 2003) although they solve the time evolution in the mantle wedge. These models predict that if the viscosity in the wedge is low, circulation likely occurs there. Models of Gerya (Gerya et al., 2002; Stöckert and Gerya, 2002) were directed to explain an exhumation of high-pressure metamorphic rocks and showed that the forced flow in the wedge-shaped region of low viscosity is a feasible mechanism of the exhumation since the obtained P-T paths of the rocks exhumed in the forearc are similar to those recorder in natural samples.[46]

While Geryas' models are focused to the forearc, other models calculate the influence of the LVW on the flow and link it to the observable dynamic topography (Billen and Gurnis, 2001, 2003). The significant difference between these models consists in the viscosity weakening source. In the exhumation models, the low viscosity zone is caused by highly serpentinized rocks and is located in the forearc, but in models predicting the dynamic topography, the LVW is placed in the backarc and the exact source of the viscosity decrease is not investigated although high temperatures and/or high water content are likely.

Dynamic models

In kinematic models, the main driving force is given by the prescribed velocity of the subducting plate, however, the models are limited to the upper part of the mantle (usually do not extend deeper than 400 km). If the calculations are directed to gain some knowledge about subducting plates in greater depths (for instance the interaction of the slab with the 670 km discontinuity (Christensen, 1997; Čížková et al., 2002)), dynamic models are to be used. In these models, the flow is driven by buoyancy and the plates evolve with time. The fundamental problem of this kind of modelling is that the pattern of oblique subducting plates is not reproduced even if the viscosity weakening mechanisms are employed (Tackley, 2000b). That is why a fault prescribed a priory is used (van Hunen et al., 2000, 2004; Čížková et al., 2007) but the slab detachment may be achieved also by imposing a low viscosity layer at the top of the subducting plate (Billen and Hirth, 2005, 2007; De Franco et al., 2007). Since the position of the viscosity weakening is fixed, these models, although fully dynamic, also impose some part of the flow solution to the results in advance.

An important unresolved question related to subduction is what drives the dip angle of subducting plates. Fully dynamic models have a potential to answer this question but the weakening zone decoupling the subducting oceanic plate from the overriding lithosphere should be able to evolve with time as well as the rest of the plate. This is because the viscosity weakening is not an artificial numerical trick enabling plate separation, but the weakening zone represents the oceanic crust, where the high water content is responsible

[46] Calculation explains e.g. the P-T path recorded in eclogites exhumed in western Canadia Cordillera, which were buried to depths corresponding to 1.5 GPa and then exposed to nearly isobaric cooling from 690°C to 540°C.

for the viscosity reduction. Recent dynamic models therefore suggest that the rheological properties of the crust (together with buoyancy) control the subduction dip and the wedge shape (Manea and Gurnis, 2007). In other words, the dip angle is the outcome of interplay among buoyancy, rheological properties, and slab chemistry – dehydration and melting do not occur in the wedge shaped by buoyancy forces but likely are the factors controlling the position of the slab-wedge interface. This would explain why no simple relation between the subduction dip and other properties such as convergence rate or age has been found yet (Cruciani et al., 2005).

Chapter 3

Numerical Modelling

3.1 Basic Equations

The thermal convection is generally described by the law of mass conservation

$$\frac{\partial \rho}{\partial t} + \nabla \cdot (\rho \boldsymbol{v}) = 0, \tag{3.1}$$

the law of momentum conservation

$$\nabla \cdot \boldsymbol{\tau} + \rho \boldsymbol{g} = \rho \left(\frac{\partial \boldsymbol{v}}{\partial t} + \boldsymbol{v} \cdot \nabla \boldsymbol{v} \right), \tag{3.2}$$

and the law of energy conservation, which may be expressed e.g. in p, T variables in the form

$$\rho c_p \left(\frac{\partial T}{\partial t} + \boldsymbol{v} \cdot \nabla T \right) = \nabla \cdot (k \nabla T) + \beta \left(\frac{\partial p}{\partial t} + \boldsymbol{v} \cdot \nabla p \right) + \boldsymbol{D} : \nabla \boldsymbol{v} + Q, \tag{3.3}$$

where the symbol : denotes the total scalar product of tensors and β is the thermal expansion coefficient $\beta = \frac{1}{V} \left(\frac{\partial V}{\partial T} \right)_p$. The law of moment of momentum conservation gives further the condition on symmetry of the stress tensor

$$\boldsymbol{\tau} = \boldsymbol{\tau}^T, \tag{3.4}$$

which is defined in the form

$$\boldsymbol{\tau} = -p\boldsymbol{I} + \boldsymbol{D}(\boldsymbol{v}). \tag{3.5}$$

The non-pressure part of the stress tensor $\boldsymbol{\tau}$, denoted as $\boldsymbol{D}$, includes the rheological behaviour of the fluid (Brdička et al., 1959). In Newtonian fluids, i.e. fluids in which stress versus strain rate curve is linear, the non-pressure part of stress tensor is

$$\boldsymbol{D} = \eta(\dot{\boldsymbol{e}} - \frac{1}{3} \nabla \cdot \boldsymbol{v} \boldsymbol{I}), \tag{3.6}$$

where $\dot{\boldsymbol{e}}$ is the strain rate tensor defined as

$$\dot{\boldsymbol{e}} = \frac{1}{2}\left(\nabla \boldsymbol{v} + (\nabla \boldsymbol{v})^T\right) \tag{3.7}$$

and η denotes the dynamic viscosity. The above set of equations (3.1) – (3.3) must be completed by a state equation

$$F(\rho, p, T) = 0 \tag{3.8}$$

in order to set the system of six equations for six unknowns: three components of velocity $\boldsymbol{v}$, pressure p, density ρ, and temperature T.

Dimensionless analysis shows that the inertial term in equation (3.2) can be omitted in the case of mantle convection: If the characteristic length of the system is denoted as d, then the dimensionless variables denoted by primes are

$$x = dx', \qquad t = \frac{d^2}{\kappa}t', \qquad p = \frac{\eta\kappa}{d^2}p', \qquad \boldsymbol{v} = \frac{\kappa}{d}\boldsymbol{v'} \tag{3.9}$$

and equation (3.2) may be rewritten as

$$-\nabla p' + \nabla \cdot \left(\frac{\eta}{\eta_0}\nabla \boldsymbol{v'} + (\nabla \boldsymbol{v'})^T\right) + \frac{(\rho - \rho_0)d^3}{\kappa\eta}\boldsymbol{g} = \frac{\kappa_0\rho_0}{\eta_0}\left(\frac{\partial \boldsymbol{v'}}{\partial t'} + \boldsymbol{v'} \cdot \nabla \boldsymbol{v'}\right). \tag{3.10}$$

The dimensionless ratio $Pr = \frac{\eta}{\rho\kappa}$ is known as the Prandtl number. The representative values for the convection in the Earth's mantle $\kappa_0 = 10^{-6}$ m^{2}s^{-1}, $\rho_0 = 5. \times 10^3$ kgm^{-3}, and $\eta = 10^{21}$ Pas (Fowler, 2005) yield a very high value of the Prandtl number, about 10^{24}, and therefore $\frac{1}{Pr}$ in equation (3.10) may be treated as zero.

Further simplification of the system of governing equations stems from the observation that "the variations of density can be ignored except were they are multiplied by the acceleration of gravity in equation of motion for the vertical component of the velocity vector" (Boussinesq, 1903), which is applicable to a buoyancy-driven convection. This approach, nowadays generally called Boussinesq approximations (Zeytounian, 2003), allowing to work with quasi-incompressible fluid is widely used in various problems of fluid dynamics. In mantle convection, either *incompressible* or *compressible extended Boussinesq approximation* is used. In both cases, the heat transfer equation reads

$$\rho_0 c_p \left(\frac{\partial T}{\partial t} + \boldsymbol{v} \cdot \nabla T\right) = \nabla \cdot (k\nabla T) - \rho_0 \boldsymbol{v} \cdot \boldsymbol{g_0}\beta T + \boldsymbol{D} : \nabla \boldsymbol{v} + Q, \tag{3.11}$$

whereas the continuity equation is either

$$\nabla \cdot \boldsymbol{v} = 0 \tag{3.12}$$

or

$$\nabla \cdot (\rho_0 \boldsymbol{v}) = 0. \tag{3.13}$$

In these equations, the zero subscripted quantities refer to the reference state given by $\nabla p_0 = \rho_0 \boldsymbol{g_0}$ and the state equation (3.8) is assumed in the linearized form $\rho = \rho_0 (1 - \beta(T - T_0))$,

where β is the thermal expansion coefficient. The *classical Boussinesq approximation* moreover assumes Newtonian fluid with a constant dynamic viscosity η, neglects both dissipation terms $\boldsymbol{D} : \nabla \boldsymbol{v}$ and adiabatic heating $-\rho_0 \beta T \boldsymbol{v} \cdot \boldsymbol{g_0}$, and requires the thermal conductivity k, the isobaric specific heat c_p, and the thermal expansion coefficient β to be constant.

In this work, we assume an incompressible fluid, however, we do not neglect energy dissipation. Since we are interested in the steady-state flow, the time derivatives vanish and we finally have the set of governing equations

$$-\nabla p + \nabla \cdot \boldsymbol{D} + \rho \boldsymbol{g} = 0, \tag{3.14}$$

$$\nabla \cdot \boldsymbol{v} = 0, \tag{3.15}$$

$$\rho c_p \boldsymbol{v} \cdot \nabla T = \nabla \cdot (k \nabla T) + \boldsymbol{D} : \boldsymbol{v} + Q. \tag{3.16}$$

The first two equations (3.14) – (3.15) are known as the Stokes problem. They might be numerically solved directly in $\boldsymbol{v}$ and p variables using the Galerkin method (Křížek and Neittaanmäki, 1990), however, the discretized system of equations is then ill-conditioned since the stiffness matrix contains zeroes on the main diagonal which is a consequence of absent pressure in the continuity equation. Therefore, the penalty method (Cuvelier et al., 1986) is often used instead (van Keken, 1993; Manea et al., 2004). The idea of penalty method is quite straightforward and consists in perturbation of the continuity equation with a small term containing the pressure: $\nabla \cdot \boldsymbol{v} + p\varepsilon = 0$. The pressure is then eliminated and thus the momentum equation and the continuity equation are uncoupled, which results in a large reduction of the system of equations (Codina, 1993). Moreover, any partial pivoting is not needed in this approach. In practical implementation, a choice $\varepsilon = 10^{-3} - 10^{-9}$ is recommended for 64 bits accuracy, i.e. double precision arithmetic on a 32-bits computer, although a good choice for ε may be hard to find in the case of non-Newtonian fluids (Cuvelier et al., 1986).

The penalty method is based on the proof that the solution of the Stokes equation with the perturbed continuity equation converges to the solution of the Stokes problem if $\varepsilon \to 0$ for general boundary conditions in the case of Newtonian fluid (Temam, 2001). Recently, it has been proved that the solution exists and is unique also in the case of power-law rheology (Lefton and Wei, 2001) and the penalty method converges in that case as well (Borggaard et al., 2008).

In this work, we use a different approach: the Stokes problem may be formally written as

$$K(\boldsymbol{u})\,\boldsymbol{u} = \boldsymbol{f}, \tag{3.17}$$

where K denotes a non-linear operator. An old, but still very popular, method of solving such a system of equations is the Picard method. In this iterative method, the non-linear operator K is applied to a vector $\boldsymbol{u}$ from the previous iteration (Cuvelier et al., 1986) and thus, in the i-th iteration, we solve the linear equation

$$K\left(\boldsymbol{u^{i-1}}\right)\boldsymbol{u^{i}} = \boldsymbol{f}, \tag{3.18}$$

for unknown $\boldsymbol{u}^i$. That is why the Picard method is sometimes called a successive substitution method. The Picard method is simple to implement and in general has a large region of convergence, which means that it does not need an accurate initial estimate. On the other hand, it converges slowly: if we denote the rate of convergence as λ, i.e.

$$\|\boldsymbol{u} - \boldsymbol{u}^{i-1}\| = \lambda \|\boldsymbol{u} - \boldsymbol{u}^i\|, \tag{3.19}$$

and require an accuracy of ε, then the iterative process should be terminated when

$$\|\boldsymbol{u}^{i-1} - \boldsymbol{u}^i\| \leq \frac{1-\lambda}{\lambda}\varepsilon. \tag{3.20}$$

Since often $\lambda \simeq 1$, the number of required iterations is generally large.

In computational fluid dynamics, the Picard iterations are usually used to linearize convective term $\boldsymbol{v} \cdot \nabla \boldsymbol{v}$ in the Navier-Stokes equation (3.2). As it has been shown above, this term can be neglected due to infinite Prandtl number, however, we will use the Picard method to treat the non-linear viscosity in equation (3.14).

Since the Stokes problem is coupled with the heat transfer equation, the Picard iterative scheme needs to be changed to

$$T^0 \to \boldsymbol{v}^1 \to T^1 \to \boldsymbol{v}^2 \to \cdots \to T^n \to \boldsymbol{v}^{n+1} \to T^{n+1} \to \boldsymbol{v}^{n+2} \to \cdots \tag{3.21}$$

In the case of Newtonian temperature-dependent viscosity, the Stokes equation is linear in $\boldsymbol{v}$ for a fixed temperature field and the heat transfer equation is linear in T for a fixed velocity field, so the possibility to use the iterative process described by iterative scheme (3.21) is obvious. For non-Newtonian fluids one may suspect to employ inner iterations to solve the Stokes problem but the numerical tests showed that for the studied class of rheology underrelaxation is a good way to achieve a sufficient convergence rate (Kukačka and Matyska, 2004), see details in Section 3.4.1.

3.2 Weak Formulation

It is quite common to write the fundamental physical laws in the differential form like equations (3.14) – (3.16) but their integral form is much more natural. Unlike the differential form, the integral form does not require smooth parameters in solved equations. Therefore, the weak formulation allows to solve the equations even in the case when they do not have a solution in the classical sense but it is obvious that their physical sense is well defined.

For instance, the Stokes equation (3.14) in fact assumes that the first derivatives of viscosity must be continuous. In the case of viscosity jumps, it would be necessary to divide the computational domain into parts, where this condition is fulfilled, and connect the solution at discontinuities correctly. The weak solution does not require such strict conditions and therefore, it is advantageous to employ it, namely, if the position of the discontinuities is not known in advance.

In order to derive the weak formulation of equation (3.14) for homogeneous Dirichlet boundary condition $\boldsymbol{v}|_{\delta\Omega} = 0$, let us define the vector space U^1 of divergence-free test functions $\boldsymbol{u}$, which satisfy the zero boundary condition at the domain boundary

$$U_0^1 = \{\boldsymbol{u} : \nabla \cdot \boldsymbol{u} = 0,\, \boldsymbol{u}|_{\partial\Omega} = 0,\, u_i \in L^2(\Omega),\, \frac{\partial u_i}{\partial x_j} \in L^2(\Omega),\, \forall i, j\}. \tag{3.22}$$

Multiplication the equation (3.14) by an arbitrary test function $\boldsymbol{u} \in U_0^1$ and integration over the whole domain Ω gives

$$-\int_\Omega \nabla \cdot \left(\eta \left(\nabla \boldsymbol{v} + (\nabla \boldsymbol{v})^T\right)\right) \cdot \boldsymbol{u} \mathrm{d}\Omega + \int_\Omega \boldsymbol{u} \cdot \nabla p \mathrm{d}\Omega = \int_\Omega \rho \boldsymbol{u} \cdot \boldsymbol{g} \mathrm{d}\Omega. \tag{3.23}$$

The Green's theorem applied to the individual terms of (3.23) yields

$$\int_\Omega \nabla \cdot (\eta \nabla \boldsymbol{v}) \cdot \boldsymbol{u} \mathrm{d}\Omega = \int_{\partial\Omega} \eta \boldsymbol{n} \cdot \nabla \boldsymbol{v} \boldsymbol{u} \mathrm{d}S - \int_\Omega \eta \nabla \boldsymbol{v} : \nabla \boldsymbol{u} \mathrm{d}\Omega, \tag{3.24}$$

$$\int_\Omega \nabla \cdot \left(\eta \left(\nabla \boldsymbol{v}\right)^T\right) \cdot \boldsymbol{u} \mathrm{d}\Omega = \int_{\partial\Omega} \eta \boldsymbol{u} \cdot \nabla \boldsymbol{v} \cdot \boldsymbol{n} \mathrm{d}S - \int_\Omega \eta \left(\nabla \boldsymbol{v}\right)^T : \nabla \boldsymbol{u} \mathrm{d}\Omega, \tag{3.25}$$

$$\int_\Omega \boldsymbol{u} \cdot \nabla p \mathrm{d}\Omega = \int_{\partial\Omega} p \boldsymbol{u} \cdot \boldsymbol{n} \mathrm{d}S - \int_\Omega p \nabla \cdot \boldsymbol{u} \mathrm{d}\Omega. \tag{3.26}$$

The integrals over the boundary $\partial\Omega$ vanish because the test functions satisfy the homogeneous boundary condition $\boldsymbol{u}|_{\partial\Omega} = 0$ and the second term in (3.26) vanishes as the test functions are divergence-free. Thus the equation (3.14) becomes

$$\int_\Omega \eta \left(\nabla \boldsymbol{v} + (\nabla \boldsymbol{v})^T\right) : \nabla \boldsymbol{u} \mathrm{d}\Omega = \int_\Omega \rho \boldsymbol{g} \cdot \boldsymbol{u} \mathrm{d}\Omega. \tag{3.27}$$

Defining the bilinear form

$$A\left(\boldsymbol{u}, \boldsymbol{v}\right) = 2 \int_\Omega \eta \dot{\boldsymbol{e}}\left(\boldsymbol{u}\right) : \dot{\boldsymbol{e}}\left(\boldsymbol{v}\right) \mathrm{d}\Omega \tag{3.28}$$

and the linear form

$$F\left(\boldsymbol{u}\right) = \int_\Omega \rho \boldsymbol{g} \cdot \boldsymbol{u} \mathrm{d}\Omega \tag{3.29}$$

the equation (3.27) may be written simply as: seek for $\boldsymbol{v} \in U_0^1$ such that

$$A\left(\boldsymbol{v}, \boldsymbol{u}\right) = F\left(\boldsymbol{u}\right), \qquad \forall \boldsymbol{u} \in U_0^1. \tag{3.30}$$

We may take the advantage of such a formulation also if the inhomogeneous boundary condition $\boldsymbol{v}|_{\partial\Omega} = \boldsymbol{v}_0$ is prescribed. Then the weak solution may be sought in the form $\boldsymbol{v} = \boldsymbol{v'} + \boldsymbol{v}_0$, where $\boldsymbol{v'} \in U_0^1$ and $\boldsymbol{v}_0 \in U^1$. The vector space U^1 is given by

$$U^1 = \{\boldsymbol{u} : \nabla \cdot \boldsymbol{u} = 0,\, u_i \in L^2(\Omega),\, \frac{\partial u_i}{\partial x_j} \in L^2(\Omega),\, \forall i, j\}, \tag{3.31}$$

and $\boldsymbol{v'}$ must satisfy

$$A\left(\boldsymbol{v'}, \boldsymbol{u}\right) = F\left(\boldsymbol{u}\right) - A\left(\boldsymbol{v}_0, \boldsymbol{u}\right), \qquad \forall \boldsymbol{u} \in U_0^1. \tag{3.32}$$

If we consider the impermeable boundary with the free-slip

$$\boldsymbol{v} \cdot \boldsymbol{n} = 0, \tag{3.33}$$

$$\boldsymbol{D} \cdot \boldsymbol{n} - \boldsymbol{n} \cdot \boldsymbol{D} \cdot \boldsymbol{n}\boldsymbol{n} = 0, \tag{3.34}$$

define the vector space V^1 such that

$$V^1 = \{\boldsymbol{u} : \nabla \cdot \boldsymbol{u} = 0,\, \boldsymbol{u} \cdot \boldsymbol{n}|_{\partial\Omega} = 0,\, u_i \in L^2(\Omega),\, \frac{\partial u_i}{\partial x_j} \in L^2(\Omega)\}, \tag{3.35}$$

apply the Green's theorem, and rewrite the integrals over domain boundary

$$\begin{aligned}\int_{\partial\Omega} \eta \boldsymbol{n} \left(\nabla \boldsymbol{v} + (\nabla \boldsymbol{v})^T\right) \cdot u \mathrm{d}S = \int_{\partial\Omega} \eta \boldsymbol{n} \cdot \left(\nabla \boldsymbol{v} + (\nabla \boldsymbol{v})^T\right) \cdot \boldsymbol{u}_t \mathrm{d}S = \\ = \int_{\partial\Omega} \eta \left(\boldsymbol{n} \cdot \boldsymbol{D} - \boldsymbol{n} \cdot \boldsymbol{D} \cdot \boldsymbol{n}\boldsymbol{n}\right) \cdot \boldsymbol{u}_t \mathrm{d}S,\end{aligned}$$

where $\boldsymbol{u}_t$ is tangential velocity, then the weak solution $\boldsymbol{v} \in V^1$ may be defined by

$$A\left(\boldsymbol{v}, \boldsymbol{u}\right) = F\left(\boldsymbol{u}\right), \qquad \forall \boldsymbol{u} \in V^1, \tag{3.36}$$

due to zero boundary condition on tangential force (3.34). Thus, the weak solution of the system of equations (3.14) – (3.15) for boundary conditions on velocity and free-slip boundary conditions differ only in the vector space of test functions. Furthermore, it may be shown that the formulation

$$A\left(\boldsymbol{v}, \boldsymbol{u}\right) = F\left(\boldsymbol{u}\right), \qquad \forall \boldsymbol{u} \in U^1, \tag{3.37}$$

naturally incorporates the no-force boundary conditions (Matyska, 1996).

The weak solution of equation (3.16) may be defined in a similar way. Introducing the vector spaces H_0^1 and H^1 of test function τ such that

$$H_0^1 = \{\tau : \tau|_{\partial\Omega} = 0,\, \tau \in L^2(\Omega),\, \frac{\partial \tau}{\partial x_i} \in L^2(\Omega)\} \tag{3.38}$$

$$H^1 = \{\tau : \tau \in L^2(\Omega),\, \frac{\partial \tau}{\partial x_i} \in L^2(\Omega)\} \tag{3.39}$$

yields the weak formulation

$$\int_\Omega k \nabla T \cdot \nabla \tau \mathrm{d}\Omega + \int_\Omega \tau \rho c_p \boldsymbol{v} \cdot \nabla T \mathrm{d}\Omega = \int_\Omega \tau \boldsymbol{D} : \nabla \boldsymbol{v} \mathrm{d}\Omega \tag{3.40}$$

from where the integral over the domain boundary $\partial\Omega$ disappeared if of homogeneous boundary conditions are assumed. Such a formulation includes either zero temperature

boundary conditions (then the solution $T \in H_0^1$) or zero heat flux conditions (then $T \in H^1$). The important fact is that also the weak formulation of the heat transfer equation may be formally written again as

$$A(\boldsymbol{u}, \boldsymbol{v}) = F(\boldsymbol{u}), \qquad \forall \boldsymbol{u} \in H_0^1 \qquad \text{or} \qquad \forall \boldsymbol{u} \in H^1. \tag{3.41}$$

In the case of a non-homogeneous mixed boundary condition $\frac{\partial T}{\partial \boldsymbol{n}} = G$ applied on a part Γ of the boundary, an integral $\int_\Gamma \tau G \mathrm{d}s$ needs to be included to the linear form F, see Křížek and Neittaanmäki (1990) for details.

The principle of the numerical method based on weak formulations consists in approximation of the vector space of test functions U with the subspace U_h of discrete functions $\boldsymbol{u}_h$. The solution $\boldsymbol{v}$ is supposed to be from the space U_h (H_h) as well. Thus the discrete formulation is: we are searching for $\boldsymbol{v}_h \in U_h$ satisfying

$$A\left(\boldsymbol{v}_h, \boldsymbol{u}_h\right) = F\left(\boldsymbol{u}_h\right), \qquad \forall \boldsymbol{u}_h \in U_h. \tag{3.42}$$

Such an approach is called the Galerkin approximation (Křížek and Neittaanmäki, 1990). It is sufficient if the above equation is fulfilled for all the base functions $\boldsymbol{u}_i$. The discrete solution $\boldsymbol{v}_h$ may naturally be written as $\boldsymbol{v}_h = \sum_i c_i \boldsymbol{u}_i$ and equation (3.42) is then the set of equations for unknown coeffiecients c_i

$$a_{ij} c_j = f_i, \tag{3.43}$$

where $a_{ij} = A(\boldsymbol{u}_i, \boldsymbol{u}_j)$ is called from the historical reasons the stiffness matrix and $f_i = F(\boldsymbol{u}_i)$ the load vector. The key point of equation (3.43) consists of the fact that the base functions may be chosen in such a way that the resulting stiffness matrix a_{ij} is sparse and more effective algorithms may be utilized for numerical solution of this set of the equations.

3.3 Solution in Rectangular Domains

In the case of fluid flow in a 2-D domain, the continuity equation (3.15) is easily fulfilled by defining

$$v_1 = \frac{\partial \psi}{\partial x_2}, \qquad v_2 = -\frac{\partial \psi}{\partial x_1}. \tag{3.44}$$

The function ψ is called the stream function because its isolines are stream lines (that is such lines that are tangent to the velocity vector at any given time). By definition, the component of the velocity normal to a stream line is always zero so there is no mass flux across a stream line.

The bilinear form (3.28) may be rewritten by means of the stream function to the form

$$A(\psi, \xi) = \int_\Omega \eta \left(\frac{\partial^2 \psi}{\partial x_1^2} - \frac{\partial^2 \psi}{\partial x_2^2} \right) \left(\frac{\partial^2 \xi}{\partial x_1^2} - \frac{\partial^2 \xi}{\partial x_2^2} \right) \mathrm{d}\Omega + 4 \int_\Omega \eta \frac{\partial^2 \psi}{\partial x_1 \partial x_2} \frac{\partial^2 \xi}{\partial x_1 \partial x_2} \mathrm{d}\Omega \tag{3.45}$$

and the vector space U^2, analogical to U^1, is defined then as

$$U^2 = \{\xi : \frac{\partial \xi}{\partial x_i} \in L^2(\Omega), \frac{\partial^2 \xi}{\partial x_i \partial x_j} \in L^2(\Omega)\}, \tag{3.46}$$

where curl $= \left(\frac{\partial}{\partial x_2}, -\frac{\partial}{\partial x_1}\right)$ denotes the rotation of a scalar function.

If the computational domain is a rectangle, the staggered grid may be used: The rectangle domain $\Omega = \langle 0, a\rangle \times \langle 0, b\rangle$ is divided into rectangular elements by the nodal points

$$\begin{aligned} x_1^0 = 0, x_1^1 = h_1^1, x_1^2 = h_1^2, \ldots, x_1^{n-1} = a - h_1^n, x_1^n = a, \\ x_2^0 = 0, x_2^1 = h_2^1, x_2^2 = h_2^2, \ldots, x_2^{m-1} = b - h_2^m, x_2^m = b, \end{aligned} \tag{3.47}$$

and the basis function ξ^{ij} is the cartesian product $\xi^{ij}(x_1, x_2) = \phi^i(x_1)\phi^j(x_2)$ of the cubic elementary basis functions $\phi^k(x_s)$, $s = 1, 2$, which are uniquely determined by the relations

$$\phi^{2k-1}(x_s^l) = \delta_{kl}, \qquad \frac{\mathrm{d}\phi^{2k-1}}{\mathrm{dx}}(x_s^l) = 0, \tag{3.48}$$

$$\phi^{2k}(x_s^l) = 0, \qquad \frac{\mathrm{d}\phi^{2k}}{\mathrm{d}x}(x_s^l) = \delta_{kl}. \tag{3.49}$$

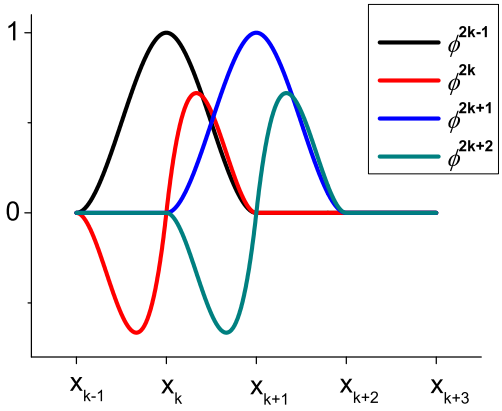

Figure 3.1: Schematic graph of the elementary base functions ϕ which the base functions $\xi^h \in U^2$ are composed from: $\xi^h = \phi^{h1}(x_1)\phi^{h2}(x_2)$.

The condition $\frac{\mathrm{d}^2\phi}{\mathrm{d}x^2} \in L^2(\langle 0, l\rangle)$ yields together with (3.48) the analytical form of the elementary base functions

$$\phi^{2i-1}(x) = -2(x - x^{i-1})^2(x - x^i - h_i/2)/h_i^3, \qquad x \in K_i \tag{3.50}$$

$$\phi^{2i-1}(x) = 2(x - x^{i+1})^2(x - x^i + h_{i+1}/2)/h_{i+1}^3, \qquad x \in K_{i+1} \tag{3.51}$$

$$\phi^{2i}(x) = (x - x^{i-1})^2(x - x^i)/h_i^2, \qquad x \in K_i \tag{3.52}$$

$$\phi^{2i}(x) = (x - x^{i+1})^2(x - x^i)/h_{i+1}^2, \qquad x \in K_{i+1} \tag{3.53}$$

$$\phi^{2i-1}(x) = \phi^{2i}(x) = 0, \qquad x \in \langle 0, l\rangle \setminus \left(K_i \bigcup K_{i+1}\right), \tag{3.54}$$

where $K_i = \langle x^{i-1}, x^i \rangle$ and $h_i = x^i - x^{i-1}$.

The basis functions τ^{ij} is defined again as the cartesian product $\tau_{ij}(x_1, x_2) = \theta^i(x_1)\theta^j(x_2)$ of the piece-wise linear functions uniquely determined by the relation

$$\theta^k(x_s^l) = \delta_{kl}. \tag{3.55}$$

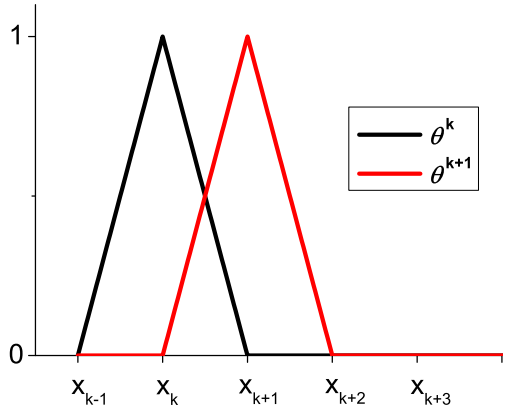

Figure 3.2: Schematic graph of the elementary base functions θ which the base functions $\tau^h \in H^1$ are composed from: $\tau^h = \theta^{h1}(x_1)\theta^{h2}(x_2)$.

3.4 Numerical Solution

As shown in the previous sections, any practical implementation of the finite element method reduces to solving a system of linear equations (3.43). Numerical solution requires two main issues to be solved: Firstly, an appropriate method for solution of usually large number of linear equations must be chosen. Secondly, individual terms in linear equations are formed by integrals and therefore, a fast but accurate method of numerical integration needs to be implemented.

3.4.1 Implementation of Code

The numerical solution of the iterative scheme (3.21) in terms of the temperature and the stream function

$$T^0 \to \psi^1 \to T^1 \to \psi^2 \to \cdots \to T^n \to \psi^{n+1} \to T^{n+1} \to \psi^{n+2} \to \cdots \tag{3.56}$$

has been implemented in C++. Each iteration therefore consists of two parts: first, the equation of the form (3.43) for the temperature and then for the stream function are solved. The elements of the stiffness matrix a_{ij} and the right hand side f_i are evaluated using 4-points Gauss rule for numerical integration. The resulting system of algebraic equations

is solved by the Gaussian elimination for sparse matrices since iterative methods like the conjugate gradient method showed a poor convergency, particularly, in the case of a non-linear viscosity or high viscosity contrasts in different parts of the computational domain. For the elimination the algorithm used in Y12M library (Zlatev, 1981) has been ported to C++.

In the practical numerical implementation, the convergence of the iterative scheme (3.56) requires underrelaxation to avoid possible oscillations in the iterative process. It means that the modified temperature $\hat{T}^n$ given by

$$\hat{T}^n = \beta_T T^n + (1 - \beta_T) T^{n-1} \,, \tag{3.57}$$

is used in the n-th iteration of the Stokes equation and the modified stream function $\hat{\psi}^n$ given by

$$\hat{\psi}^n = \beta_\psi \psi^{n-1} + (1 - \beta_\psi) \psi^{n-2}, \tag{3.58}$$

is used in n-th iteration of the heat transfer equation. Parameters β_T and β_ψ are the damping parameters from the interval $(0, 1\rangle$. The optimal values of the damping parameters differ from case to case but the values between 0.2 and 0.5 were sufficient in most cases.

The iterative process starts with a solution of the heat transfer equation with zero velocity which is in equation (3.56) denoted as T_0. Although the used Picard method usually converges from almost any initial guess, its convergence is poor (if any) in the case that the viscosity is a non-linear function of the velocity (the stream function). Therefore, in several first iterations (usually three or four) only the temperature-dependence of the viscosity is taken into account. Moreover, the dissipative term $\boldsymbol{D} : \nabla \boldsymbol{v}$ in the heat transfer equation needs to be underrelaxed as well with a damping parameter less than 0.2. The iterative process stops when several criteria are reached: Since the solution is sought in the form of series $T = c_i^T \xi_i$ and $\psi = c_i^\psi \psi_i$, the difference of norms of vectors c_i^T and c_i^ψ in two subsequent iterations is a good termination criteria. Besides those, also root-mean squared velocity $v_{rms} = \sqrt{\int_\Omega (v_1^2 + v_2^2)\, \mathrm{d}\Omega}$ and the derivatives of the temperature at the boundary (surface heat flow) are used.

3.4.2 Numerical Integration

The general form of numerical integration formulas reads

$$\int_K f(x) \mathrm{d}x = \sum_{q=1}^{Q} c_q^K f\left(P_q^K\right), \tag{3.59}$$

where c_q^K are coefficients and P_q^K nodes of the integration formula. For one-dimensional integration the interval K may be mapped to the reference interval $\hat{K} = \langle -1, 1\rangle$, in which the integrals in the form of (3.59) can be evaluated using Gaussian formulas.

$$\int_{-1}^{1} f(x) \mathrm{d}x = \sum_{q=1}^{Q} \hat{c}_q f\left(\hat{P}_q\right), \tag{3.60}$$

Q	$\hat{P}_q$	$\hat{c}_q$
1	0	2
2	$\pm\sqrt{3}/3$	1
3	$\pm\sqrt{15}/5$	5/9
	0	8/9
4	$\pm\sqrt{\left(15+2\sqrt{30}\right)/35}$	$1/2-\sqrt{30}/36$
	$\pm\sqrt{\left(15-2\sqrt{30}\right)/35}$	$1/2+\sqrt{30}/36$

Table 3.1: Gaussian points $\hat{P}$ (roots of the Legendre polynomials) and the corresponding coefficients for Q-point Gaussian integration formula.)

where coefficients and nodes are given in Table 3.1. The Q-point Gaussian rule is exact for all polynomials of degree $2Q-1$. In case of integration over K, the corresponding coefficients must be re-evaluated as

$$c_q^K = \hat{c}_q \frac{\operatorname{meas} K}{2}.$$

Integration over 2-dimensional rectangular domain K then yields

$$\int_K f(x_1,x_2) = \frac{1}{4}\operatorname{meas} K \sum_{i=1,\,j=1}^{M,\,N} f\left(P_i,P_j\right). \tag{3.61}$$

3.4.3 Construction of Boundary Conditions

Later, a rectangular domain will be used to model the flow of subducting plate. Here it is shown how boundary conditions may be constructed in one particular case. In Sections 4.1, 4.3, and 4.4, also modified boundary conditions are used but these might be constructed in a similar way, too.

The inflow and the outflow are prescribed at some parts of the boundary and at the rest, either the zero force condition or the free-slip condition with zero normal velocity is applied. The used boundary conditions are schematically shown in Figure 3.3: the inflow to the domain is considered at the left boundary between points A and B, whereas the outflow is considered at the bottom boundary between points C and D. The boundary conditions in the stream formulation for the following case are considered:

- Top boundary
  Free-slip condition with zero normal component of velocity

- Bottom boundary
  Prescribed outflow between C and D and zero force condition on the rest

- Left boundary
  Zero force condition from the bottom up to A and free-slip condition with prescribed normal component of velocity on the rest

- Right boundary
  Zero force condition

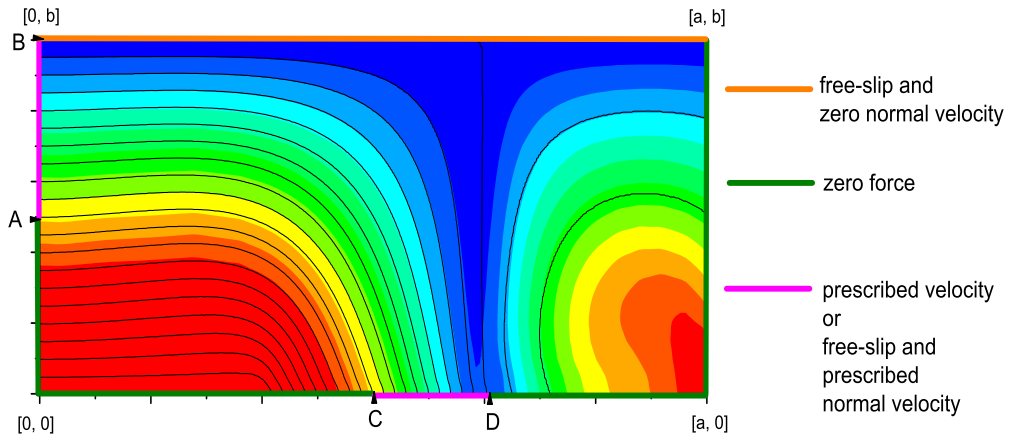

Figure 3.3: Schematic picture of applied boundary conditions in the case of subducting flow model in a rectangular domain. Stream lines illustrating the flow field and the corresponding temperature field are shown as well.

Since the stream function is not unique, it is necessary to specify its value at some point to make it unique. Because of reasons discussed later, we put $\psi = 0$ at $[0, 0]$. Then the above boundary conditions mean

$$\begin{aligned}
\psi(x_1, 0) &= 0 \quad x_1 \in \langle 0, C\rangle \\
\frac{\partial \psi}{\partial x_1}(x_1, 0) &= -v_y^{\text{out}} \quad x_1 \in \langle C, D\rangle \\
\frac{\partial \psi}{\partial x_2}(x_1, 0) &= v_x^{\text{out}} \quad x_1 \in \langle C, D\rangle \\
\psi(D, 0) = \psi_H &= -\int_C^D v_y^{\text{out}} \mathrm{d}x_1 \\
\psi(x_1, 0) &= \psi_H \quad x_1 \in \langle D, a\rangle \\
\psi(a, x_2) &= \psi_H \quad x_2 \in \langle 0, b\rangle \\
\psi(x_1, b) &= \psi_H \quad x_1 \in \langle 0, a\rangle \\
\psi(0, x_2) &= 0 \quad x_2 \in \langle 0, A\rangle \\
\frac{\partial \psi}{\partial x_2}(0, x2) &= v_x^{\text{in}} \quad x_2 \in \langle A, B\rangle \\
\psi(0, B) &= \int_A^B v_x^{\text{in}} \mathrm{d}x_2
\end{aligned}$$

Since the mass flow through the boundary between A and B and between C and D is required to be the same, the above conditions require $-\int_C^D v_y^{\text{out}} \mathrm{d}x_1 = \int_A^B v_x^{\text{in}} \mathrm{d}x_2$. When the base functions are such that the points A, C, and D coincide with some of discretization points (3.47) the test functions from U^2 may be utilized in construction of the boundary conditions on the stream function.

$$\begin{aligned}\varphi \;&= \phi^{2m+1}(x_2)\,(1-\phi^{2n+1}(x_1)-\phi^{-1}(x_1))\\ &+\phi^{2n+1}(x_1)\,(1-\phi^{-1}(x_2))\\ &+\phi^{-1}(x_1)S(A,B,x_2)+\phi^{-1}(x_2)S(C,D,x_1)\\ &+\phi^{0}(x_2)S(C,D,x_1)\end{aligned} \tag{3.62}$$

where S is defined by

$$S(\alpha,\beta,x)=\begin{cases}0, & x<\alpha\\ \frac{x-\alpha}{\beta-\alpha}, & \alpha\le x\le\beta\\ 1, & x>\beta.\end{cases} \tag{3.63}$$

3.5 Benchmarks

Flow in a square cavity has been used for benchmarking the quality of the convection codes for more than 25 years. In geophysical applications, it is not possible to use the standard benchmarks (de Vahl David and Jones, 1983) since these classical tests calculate the flow of the air, in which the Prandtl number is about 0.71. Therefore, mantle convection codes are tested on a specific set of benchmark tests.

3.5.1 Description of Tests

The standard geophysical benchmark (Blankenbach et al., 1989) defines several numerical tests of a Boussinesq fluid flow calculation with an infinite Prandtl number. We are concerned only to the steady-state flow of a Boussinesq fluid in which the viscous dissipation is not taken into account. It is described by the set of equations

$$\text{div } \mathbf{v} = 0, \tag{3.64}$$

$$-\text{grad } p + \eta\nabla^2\boldsymbol{v} + \rho\boldsymbol{g}\alpha(T-T_0) = 0, \tag{3.65}$$

$$\rho c_p \boldsymbol{v}\cdot\nabla T = k\nabla^2 T, \tag{3.66}$$

The test assumes the natural convection in the rectangular domain $\Omega = \langle 0, h\lambda\rangle \times \langle 0, h\rangle$ with the free-slip boundary condition on velocity at the whole boundary $\partial\Omega$. The temperature is fixed to T_0 at the top and $T_0 + \Delta T$ at the bottom while the left and right sides of the domain are insulated, which means the condition of zero heat flux $\frac{\partial T}{\partial \boldsymbol{n}} = 0$ (see Figure 3.4).

The following quantities are calculated for the comparison:

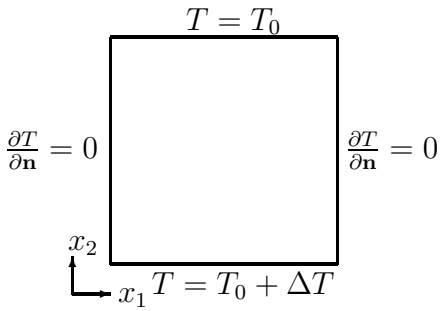

Figure 3.4: The square domain (aspect ratio $\lambda = 1$) and boundary conditions on temperature used for benchmarking.

	λ	η_0[Pas]	b	c
1a	1	10^{23}	0	0
1b	1	10^{22}	0	0
1c	1	10^{21}	0	0
2a	1	10^{23}	ln(1000)	0
2b	2.5	10^{23}	ln(16384)	ln(64)

Table 3.2: Description of benchmark tests.

1. Nusselt number
   $Nu = -\frac{\int_0^h \partial_{x_1} T(x_1, x_2=h) \mathrm{d}x_1}{T(x_1=0, x_2=0)}$,
   which is the ratio between convective and conductive heat transfer[1].

2. Non-dimensional root-mean-squared velocity
   $v_{rms} = \frac{1}{h^2 \kappa} \sqrt{\int_\Omega (v_1^2 + v_2^2) \, \mathrm{d}\Omega}$

3. Temperature gradients $q_c = \frac{-h}{\Delta T} \frac{\partial T}{\partial x_2}(x_1, x_2)$ in the corners of the region Ω, which are denoted $q_1 = q_c(0, h)$, $q_2 = q_c(h\lambda, h)$, $q_3 = q_c(h\lambda, 0)$, and $q_4 = q_c(0, 0)$.

These defined tests differ in Rayleigh number[2] and in the aspect ratio λ. The non-linear viscosity is used in the form

$$\eta = \eta_0 \exp\left(-\frac{bT}{\Delta T} + c\frac{(h - x_2)}{h}\right). \tag{3.67}$$

[1] A Nusselt number of order unity indicates a sluggish motion little more effective than pure fluid conduction; a large Nusselt number means very efficient convection.

[2] The non-dimensional form of equation (3.65) in the case of constant viscosity may be written in the form $-\nabla p + \nabla^2 \boldsymbol{v} + \mathrm{Ra}(T - T_0)\boldsymbol{g_0} = 0$, where $\mathrm{Ra} = \frac{\alpha d^3 g_0 \Delta T \rho}{\eta \kappa}$ is the Rayleigh number characterizing the heat transfer within the fluid. The Raylegh number expresses the ratio between the magnitude of the buoyancy force caused by temperature variations and viscous stresses.

The calculated tests are described in Table 3.2. Other used parameters are summarized in Table 3.3.

h	length of side	10^6	m
T_0	reference temperature	0	°C
ΔT	temperature jump	1000	°C
g	gravity acceleration	10	ms^{-2}
κ	thermal diffusivity	10^{-6}	$\mathrm{m}^2\mathrm{s}^{-1}$
η	dynamic viscosity	$10^{23}, 10^{22}, 10^{21}$	Pas
α	thermal expansivity	2.5×10^{-5}	K^{-1}
ρ	density	4000	kgm^{-3}

Table 3.3: Values of parameters used in benchmark tests.

3.5.2 Benchmarks Results

The results calculated for different grids are presented in the following tables.

1a	ψ : 20×20 T: 36×36	36×36 78×78	50×50 100×100	true solution
Nu	4.89652	4.89256	4.88898	4.8844
v_{rms}	42.9746	42.8942	42.8742	42.865
q_1	8.06454	8.06575	8.05986	8.0593
q_2	0.58182	0.58916	0.58885	0.5888
1b				
Nu	10.4278	10.5428	10.545	10.534
v_{rms}	193.207	193.331	193.254	193.215
q_1	18.7229	19.0714	19.0864	19.079
q_2	0.71685	0.72226	0.72273	0.72275
1c				
Nu	20.932	21.9677	21.974	21.972
v_{rms}	835.135	834.411	834.409	833.98
q_1	41.7578	45.8535	45.928	45.964
q_2	0.81575	0.87291	0.8724	0.8722

Table 3.4: Results of the tests with constant viscosities 1a – 1c calculated for different grids. The grids are described by the number of nodes in each coordinates for the Stokes equation and the heat transfer equation. The true solution means the best estimate of solution recommended to use for validation of codes (Blankenbach et al., 1989). The values q_3 and q_4 are not shown as the symmetry yields $q_1 = q_3$ and $q_2 = q_4$ which has been confirmed for used symmetric grid.

2a	ψ: 20×20 T: 36×36	36×36 78×78	50×50 100×100	true solution
Nu	10.0605	10.0921	10.0827	10.066
v_{rms}	481.768	480.347	480.46	480.433
q_1	17.4546	17.5656	17.5606	17.531
q_2	1.01092	1.00864	1.00842	1.008
q_3	24.0761	26.7520	26.8364	26.808
q_4	0.46007	0.495525	0.49615	0.497

Table 3.5: Results of the test 2a calculated for different grids. The same grids as in Table 3.4 were used.

2b	ψ: 66×36 T: 92×36	66×36 100×80	true solution
Nu	6.89726	6.94144	6.9299
v_{rms}	171.337	171.694	171.755
q_1	18.1774	18.4949	18.484
q_2	0.17622	0.17671	0.1774
q_3	14.0238	14.1723	14.168
q_4	0.61661	0.61756	0.617

Table 3.6: Results of the test 2b calculated for different grids. The used grids are described similarly as in Table 3.4.

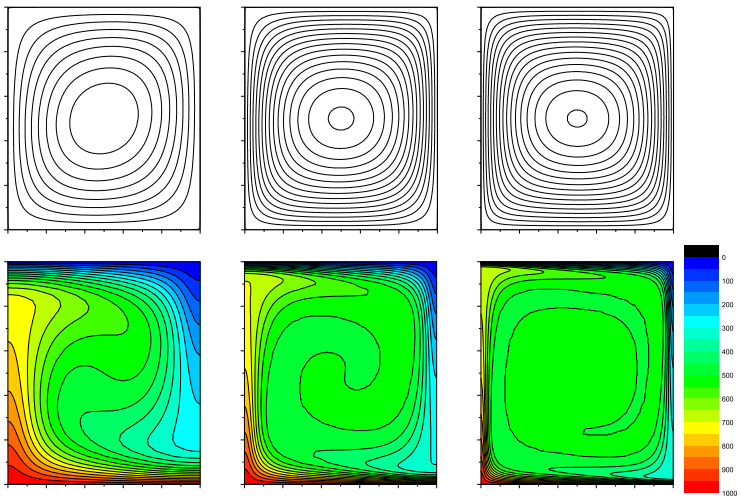

Figure 3.5: Stream function (top) and temperature (bottom) calculated for benchmark tests with constant viscosities 1a (left) – 1c (right). Stream function contour interval is 2×10^{-6} (1a), 5×10^{-6} (1b), and 2×10^{-5} (1c).

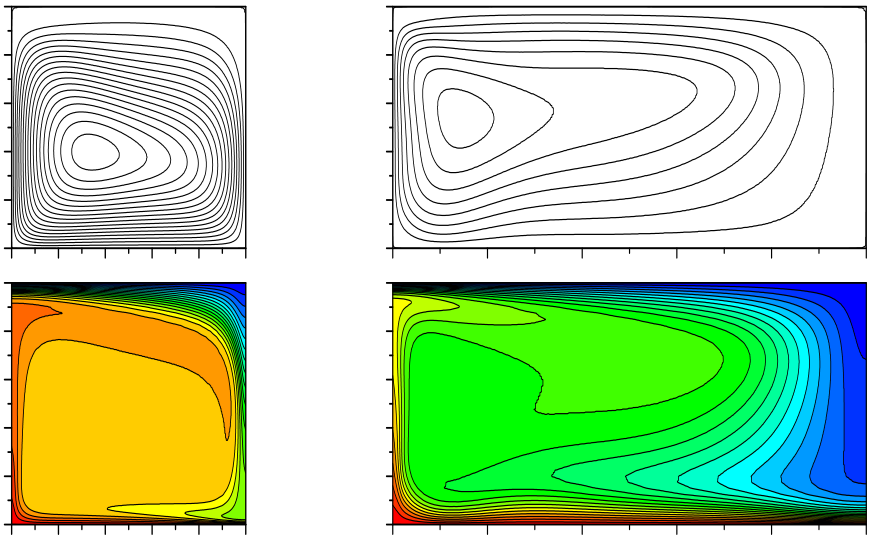

Figure 3.6: Stream function (top) and temperature (bottom) calculated for benchmark tests with temperature- and depth-dependent viscosities 2a (left) and 2b (right). Stream function contour interval is 1×10^{-5}, temperature scale same as in Figure 3.5.

From the presented results we may conclude that the developed code is sufficiently accurate: all derived quantities fall within 1.5% of the best estimate (Blankenbach et al., 1989) in the case of the coarse grid and within 0.2% of the best estimate in the finer grid is used.

Chapter 4

Numerical Models of Subduction

The aim of this study is to apply a rheology to the lithosphere so as to generate plate-like behaviour in subduction zones in a steady-state wedge model. As discussed in Section 2.4.2, nowadays, it is quite common to use kinematic models with a prescribed position of the slab-wedge interface (Peacock, 1996) and these models are primarily used to calculate the temperature field both in the subducting slab and the wedge (van Keken et al., 2002; Peacock et al., 2005). Quite recently these models have been used to explain anisotrophy observed in subduction zones (Long et al., 2007; Kneller et al., 2007). The notable weakness of these kinematic models consists of the fact that the geometry of the subducting slab is prescribed a priori and thus the deformation of the slab is excluded from these models (King, 2001). Although the position of the slab-wedge interface is known relatively well from seismic tomography, it is clear that the interface position should be also an outcome of the modelling; imposing the interface into the model in advance is somewhat ad hoc, not fully consistent with the rest of the model. Moreover, the slab dip angle could provide an important constraint on slab rheology. Although traditional geodynamics suggested there is a trade-off between the slab age and the dip angle, such a correlation have not been found (Jarrad, 1986; Cruciani et al., 2005). Therefore, there must be other factors that influence the dip angle, in a way which has not been understood yet, and the rheology of the crust is the most likely one.

If we had a kinematic model allowing self-consistent creation of the contact between the plates, it would be of interest to find a rheology which produces the plate-like behaviour pattern naturally. Such a model would lever out also some objections against kinematic models: particularly, the most important one – rigid behaviour of the subducting plate – would be solved.

The developed method, which is presented below, allows calculating the steady-state temperature field in the subducting plate and the adjacent mantle wedge without the position of their interface being prescribed in advance. The position of this interface is a part of the solution, however, the model remains kinematic, i.e. the flow is driven by velocity boundary conditions. Another advantage of the presented model consists in an inartificial inclusion of dissipative heat at the contact, which might play an important role in the temperature structure of the wedge, particularly forearc, but is handled quite

arbitrary as a free parameter in the current models (van Keken et al., 2002). In next sections, the principle of the method will be explained and an application to a generic subduction zone model will be given.

4.1 Semi-kinematic Subduction Model

The principle of presented semi-kinematic[1] modelling stems from the fact that the viscosity may be treated as a function of the stream function. This might be surprising at the first glance but in fact it is a mathematical trick how to separate different materials without any assumptions about the position of their interface.

Let's assume the Stokes flow described by the system of equations (3.14) – (3.16) in a rectangular domain depicted in Figure 4.1. For the Stokes equation the free-slip boundary condition with prescribed normal component of velocity

$$\boldsymbol{v} \cdot \boldsymbol{n} = v_0, \tag{4.1}$$

$$\boldsymbol{D} \cdot \boldsymbol{n} - \boldsymbol{n} \cdot \boldsymbol{D} \cdot \boldsymbol{n}\boldsymbol{n} = 0, \tag{4.2}$$

is applied on the top and the bottom of the model. The normal velocity $v_0 = 0$ except for that part of the bottom boundary, where the non-zero outflow is prescribed. On the left and the right sides, the no-force condition

$$\boldsymbol{D} \cdot \boldsymbol{n} = 0 \tag{4.3}$$

is used. If we denote the width of the outflow at the bottom as H, then we may set the stream function at the left-most point of the outflow to be zero and consequently the value of the stream function at the right-most point of the outflow is given by

$$\psi_B = \int_H v_0 \mathrm{d}x = H v_0. \tag{4.4}$$

In Figure 4.1, the flow pattern, which develops in the case of constant viscosity in the whole domain, is depicted. It may be easily seen that the contour ψ_B of the stream function separates the fluid coming from the left inflow from the rest of the model. Thus we may model the subducting plate as fluid bounded by two stream lines: $\psi = 0$ at the bottom and $\psi = \psi_B$ at the top.

Although this semi-kinematic model is limited to the steady state, it does not seem to be harmful, since most mantle wedge models are steady-state only (e.g. Peacock, 1993; Peacock et al., 2005).

[1]The model is kinematic since normal velocities are prescribed at the boundaries, i.e inflow and outflow are given, and the name "semi-kinematic" has been chosen to emphasize the difference between the presented model and the usual kinematic wedge models. A note should be made here that tangential velocities at the boundaries are sometimes prescribed even in dynamic models, i.e. in models where the flow is driven by buoyancy (Eberle et al., 2002), so the name "kinematic" is to be used when the prescribed velocity boundary conditions mean inflow or outflow.

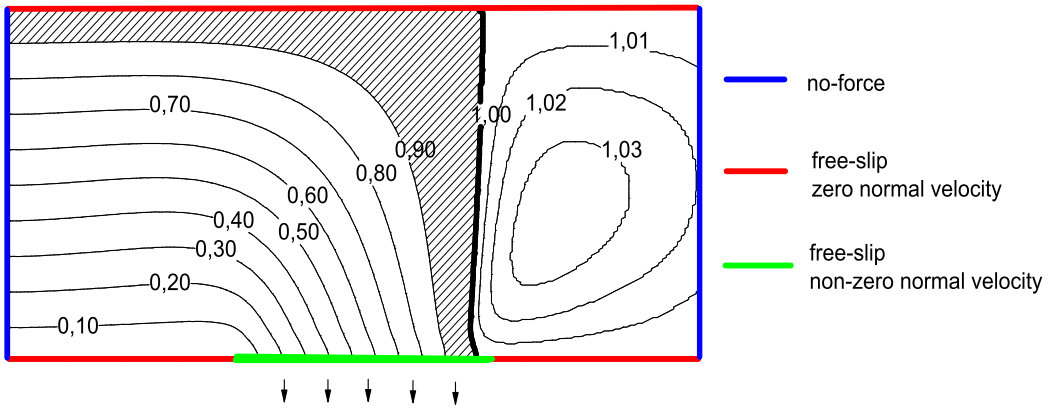

Figure 4.1: Scheme of the rectangular domain 300 × 100 km showing the flow pattern developed in the case of a constant viscosity. The stream function is scaled by the value ψ_B so as the slab-wedge interface is marked with the contour line $\psi = 1$.

4.2 Plate Contact

We utilized the principle described in the previous section (Kukačka and Matyska, 2004) in order to model the contact between the subducting plate and the overriding one. In the rectangular domain 300 km × 100 km depicted in Figure 4.1, we calculated the Stokes flow with the viscosity of the Arrhenius type

$$\eta = \eta_{\max} f(\psi) \exp\left(-\frac{\ln(K_t)T}{\Delta T}\right), \tag{4.5}$$

where $f(\psi)$ is a piece-wise function defined as

$$f(\psi) = \begin{cases} w, & \psi \in \langle (1-\delta_w)\psi_B, \psi_B \rangle, \quad 0 < \delta_w < 1 \\ 1, & \text{elsewhere} \end{cases} \tag{4.6}$$

Thus, we imposed a zone of weakness with the viscosity $\eta = w\eta_{\max}$ at the top of the subducting plate. We set its thickness to be approximately 10% of the overall thickness of the subducting slab by putting $\delta_w = 0.1\psi_B$. As the considered plate is 100 km thick, the thickness of the weakening zone is slightly higher than the thickness of the oceanic crust, however, this setting, which allows using a coarse grid and save some CPU, is evincible as not only the crust but also the uppermost portion of the oceanic lithosphere is supposed to be weak. The temperature at the top of the model is set to 0°C while at the bottom the temperature is set to 1200°C except the outflow where zero heat flux is applied. At the left and the right sides the oceanic geotherm giving surface heat flow 80 mWm^{-2} is prescribed.

We carried out a parametric study changing the viscosity reduction w for different slab velocities (Kukačka and Matyska, 2004). The resulting temperature fields and viscosity distributions are shown in Figures 4.2 – 4.4. Although the viscosity given by equation (4.5)

is a long way from what might be a realistic viscosity, the subducting plate is separated from the overriding one if the weakening w is sufficient, i.e. if the viscosity of the topmost part of the subducting plate is by about several orders of magnitude less than the viscosity of the overriding plate. The plate-like behaviour is developed if the weakening factor w is less than 10^{-2}. Moreover, it may be easily seen that the dip angle depends on the weakening factor w as well: higher weakening results in a less steep dip angle of subducting plates.

density	ρ	3300	kgm^{-3}
thermal conductivity in continental crust	k	2.5	$\mathrm{Wm}^{-1}\mathrm{K}^{-1}$
thermal conductivity elsewhere	k	3.1	$\mathrm{Wm}^{-1}\mathrm{K}^{-1}$
specific heat	c_p	1250	$\mathrm{Jkg}^{-1}\mathrm{K}^{-1}$

Table 4.1: The values of various parameters used in the model.

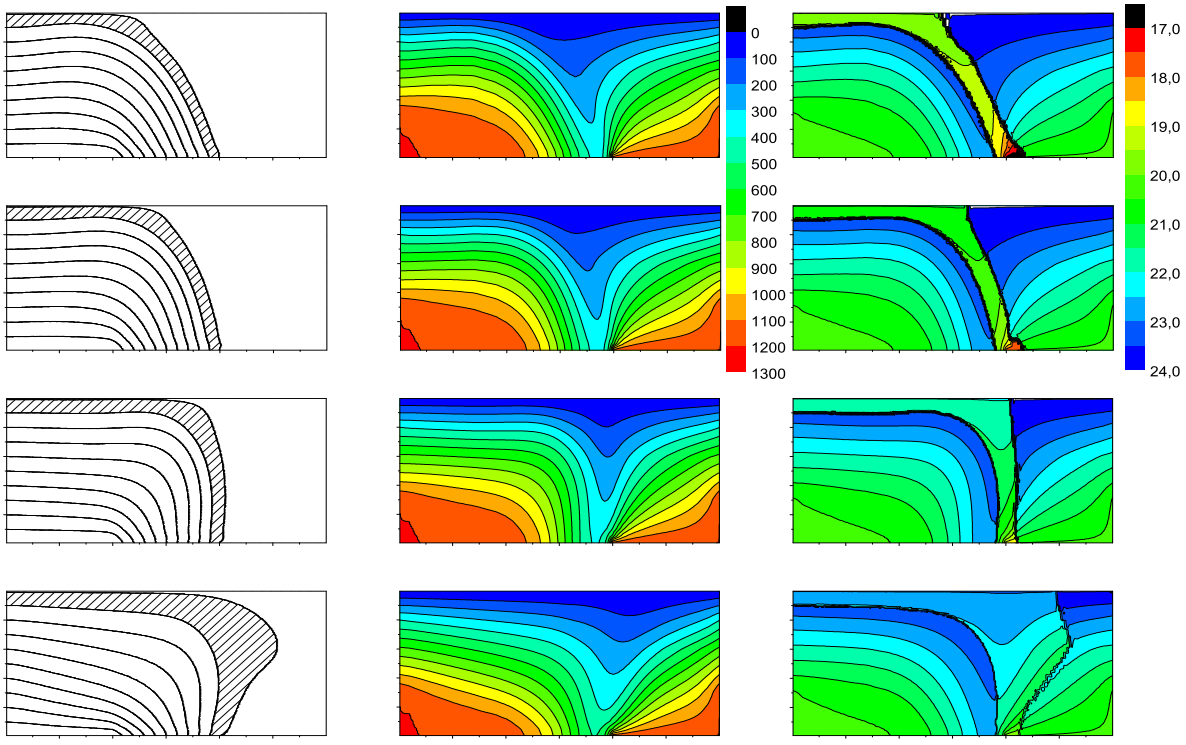

Figure 4.2: Stream lines (left), temperature (middle), and viscosity in log scale in the case of velocity $v_0 = 1$ cm/year. Reference viscosity η_0=10^{24} Pas and $K_t = 10^3$. The weakening parameter w changes from top to bottom: 10^{-4}, 10^{-3}, 10^{-2}, and 10^{-1}. The position of the weakening zone is hatched.

The obtained results show that in the given range of viscosities the dissipative heating may affect the temperature field, particularly, for faster subducting plates. For a very slow

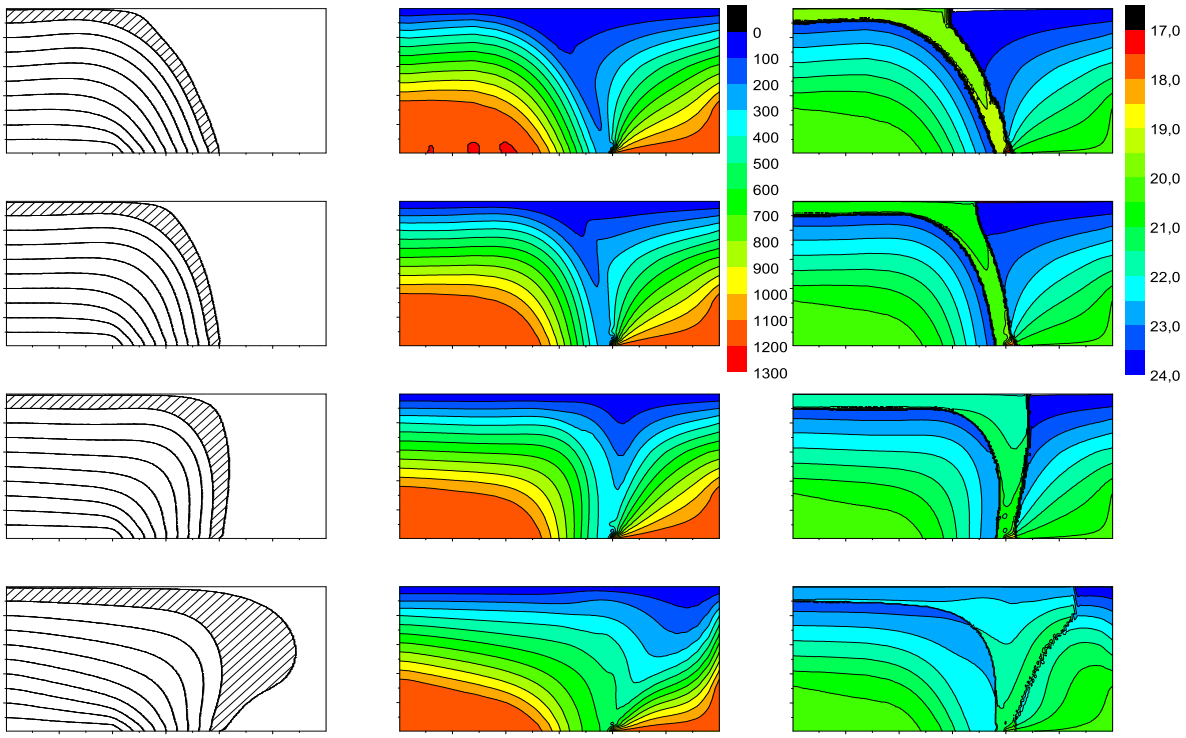

Figure 4.3: Same as in Figure 4.2 but the plate velocity $v_0 = 5$ cm/year.

plate with v_0=1 cm/year the minimum of surface heat flow moves along with the changing viscosity weakening parameter w as well as the dip angle (see Figure 4.5), however, the values in the minimum, about 20 mWm^{-2}, are the same for all cases. It means that in the case of slowly subducting plate the contribution of shear heating is negligible. Unlike that, in the case of a faster plate (5 cm/year) the value in the minimum increases from about 10 mWm^{-2} to 30 mWm^{-2} with the increasing weakening parameter w. In faster plates, cold geotherms should reach greater depths, which would result in smaller surface heat flow values. However, results show that dissipative heating may change this behaviour completely. This effect is noticeable namely in the case of a very fast plate v_0=10 cm/year, where the mantle wedge and the zone of weakness may be unrealistically overheated if the weakening w is not sufficient.

The results demonstrate that a weak uppermost part of the subducting plate may simply act as a lubricant. If the weakening is sufficient (at least two orders), the plate-like behaviour develops. Even if the model demonstrating this feature is too simplified to be realistic, and its results are rather suggestive than diagnostic, the magnitude of the viscosity weakening, which is required to obtain plate-like behaviour, corresponds roughly to the idea of how much water content in the oceanic crust reduces its viscosity.[2] Moreover, the model

[2]Realistic water content in the crust estimated from seismic tomography studies reduces the viscosity

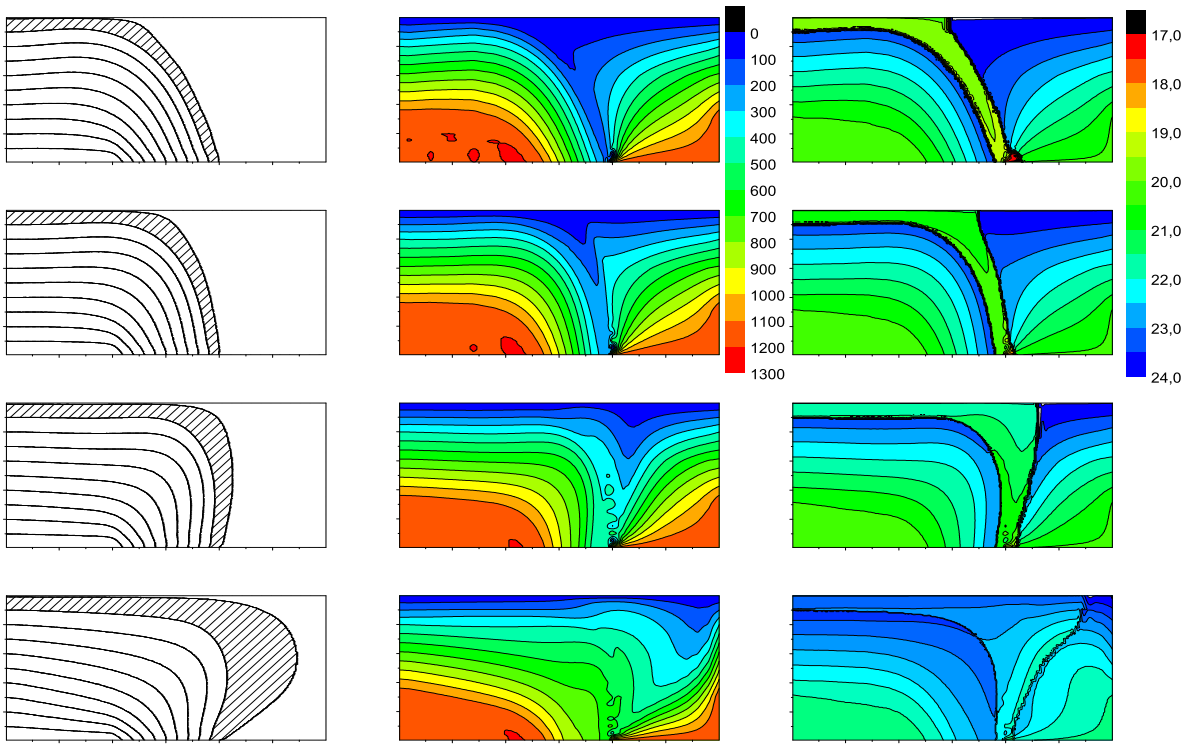

Figure 4.4: Same as in Figure 4.2 but the plate velocity $v_0 = 10$ cm/year.

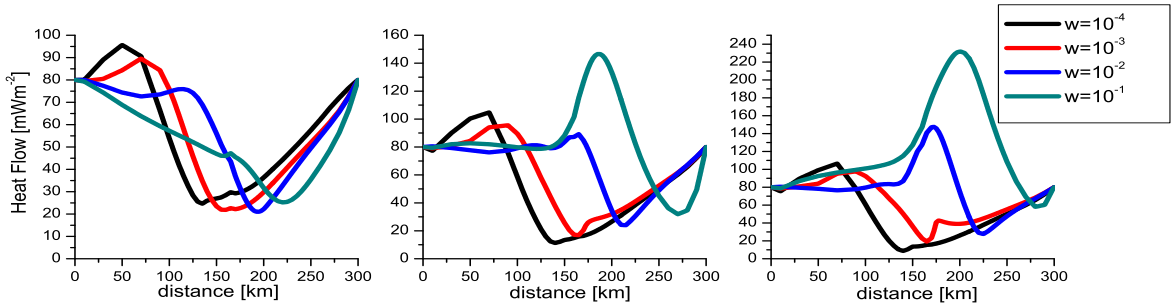

Figure 4.5: The surface heat flow for plate velocities 1 cm/year (left), 5 cm/year (middle), and 10 cm/year and different values of the viscosity weakening parameter w.

shows that the overriding lithosphere may become overheated if it has a high viscosity and the decoupling of lithospheric plates is inefficient (i. e. the viscosity weakening in the oceanic crust in small).

From these findings the conclusion is inevitable: the viscosity weakening in the topmost part of the subducting slab should be treated in the slab-wedge models in a more natural

of rocks by about two to four orders (Karato, 2003).

way than has been handled so far. Conder (2005) showed that different parameterizations of the fault decoupling the subducting plate from the overriding one may significantly affect the calculated temperature field, however, still considered the weakening in the topmost layer as an artificial trick how to separate the lithospheric plates from each other. The message from the model just described is clear: the contact between the subducting slab and the overlying lithosphere can be, and also should be, modelled self-consistently even in kinematic models. It removes some of the arbitrariness of kinematic models associated with a fault parameterization[3] and allows incorporating viscous deformations also in the subducting slab. The only problem with this approach is, how to achieve a plate-like pattern of the flow and reproduce realistic dip angles, but it has just been demonstrated that a weak layer at the top of the subducting slab is sufficient to produce such behaviour.

4.3 Pseudo-plastic Plates

Steady-state kinematic models used in literature seem to be inconsistent with the idea of eclogites exhumation since they require a stagnant tip of the mantle wedge (van Keken et al., 2002). The upward flow is not predicted in these steady-state models, however, the derived temperature field is used to claim that the tip of the wedge is extensively serpentinized (Hyndman and Peacock, 2003) because the calculated temperatures (less than 700°C at 2 GPa) are within the stability field of serpentinites (Ulmer and Trommsdorf, 1995). On the other hand, serpentitite is light and especially very weak and is therefore supposed to play a key role in the exhumation of eclogite-serpentinite melange (Guillot et al., 2001). A simple numerical model of an exhumation channel (Schwartz et al., 2001) predics exhumation rates of order cm per year due to low viscosity of serpentinites but the model does not take into account the temperature distribution in the exhumation channel.

In other words, the tip of the mantle wedge is supposed to be serpentinized since the presence of low viscosity serpentinites is required so as to explain the exhumation of heavy eclogites (Hermann et al., 2000), but the low temperatures allowing the existence of stable serpentinites are inferred from numerical models without any exhumation upward flow. If such exhumation occurs, one may expect that the backward flow will also substantially change the temperature field in the wedge[4] and that is why forecasting serpentinization from the temperature field calculated without the effect of a low serpentinite viscosity is at least questionable. In this section, the semi-kinematic wedge model is used to infer how weak serpentinite rocks in the tip of the wedge may affect the temperature field.

4.3.1 Model Description

The boundary conditions on velocity (4.1) – (4.3) applied to the model in the previous section do not take into account the interaction of the modelled portion of the wedge with its rest. That is why they need to be modified as depicted in Figure 4.6. The no-force

[3]For instance, shear heating rate which is in fact a free parameter (van Keken et al., 2002).

[4]It was shown by Gerya and Yuen (2003), who calculated how the "cold plume" may rise in the wedge.

condition is applied at the bottom and side boundary of the wedge; other conditions on velocity remain unchanged. Consequently, the zero heat flux condition is used on the whole bottom. In this way the material between the modelled shallow portion of the wedge and the rest of the lithosphere is allowed to flow freely.

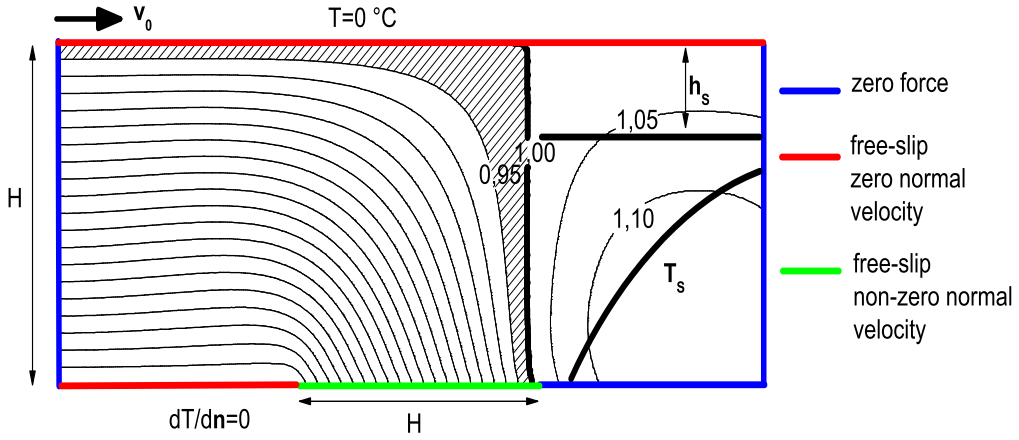

Figure 4.6: Rectangular domain 300 × 100 km with the boundary conditions. The stream lines for a constant viscosity are indicated as well as the thickness of the overlying plate h_s and the temperature T_s defining the weak portion of the mantle wedge.

In order to model the behaviour of the lithosphere in a more realistic way pseudo-plasticity is applied, which read the viscosity in the form

$$\eta_p = \frac{\sigma_{\text{yield}}(\psi,\, T,\, h)}{2\dot{e}}, \tag{4.7}$$

where σ_{yield} is the yield stress. The plastic behaviour is assumed only in a cold part of the lithosphere and hence is bounded by the temperature value T_c. The total viscosity is then

$$\eta = \begin{cases} \eta_c, & T > T_c \\ \frac{\eta_c \eta_p}{\eta_c + \eta_p}, & T < T_c \end{cases} \tag{4.8}$$

where η_c means the creep viscosity.

4.3.2 Characteristic Behaviour

The behaviour of the system with the pseudo-plastic viscosity defined by equations (4.7) – (4.8) and the creep viscosity η_c of the Arrhenius type (4.5) is studied in a domain of the same size as in the previous case (see Figure 4.6). Different magnitudes of the yield stress are prescribed in different regions; similarly to equation (4.5) the stream function is employed to identify distinct regions. Moreover, the yield stress is assumed to be a

function of the temperature and the depth:

$$\sigma_{\text{yield}}(\psi,\, T,\, h) = \begin{cases} \sigma_1, & \psi < 0.8\psi_B \quad \text{or} \quad \psi > \psi_B,\, h < h_c \\ \sigma_2, & \psi \in \langle 0.8\psi_B, 0.95\psi_B \rangle \\ \sigma_3, & \psi \in \langle 0.95\psi_B, \psi_B \rangle \\ \sigma_4, & \psi > \psi_B,\, T < T_s,\, h > h_c \\ \sigma_5, & \psi > \psi_B,\, T > T_s \end{cases} \tag{4.9}$$

The meaning of the above viscosity definition is following: In cold parts defined by the temperature T_c, the lithosphere behaves as a pseudo-plastic fluid, i.e. stress is limited by the yield stress value. The basic value of the yield stress is σ_1, but in the subducting plate another two zones are defined. The upper part of the plate defined by the stream function $0.8\psi_B < \psi < 0.95\psi_B$ represents the weak portion of the oceanic lithosphere with the yield stress σ_2 and the uppermost part of the plate given by $0.95\psi_B < \psi < \psi_B$ represents the oceanic crust with the yield stress σ_3. The yield stress of the overlying plate defined by the depth of the continental crust h_c is σ_1. Below the depth h_c the cold wedge is separated by the temperature T_s into two parts. The yield stress in the colder part is denoted as σ_4 and in the warmer part as σ_5. The part of the mantle wedge limited by the depth of continental crust h_c at the top and the temperature value T_s at the bottom represents the weakest, presumably serpentinized, portion of the wedge. Thus, the temperature value T_s represents the stability field of serpentinites whereas T_c represents the temperature below which plastic behaviour occurs and we consider $T_c > T_s$.

The same parameters for the creep viscosity as in the previous section are used and the limit of the plastic behaviour is set by the value $T_c = 800°\text{C}$. The extent of the weak portion of the wedge is limited by the depth of the overriding plate $h_c = 30$ km at the top and by the value $T_s = 700°\text{C}$ at the bottom. The result for yield stress values $\sigma_1 = 500$ MPa, $\sigma_2 = 100$ MPa, $\sigma_3 = \sigma_4 = 10$ MPa, and $\sigma_5 = 100$ MPa is shown in Figure 4.7. In this section, on both sides of the model the geotherm giving surface heat flow 80mWm^{-2} is used.

The described non-linear system with the viscosity defined by equations (4.5) – (4.9) exhibits behaviour which is typical for all subduction zones: in the shallow depths, the dip angle is small and it gradually increases with the increasing depth reaching a value about 60° and the depth of 100 km. More interestingly, there is a small-scale circulation in the cold and weak portion of the wedge extending to depths of about 80 km. The model demonstrates that the backward flow, which would explain rocks exhumation, may be a steady-state feature of the cold portion of the mantle wedge.

The system shows that there is a trade-off between the rheological weakening of the uppermost part of the subducting slab and the dip angle similar as in the previous purely viscous model. Figures 4.9 and 4.8 show the flow field, temperature field, viscosity distribution, and surface heat flow for various values of the yield stress of the oceanic crust (σ_3) in a wide range $0.1 - 200$ MPa, while the yield stress in other domains is fixed ($\sigma_1 = 500$ MPa, $\sigma_2 = 100$ MPa, $\sigma_4 = 1$ MPa, $\sigma_5 = 100$ MPa). A very weak oceanic crust effectively decouples the sinking plate from the overriding one and results in a small dip angle in shallow

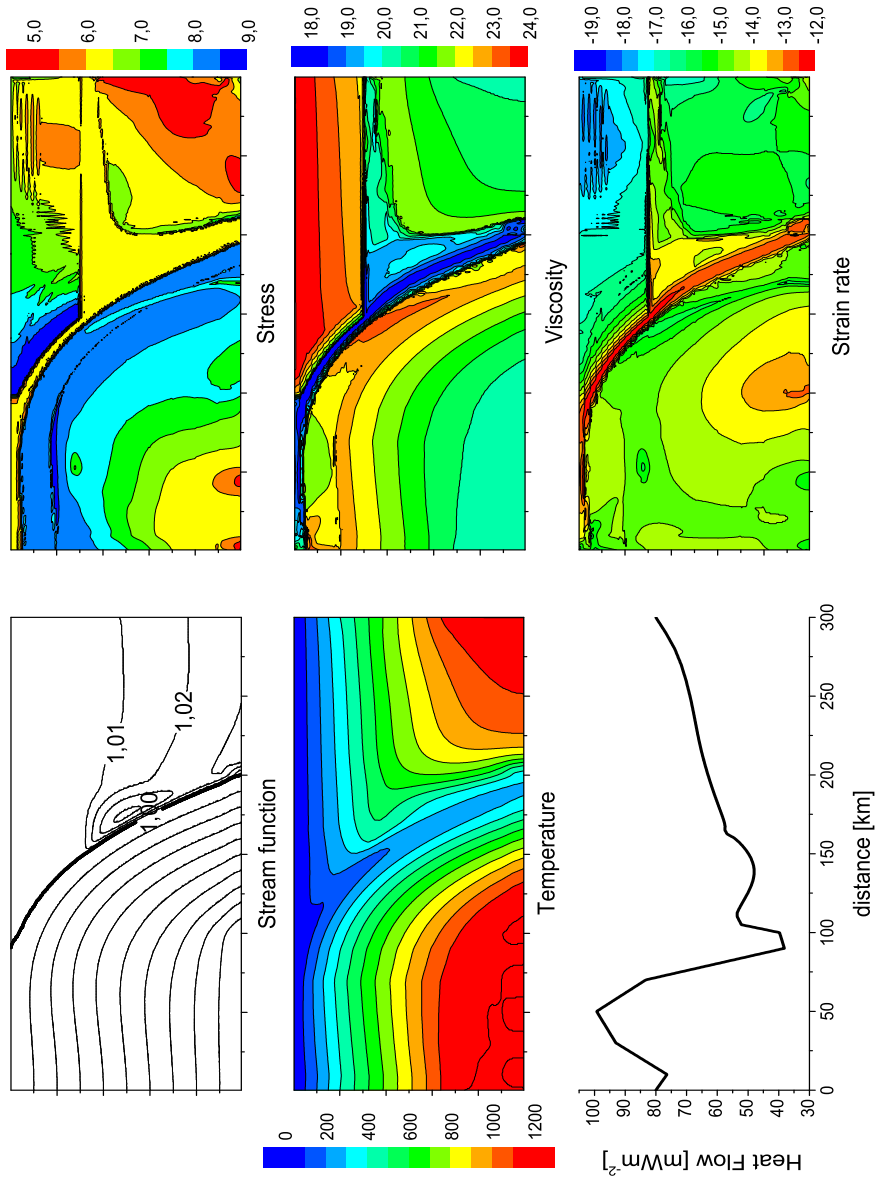

Figure 4.7: Characteristic pseudo-plastic behaviour demonstrates that in the cold nose of the mantle wedge, an exhumation flow may evolve if the weakening in the serpentinized portion is sufficient. The used values are: $\sigma_1 = 500$ MPa, $\sigma_2 = 100$ MPa, $\sigma_3 = \sigma_4 = 10$ MPa, $\sigma_5 = 100$ MPa and $h_s = 30$ km. Shown are the stream function, temperature, surface heat flow (all left), and stress, the viscosity, and the strain (all in the logarithmic scale). The plate velocity is 5 cm/year.

depths, while a very strong oceanic crust does not allow plates decoupling at all as shown in Figure 4.9.

Both end members ($\sigma_3 = 0.1$ MPa and $\sigma_3 = 200$ MPa) result in very low surface heat flow (< 20 mWm^{-2}) over a long distance (see Figure 4.8). In contrast to it, the oceanic crust of a yield stress more closer to that of the weak portion of the wedge, produces a narrow (~ 50 km) minimum of surface heat flow where the minimal values of heat flow are above 30 mWm^{-2}. It means that the backward flow occurring in the weak portion of the wedge causes not only a return of subducted rocks but also heat upwelling. The vigour of the backward flow obviously depends on the yield stress in the cold portion of the wedge. Figures 4.10 and 4.11 show the flow field, temperature field, viscosity distribution, and surface heat flow for various values of the yield stress in the cold part of the wedge (σ_4). The yield stress magnitudes in other domains are again set to $\sigma_1 = 500$ MPa, $\sigma_2 = 100$ MPa, $\sigma_3 = 1$ MPa, and $\sigma_5 = 100$ MPa, which is sufficient to produce a small dip angle (about 30°) in shallow depths. If the yield stress in the wedge is smaller or roughly equal to that in the subducting crust, the return flow occurs in the wedge. If it is too high, the wedge is stagnant and the region of very low surface heat flow is wider.

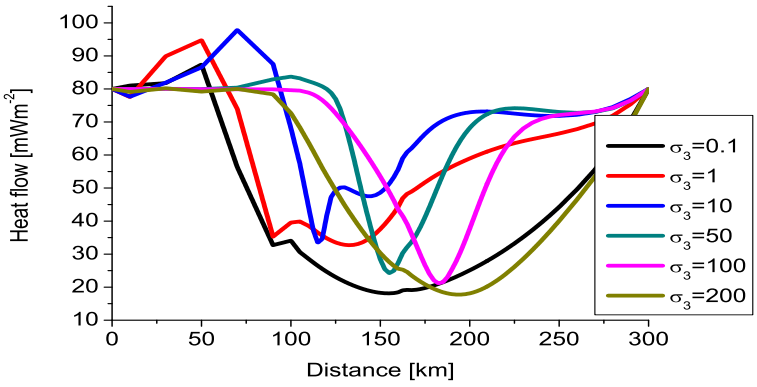

Figure 4.8: The surface heat flow for various values of the yield stress in the oceanic crust.

In Figures 4.12 and 4.13, the upper limit of the weak portion is not given by the crustal depth h_c, but is also limited by the temperature denoted as T_h. It is demonstrated that the upper limit of the exhumation flow may be related to the temperature at which serpentinization starts, i.e. $100 - 400$°C (Wenner and Taylor, 1971).

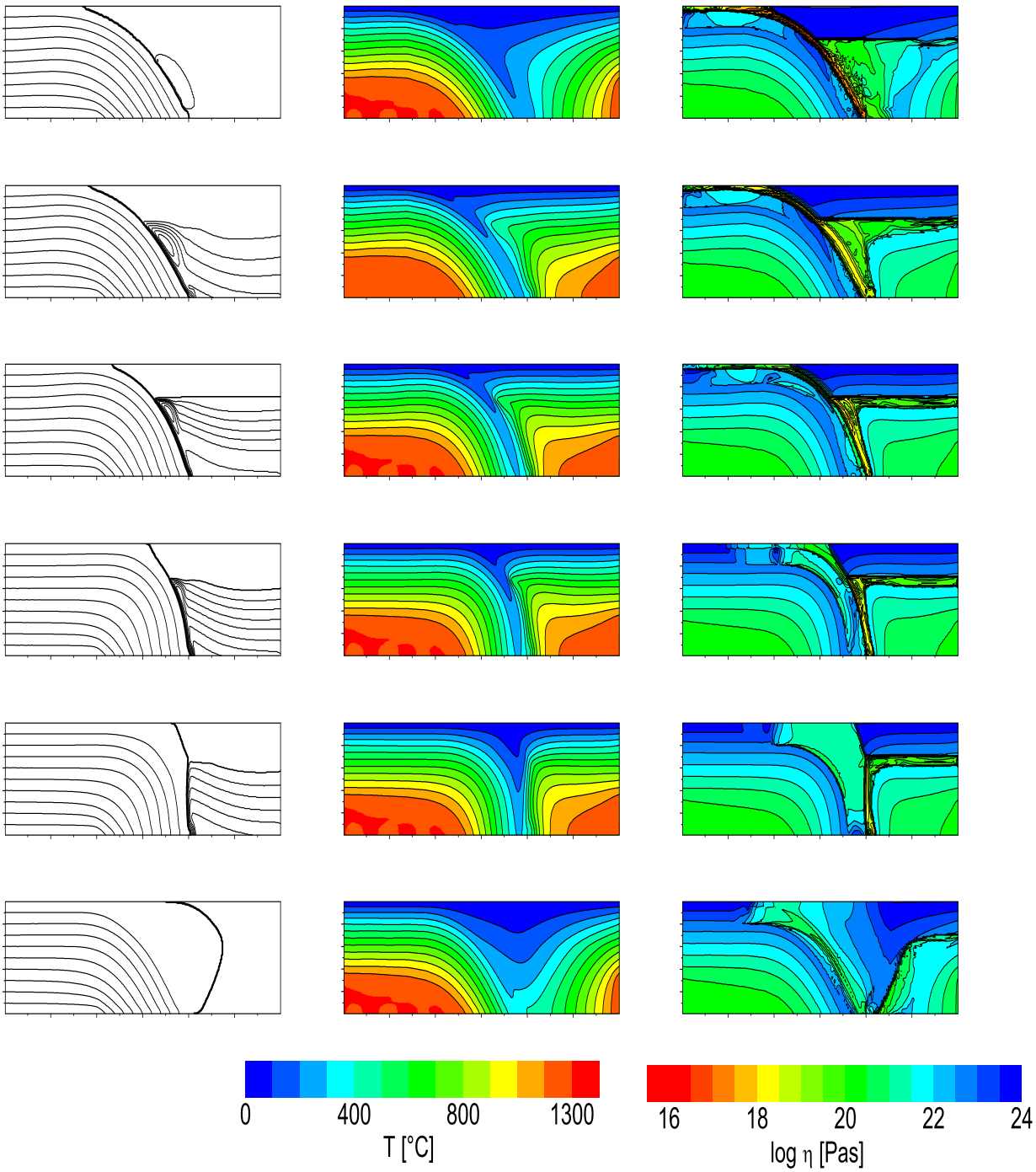

Figure 4.9: Stream function, temperature, and viscosity for different yield stress magnitude in the oceanic crust. The used values σ_3 are 0.1 MPa (top), 1 MPa, 10 MPa, 50 MPa, 100 MPa, and 200 MPa (bottom). The yield stress magnitudes in other parts are the same as in the text.

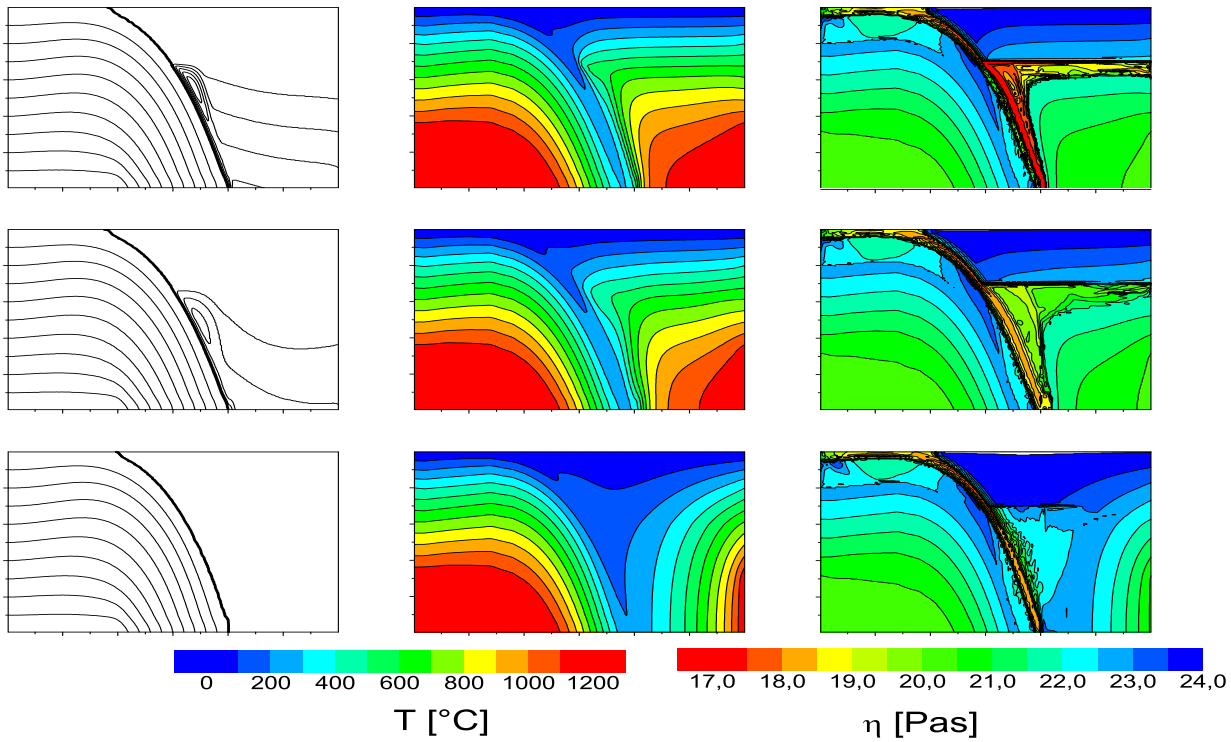

Figure 4.10: Stream function, temperature, and viscosity for different yield stress magnitude in the cold portion of the mantle wedge. The used values of σ_4 are 0.1 MPa (top), 1 MPa, and 10 MPa (bottom). The yield stress magnitudes in other parts are the same as in the text.

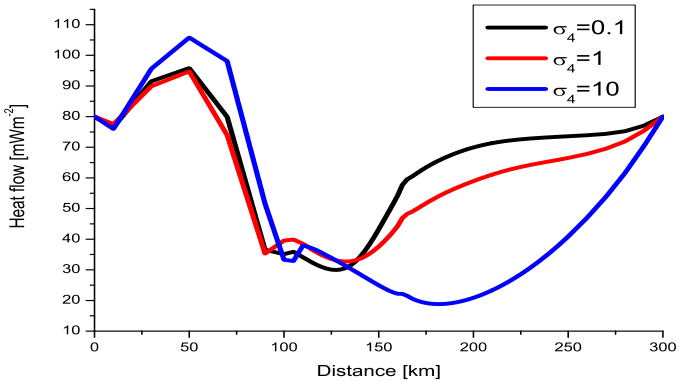

Figure 4.11: The surface heat flow for various values of the yield stress in the cold portion of the mantle wedge.

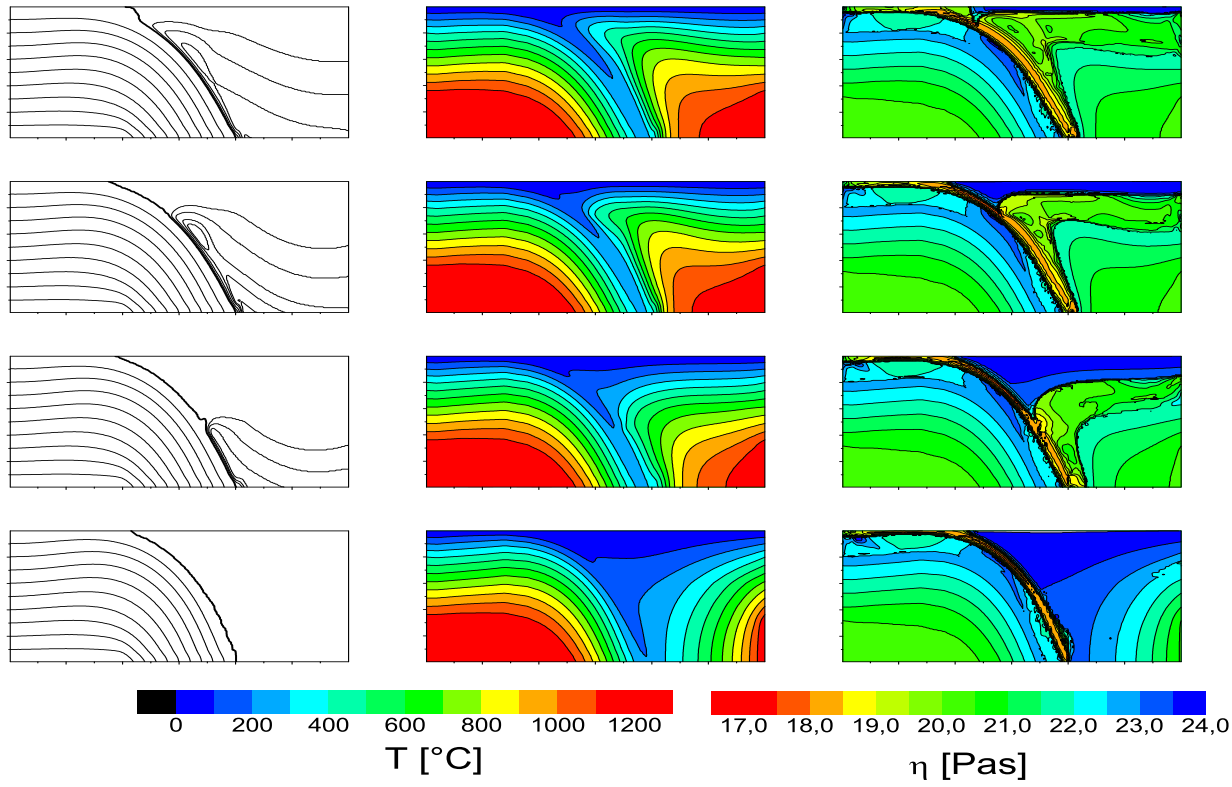

Figure 4.12: Stream function, temperature, and viscosity in case the upper part of the weakening zone in the mantle wedge is limited by temperature T_h. The used values are 100°C (top), 200°C, 300°C, and 400°C.

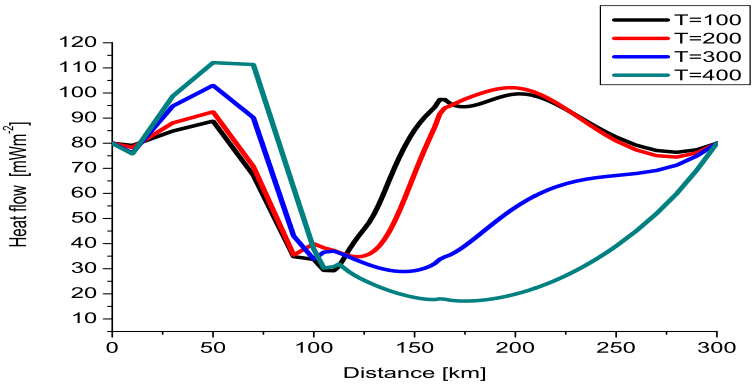

Figure 4.13: The surface heat flow for various values of T_h limiting the upper boundary of the weak part of the mantle wedge.

4.3.3 Realistic Viscosity

In this section, both diffusion and dislocation creep are employed instead of the viscosity (4.5). In the equation

$$\eta = \left(\frac{d^m}{AC_{OH}^r}\right) \dot{e}^{\frac{1-n}{n}} \exp \frac{E+pV}{nRT}, \tag{4.10}$$

values for diffusion creep $n = 1$, $E = 335$ kJ, $V = 4 \times 10^{-6}$ m^3/mol and dislocation creep $n = 3.5$, $E = 480$ kJ, $V = 11 \times 10^{-6}$ m^3/mol (Hirth and Kohlstedt, 2003) are used and the yield stress is given in a simpler form

$$\sigma_{\text{yield}}(\psi,\, T,\, h) = \begin{cases} \sigma_1, & \psi < (1-\delta)\psi_B \text{ or } \psi > \psi_B,\, h < h_s \\ \sigma_2, & \psi \in \langle (1-\delta)\psi_B, \psi_B \rangle \\ \sigma_3, & \psi > \psi_B,\, T < T_s,\, h > h_s \\ \sigma_4, & \psi > \psi_B,\, T > T_s \end{cases} \tag{4.11}$$

The total viscosity is then

$$\frac{1}{\eta_{\text{eff}}} = \frac{1}{\eta_{\text{yield}}} + \frac{1}{\eta_{\text{diff}}} + \frac{1}{\eta_{\text{disl}}}. \tag{4.12}$$

The absolute value of viscosity depends on the water content and the grain size, whose values are not known precisely. Here these values are set so as the viscosity at the depth 100 km is 10^{20} Pas for both diffusion and dislocation creep at the strain rate 10^{-15} s^{-1}. The temperature T_s is set to 700°C, which is the limit of serpentinite rocks stability (Ulmer and Trommsdorf, 1995).

Figure 4.14 shows the temperature field, stream lines, and surface heat flow for different magnitudes of the yield stress in the oceanic crust σ_2, whereas in all other parts the yield stress is $\sigma_1 = \sigma_3 = \sigma_4 = 10^9$ Pa. Similarly as in the previous results, a plate-like behaviour develops only if there is a substantial drop in the strength of the oceanic crust comparing to the strength of the overlying mantle. Lower ratio between yield stress in the oceanic crust and in the overlying lithosphere results in less steep dip angle. Results show that the wedge is very cold as surface heat flow above the wedge is as low as 15 mWm^{-2}. This is caused by negligible viscous coupling between the subducting plate and the overlying mantle which leads to a stagnant mantle wedge dominantly cooled by the incoming lithosphere.

The flow in the tip of the wedge changes drastically if a weakening (drop in the yield stress) in the wedge is considered. Figure 4.15 demonstrates that various yield stress magnitudes may produce different backward flow. In this simulation, the yield stress in the subducting crust is set so as a reasonable dip angle is achieved, and the influence of the yield stress magnitude in the wedge is studied. The vigour of the backward flow in biggest if the yield stress in the subducting crust is somewhat higher than in the wedge.

Figures 4.16 and 4.17 present in detail the case when $\sigma_2 = \sigma_3 = 10$ MPa. The retrograde P-T path shows nearly isothermal exhumation from depths of about 70 km similar to that one described by Herms (2004).

4.3.4 Concluding Remarks

The presented model shows that the viscosity weakening (modelled by lowering in the yield stress) in the topmost part of the subducting plate significantly affects the dip angle and, moreover, a similar weakening in the cold part of the wedge may cause a backward flow. Such a flow would explain the exhumation of rocks from depths of about 80 km to lover crustal depths or even to shallower depths. In these zones of low viscosity, the physical reason for lowering the viscosity (yield stress) is likely the high water content resulting in extensive serpentinization. An important result from the presented models is that the exhumation occurs due to low viscosity of serpentinite and not due to its low density.

In models of the exhumation channel (e.g. Schwartz et al., 2001), both the low viscosity and density is needed. Since the density of serpentinites is very low (2.7 gcm^{-3}) and the density of eclogites very high (3.5 gcm^{-3}), their melange is supposed to have usually lower density (3.1 gcm^{-3}) than the surrounding peridotites (3.3 gcm^{-3}). However, if the serpentinization is only partial, the density of the melange may be close to that of peridotites and buoyancy force will not allow the exhumation in the channel model. Unlike that, in our model partial serpentinization is not a problem, since mere partial serpentinization results in sufficient strength reduction (Escartin et al., 2001).

In the serpentinized cold tip of the wedge, the characteristic value of strain stress is about two orders of magnitude higher (see Figure 4.16) than in the rest of the wedge. Together with the assumed high content of water it is an indicator that this region of exhumation exhibits LPO different from the rest of the wedge since B-fabric olivine may occur there (Lassak et al., 2006; Kneller et al., 2007).

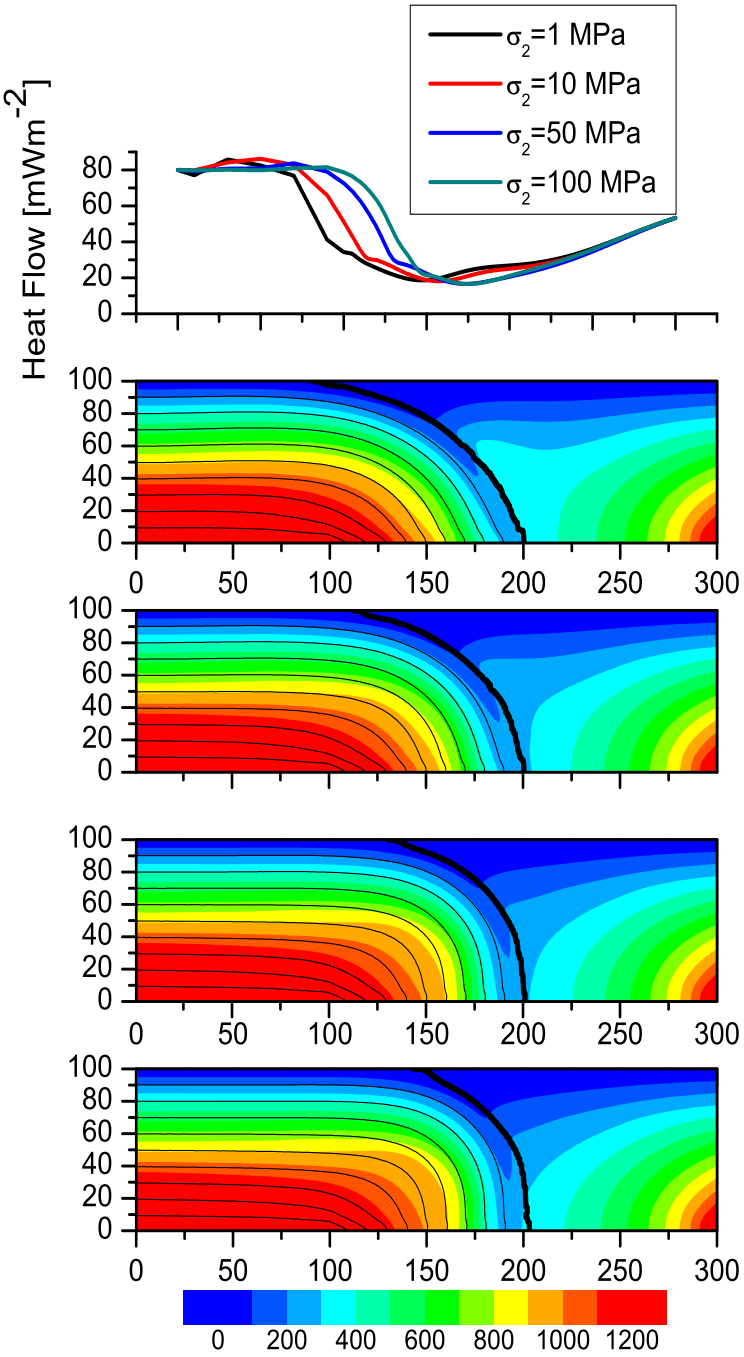

Figure 4.14: The temperature, the stream function (contour interval 0.1 ψ_B), and the surface heat flow for a subducting plate of rate 5 cm/year. Results calculated for different magnitudes of the yield stress in the oceanic crust without any weakening in the mantle wedge.

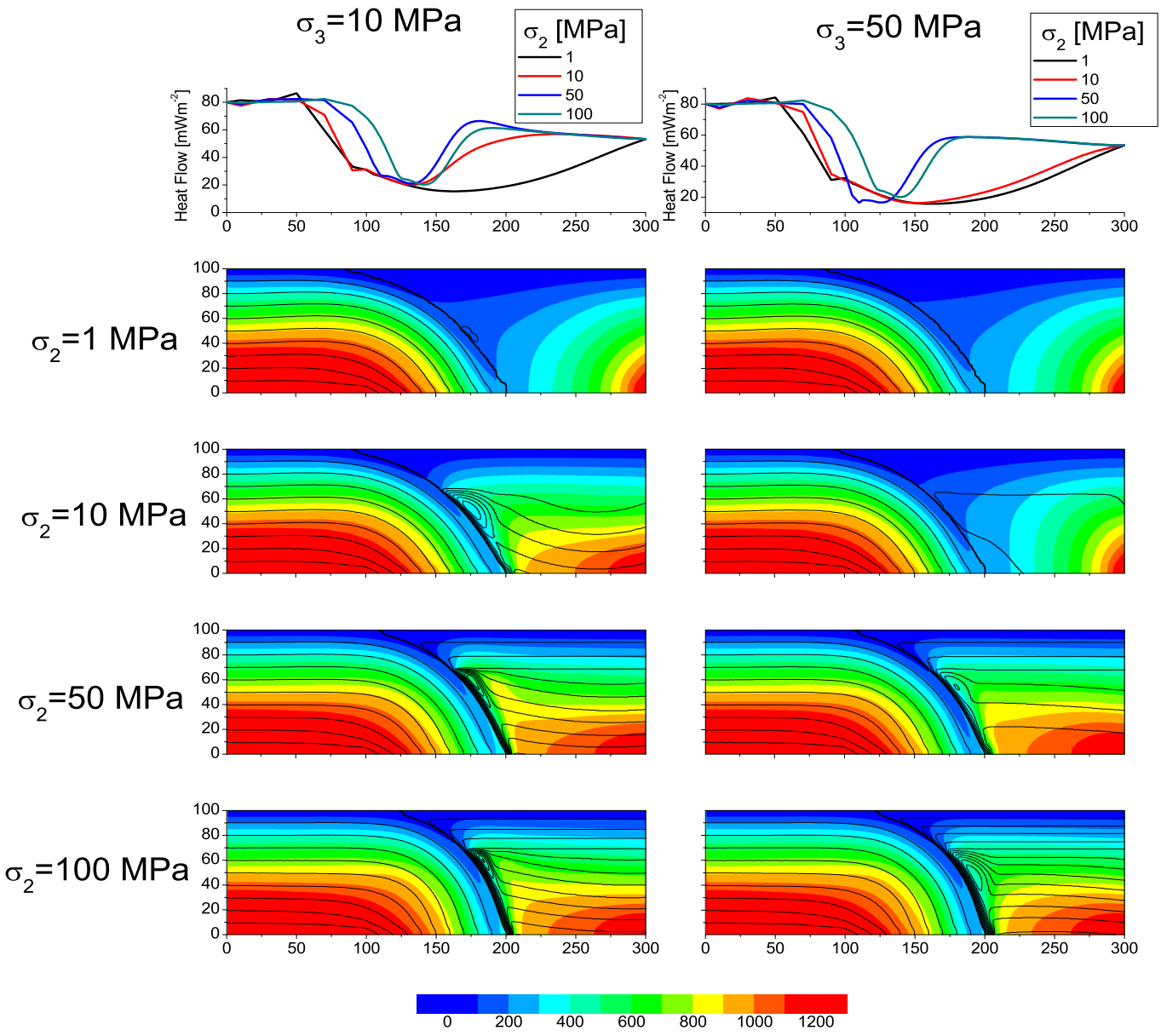

Figure 4.15: The temperature, the stream function (contour interval 0.1 ψ_B for $\psi < \psi_B$ and $0.005\psi_B$ otherwise), and the surface heat flow for a subducting plate of rate 5 cm/year. Results for two different magnitudes of the yield stress in the cold tip of the wedge (columns) and different magnitudes of the yield stress in the oceanic crust (rows) shown.

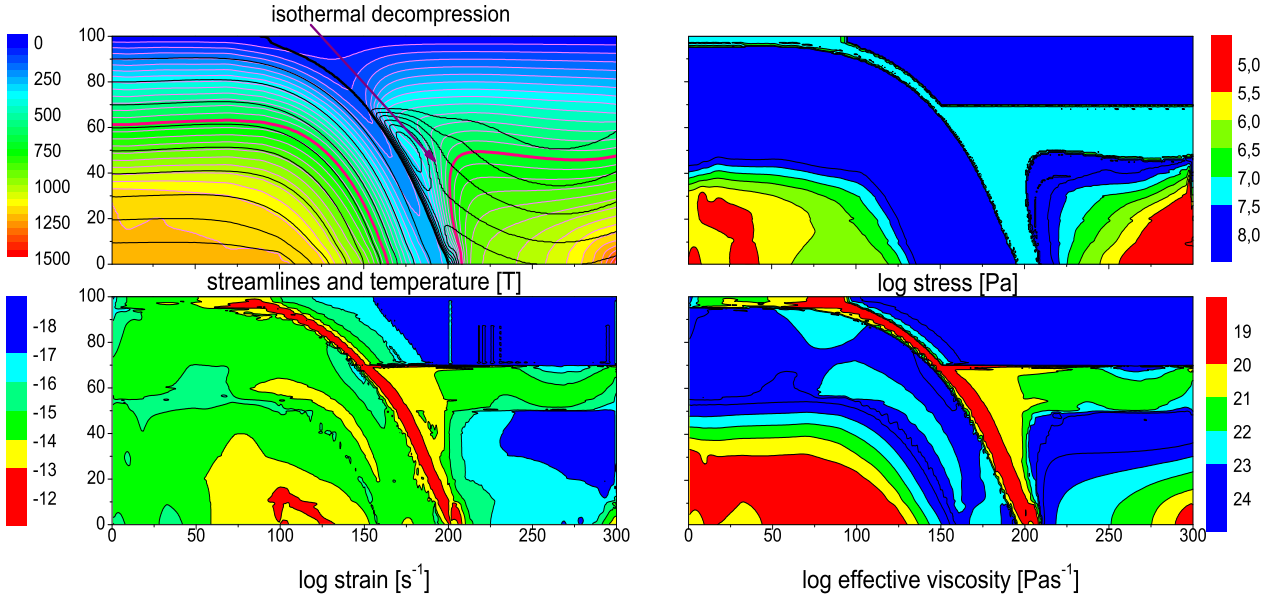

Figure 4.16: The temperature and stream lines (top left), stress (top right), strain (bottom left), and effective viscosity in the case of $\sigma_2 = \sigma_3 = 10$ MPa (convergence rate 5 cm).

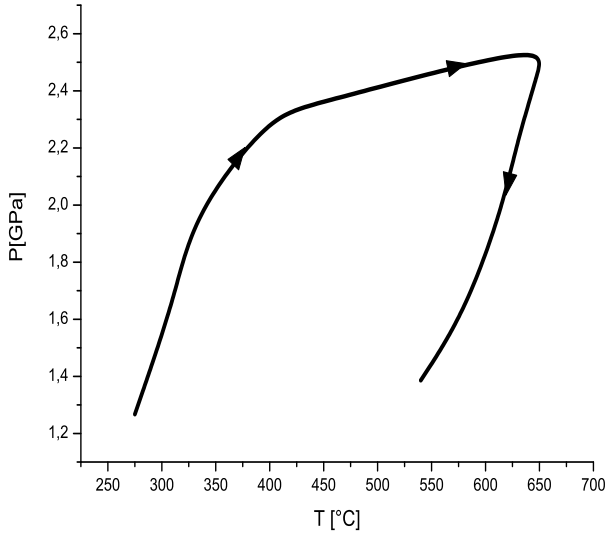

Figure 4.17: P-T path demonstrating the exhumation in the case of $\sigma_2 = \sigma_3 = 10$ MPa; convergence rate 5 cm. Retrograde path shows almost isothermal decompression.

4.4 Heat Flow in Backarcs

As discussed before in Section 2.2.3, an important quantity, which constraints numerical models of the mantle wedge, is surface heat flow, whose pattern is similar in almost all subduction zones regardless their age, dip angle or convergence rate (Currie and Hyndman, 2006) and whose explanation is missing, particularly, in those backarcs, where no recent extension is observed (Hyndman et al., 2005). Although the typical heat flow values in forearcs are usually fitted in steady-state models of the wedge (e.g. van Keken et al., 2002; Manea et al., 2005), the elevation of surface heat flow in backarc has been mostly ignored. It has been suggested that the likely explanation is an induced flow in the wedge (Andrews and Sleep, 1974), but the recent kinematic model of Currie et al. (2004b) failed to reproduce high heat flow values in backarcs. Also a dynamic model did not explain the increase in a large portion of the wedge[5] and the increase in surface heat flow has not been successfully modelled yet.

In this section, the method, in which the position of the contact between the subducting slab and the overlying wedge is not prescribed a priori, is employed also in the backarc model. The aim of this section is to find a rheology which is capable to reproduce the observed surface heat flow pattern in backarcs under various temperature boundary conditions. This is important since the increase in surface heat flow in backarcs is reported from nearly all subduction zones, but one may assume that temperature conditions at the base of backarc may differ from case to case. Therefore, a rheology successful in reproducing the observed heat flow pattern for a wide range of boundary conditions could be a good candidate for the actual rheology. Rheology of backarcs may be affected by a number of parameters: besides temperature and pressure, it depends also on mineral composition, water content or grain size. The fact that the slab-wedge interface is a part of the solution in the presented approach makes the problem non-linear even in the case when different constant viscosity values are prescribed in the slab and in the wedge. To make the problem more tractable, only the influence of temperature- and pressure-dependence of viscosity to the state of the mantle wedge is taken into account.

4.4.1 Model Description

We have formulated a 2-D model of the flow in the mantle wedge, which enables to calculate simultaneously the velocity field, the temperature distribution, and particularly the boundary between the slab and the wedge. The steady state flow is described by the Stokes equation

$$-\nabla p + \nabla \cdot (\eta(\nabla \boldsymbol{v} + (\nabla \boldsymbol{v})^T)) = 0 \tag{4.13}$$

and the continuity equation

$$\nabla \cdot \boldsymbol{v} = 0. \tag{4.14}$$

[5]Eberle et al. (2002) studied a dynamic model with prescribed plate velocities and came to the conclusion that an increase in backarc heat flow (in a fraction approximatelly 200 km in width) occures if the overriding plate was fixed. If a more realistic free-slip condition is applied at the top of the overriding plate, no elevation of heat flow is produced.

In the Stokes equation the body forces are not taken into account as we are focused on the flow in the mantle wedge driven solely by a subduction traction. The temperature distribution is given by the steady state heat transfer equation

$$\rho c_p \boldsymbol{v} \cdot \nabla T = \nabla \cdot (k \nabla T) + \boldsymbol{D} : \nabla \boldsymbol{v} + \rho \alpha T \boldsymbol{v} \cdot \boldsymbol{g} \ , \tag{4.15}$$

which includes not only dissipation of heat but also adiabatic heating/cooling. Radiogenic heating in the crust is not taken into account since we are focused purely to the effect of heat carried from the depth by convection in the wedge. Radiogenic heat sources localized in the continental crust are not the cause of hot backarcs and their contribution to surface heat flow is additive. Moreover, the dissipative terms are neglected in the continental crust, which is assumed to be a stagnant lid modelled as a high viscosity layer.

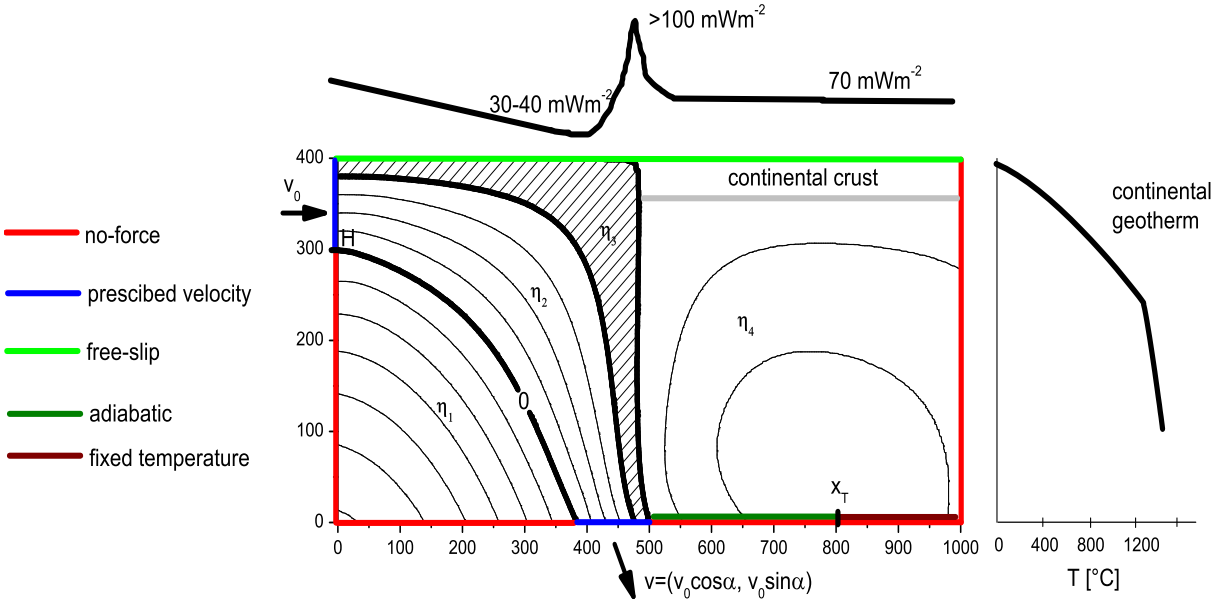

Figure 4.18: Scheme of the computational rectangle domain 1000×400 km with boundary conditions on velocity showing streamlines in the case of constant viscosity in the whole domain. The value of the stream function is scaled by the value $\psi_s = Hv_0$. Streamlines labelled as 0 and 1 thus border the subducting plate. The weakening zone given by $\delta_w = 0.2$ is hatched and domains with different viscosity prefactors defined by eq. (4.20) are indicated. Typical surface heat flow (based on Hyndman et al. (2005)) is schematically shown together with the cold continental geotherm prescribed at the landward boundary up to the depth of 300 km. The transition point x_T at the base of the backarc, where the thermal boundary condition changes from adiabatic gradient to prescribed temperature, is marked.

The above mentioned set of equations is solved in a rectangular domain 1000×400 km. The boundary conditions for velocities, which are the only source of the flow in our model, are as follows: the impermeable boundary with the free-slip

$$\boldsymbol{v} \cdot \boldsymbol{n} = 0, \tag{4.16}$$

$$\boldsymbol{D}\cdot\boldsymbol{n}-(\boldsymbol{n}\cdot\boldsymbol{D}\cdot\boldsymbol{n})\boldsymbol{n}=0, \tag{4.17}$$

is prescribed on the top boundary and the no-force condition

$$\boldsymbol{D}\cdot\boldsymbol{n}=0 \tag{4.18}$$

at the rest of the boundary except the parts, where an inflow or an outflow is given; for details see Figure 4.18.

The lithospheric inflow is modelled by means of a prescribed velocity v_0 at the topmost part of the left boundary. The depth interval of the inflow is denoted by H. The lithospheric outflow is modelled as a part of the bottom boundary, at which both horizontal and vertical velocities are prescribed. The end point of the outflow of the slab is located in the middle of the bottom boundary and the outflow width is $H/\sin\delta$, where δ means the given dip angle. The prescribed velocities are $v_x = v_0\cos\delta$ and $v_y = v_0\sin\delta$ and thus the mass flow through the outflow boundary is equal to the mass flow through the inflow boundary.

At the side parts of the rectangular domain the geotherms are prescribed: the oceanic geotherm on the left and the continental geotherm on the right up to a depth of 300 km, below which the zero heat flux through the boundary is assumed. The temperature at the top boundary is set to 0°C, while at the bottom of the computational domain a variable boundary condition is used: an adiabatic temperature gradient 0.3°C/km is prescribed from $x = 0$ to a certain distance x_T, which is considered to be a free parameter. In the rest of the boundary temperature is fixed to 1450°C, which is the typical temperature in the depth of 400 km (Ito and Katsura, 1989). This is the crucial point of this model – the exact boundary condition is not known and it is supposed to be different for various subduction zones. For steeply subducting slabs the point x_T is presumably close to the prescribed outflow since the area underlayed by the slab is relatively narrow. For shallower slabs the point x_T should be farther, however, an important source of uncertainties comes from the slab behaviour, which may be affected by the phase transition at 670 km; flattening of the subducting slabs at 670 km discontinuity was both observed by seismic tomography (van der Hilst, 1995) and calculated in numerical models (Christensen, 1997). If a large part of the backarc was underlayed with the cold slab, the point x_T might be relatively far from the prescribed outflow. Although the actual thermal boundary condition at the bottom of the backarc may differ from case to case, elevated surface heat flow is observed throughout backarcs, so it should be insensitive to prescribed thermal conditions.

As in the previous sections, a viscosity formally dependent on the stream function is used. The uniqueness of the stream function is achieved differently by defining $\psi = \psi_H = v_0 H$ at the left upper point of the rectangular domain. Then the subducting slab is bordered by the streamline $\psi = 0$ on the bottom and $\psi = \psi_H$ on the top. The viscosity is defined by

$$\eta = \eta_R(x, y, \psi)\exp\left(-\ln(K_T)\frac{T}{\Delta T}+\ln(K_p)\frac{p}{\Delta p}\right), \tag{4.19}$$

where η_R is the reference viscosity prefactor. The considered temperature- and pressure-dependence of viscosity is thus a simplified version of (2.9), which is broadly employed in convection studies to distinguish between both dependences in a more straightforward

way (e.g. Christensen, 1989; Čadek and Berg, 1998; Trubitsyn et al., 1999; Yoshioka and Murakami, 2007). The different parts of the model are defined by

$$\eta_R = \begin{cases} \eta_1, & \psi < 0 \\ \eta_2, & \psi \in \langle 0, (1-\delta_w)\psi_H \rangle, 0 < \delta_w < 1 \\ \eta_3, & \psi \in \langle (1-\delta_w)\psi_H, \psi_H \rangle \\ \eta_4(y), & \psi > \psi_H. \end{cases} \tag{4.20}$$

In this way four distinct parts may be separated as shown in Figure 4.18: the mantle below the oceanic lithosphere with the viscosity prefactor η_1, the subducting slab except its top with the viscosity prefactor η_2, the topmost part of the slab with the viscosity prefactor η_3, and the mantle wedge and the overlying plate with the viscosity prefactor η_4. The prefactors $\eta_1 - \eta_3$ are constant and η_4 is a simple function of depth: the lithosphere overlying the subducted slab is divided into the continental crust (its prefactor is denoted as η_{4C}) and the wedge (η_{4W}) by specifying a crustal depth. The top of the subducting plate is treated separately as we suppose it is significantly weaker than the rest of the subducting plate. The ratio between the thickness of the weakening zone at the inflow part of the boundary and the thickness of the whole subducting lithospheric plate is denoted by δ_w.

4.4.2 Results

We set the parameters so as to model a generic subduction zone: in the first set of simulations, the slab thickness H is 100 km and the bottom dip angle δ is set to 60°, which is the average deep dip angle over all subduction zones (Jarrad, 1986). We used the slab velocity v_0 equal to 4.5 cm/year. Other parameters were set as described in Table 4.1.

On the left boundary the oceanic geotherm giving the surface heat flow 80 mWm^{-2} was prescribed, whereas on the right boundary the cold continental geotherm producing the surface heat flow 40 mWm^{-2} was applied up to the depth of 300 km. Below this depth zero heat flux through the boundary was assumed.

First, we investigated the case where individual domains have a constant viscosity (i.e. $K_T = K_p = 1$) in order to gain an insight into the physics of the problem. It turned out that the value of viscosity η_1 does not affect the flow in the wedge. Similarly as in the previous forearc models, the viscosity η_3 in the uppermost part of the subducting slab is very important for the flow in the overlying lithosphere. If it is sufficiently lower than the viscosity of the continental crust, about three orders of magnitude, a relatively narrow zone (of the weak viscosity material) is formed at the top of the subducting slab. The weak oceanic crust acts as a lubricant and effectively reduces viscous forces transferred from the subducting slab to the overriding lithosphere. If, however, the viscosity in the wedge below the continental crust (η_{4W}) is reduced, lubrication between the subducting slab and the wedge becomes inefficient and a substantial flow occurs in the wedge. It is demonstrated in Figure 4.19, where the adiabatic temperature gradient is applied at the whole bottom boundary. The viscosity of the wedge changes in a range $10^{16} - 10^{22}$ Pas: For high viscosity values the wedge is nearly stagnant and heat is transferred dominantly

by conduction, which results in relatively high temperatures at the bottom but low surface heat flow. For low viscosity values η_{4W} a substantial corner flow occurs and convection dominates – heat from the bottom is transferred to the surface and surface heat flow increases, but a cold material neighbouring the subducting slab cools down a relatively large part of the bottom. A balance between these two heat transfer mechanisms appears when the viscosity values of the uppermost part of the subducting plate and the wedge are roughly equal. Then a significant part of the wedge is hot (temperatures above 1200°C near the continental crust) and simultaneously a pattern of elevated surface heat flow may be observed.

In the case of pure temperature-dependence of viscosity (i.e. $K_T > 1$ and $K_p = 1$), the corner flow becomes more localized to the region near the subducting plate. Stronger temperature-dependence results in stronger localization and it substantially affects the temperature field. It is documented in Figure 4.20, where the parameter scaling temperature dependence K_T varies between 1 and 10^3. Since the adiabatic temperature gradient is again applied at the whole bottom, the narrower corner flow does not carry enough heat from the bottom and the whole wedge is cooled down with increasing flow localization. The temperature field in the wedge is, however, very sensitive to the thermal boundary condition applied at the bottom; moving the point x_T, from where a temperature value 1450°C is fixed, towards the subducting plate results in an increase of wedge temperatures and surface heat flow as well, which is shown in Figure 4.21. Due to the flow localization effect and the strong sensitivity to the bottom boundary condition, the purely temperature-dependent viscosity is not able to successfully reproduce the observed pattern of the surface heat flow.

If also the pressure-dependence of viscosity is employed, the temperature field in the wedge may change drastically. Figure 4.22 shows the case with $K_T = 10^3$ and $K_p = 10^2$ under variable thermal boundary conditions applied at the bottom. Even if a pattern of elevation in surface heat flow is developed only for a transition point close to the sinking slab ($x_T = 700$, 800 km), a trend is obvious: the corner flow can carry more hot material from greater depths and distances.

Figure 4.23 shows simulations when even stronger temperature- and pressure-dependence $K_T = 10^5$ and $K_p = 10^4$ is used under various thermal boundary conditions. In this case, an increase in surface heat flow is obtained even in the case of the adiabatic temperature gradient applied at the whole bottom boundary. The strong pressure dependence of the viscosity leads to a low viscosity layer beneath the continental crust, which allows rapid corner flow (velocities of the same order as the convergence rate). Such a rapid flow can carry upward the materials, which are far from the subducting slab and therefore not cooled down, and, consequently, almost uniformly hot region below the backarc is developed. A surface manifestation of such hot regions, elevated surface heat flow, occurs.

The question arises, whether the elevated backarc surface heat flow obtained for strongly temperature- and pressure-dependent viscosity is robust enough, i.e. whether it is not sensitive to reasonable changes of other parameters of the model. We have found that such a pattern is stable over a broad range of tested bottom dip angles ($30° - 80°$, see Figure 4.25), different convergence rates ($4 - 10$ cm/year) and different oceanic geotherms

(yielding $50 - 100$ mWm^{-2} at the surface, see Figure 4.25). On the other hand, if a pressure-dependence is not considered, the corner flow is focused to the region close to the subducting slab, which is extensively cooled down with the cold incoming lithosphere, and thus such a viscosity does not produce hot backarcs.

4.4.3 Concluding Remarks

The developed method of simultaneous calculation of both the velocity and the temperature fields and the subducting slab shapes was used to calculate surface heat flow in backarc regions. The model does not require usual assumptions about the position of the whole slab-wedge boundary (e.g. van Keken et al., 2002; Currie et al., 2004b) and thus it is advantageous to use it to study the interactions between the subducting slab and the wedge where an induced flow occurs. We investigated how different kinds of viscosity affect the mantle wedge flow and, particularly, the surface heat flow pattern, which is directly observable quantity. Observed surface heat flow in almost all backarcs is remarkably higher than that in the continental lithosphere (Currie and Hyndman, 2006) and that is why we searched for a viscosity law, which would be capable to reproduce this effect under various thermal conditions at the base of the backarc. Numerical modelling revealed that the increase in surface heat flow may be reproduced even with a constant viscosity in the wedge if its value is sufficiently low. More realistic, temperature-dependent, viscosity, however, does not reproduce such a pattern and the results are extremely sensitive to the thermal conditions applied at the bottom. Strong temperature dependence leads to a localization of the corner flow to a region close to the subducting slab and such a localized flow is unable to advect enough heat from the depth. On the other hand, considered pressure-dependence may compensate this effect since it results in a low viscosity layer below the backarc continental crust. If the viscosity of this layer is sufficiently low (about 10^{17} Pas), the pattern of surface heat flow increase is stable under various thermal boundary conditions and various settings of the subducting slab including convergence rate or dip angle. Note that the radiogenic heating has been omitted in the calculations; if it were added into the continental crust, it would result in an additional increase of surface heat flow in the wedge. There is still a space for such an increase as the modelled heat flow in backarcs is still slightly lower than the observed values. The calculated heat flow outputs may thus be considered as the heat flow part of deep origin.

In general, our preferred viscosity distribution is in agreement with the idea of a low viscosity wedge (Billen and Gurnis, 2001) although the magnitude of viscosity decrease seems to be rather high. It is possible that such a viscosity weakening could be also caused by compositional effects and/or water content; a very low viscosity zone in shallow portion of the backarcs could be the physical reason why the backarcs are relatively hot anyway.

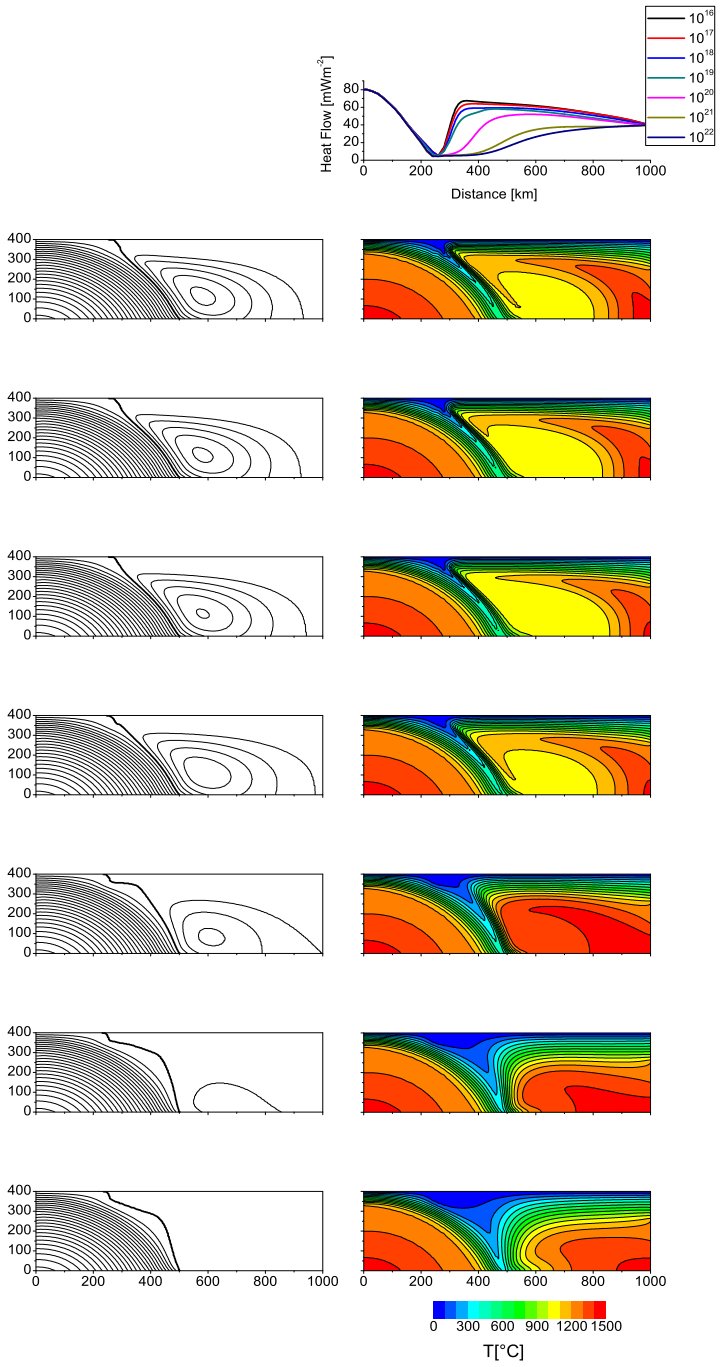

Figure 4.19: The comparison of the flow patterns, temperature fields, and surface heat flow for different values of the constant mantle wedge viscosity η_{4W} changing from 10^{16} (top) to 10^{22} Pas (bottom). Other viscosity values $(\eta_1, \eta_2, \eta_{4C})$ are set to 10^{23} Pas except the weaker topmost layer in the subducting lithosphere (η_3) which is set to 10^{20} Pas. The stream function is scaled by the value ψ_H; the contour interval is $\psi_H/10$. The adiabatic temperature gradient is considered along the whole bottom boundary.

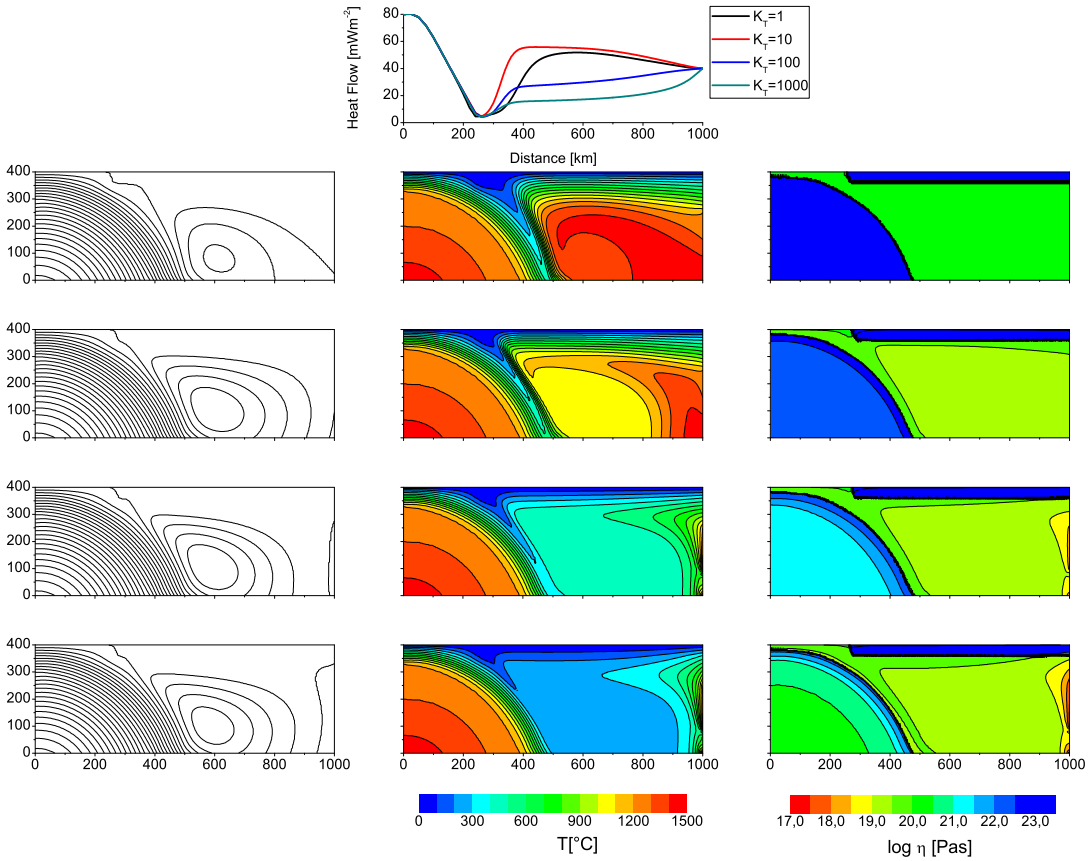

Figure 4.20: The comparison of the flow and temperature fields and surface heat flow for a purely temperature dependent viscosity ($K_p = 1$) with K_T changing from 1 (top) through 10 and 100 to 10^3 (bottom) in the case $\eta_{4W} = 10^{20}$ Pas. Other viscosity values and representation of the stream function is the same as in Figure 4.19.

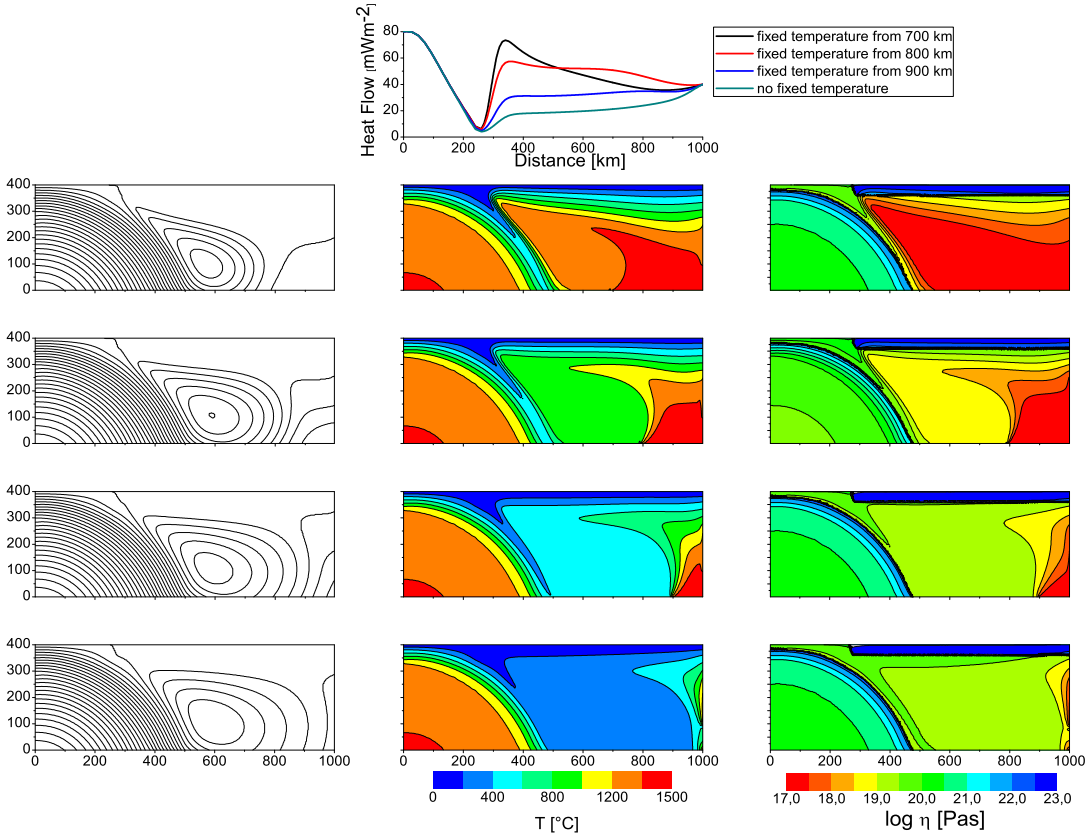

Figure 4.21: The different flow patterns, the temperature distributions, and surface heat flow in the case of temperature dependent viscosity $K_T = 10^3$ ($K_p = 1$) for different thermal boundary conditions at the bottom: The fixed temperature 1450°C is applied at the bottom boundary from the point x_T equal to 700 km (top), 800 km, 900 km, and 1000 km (bottom). Representation of the stream function and values η_1, η_2, η_3, η_{4C}, and η_{4W} are the same as in Figure 4.19.

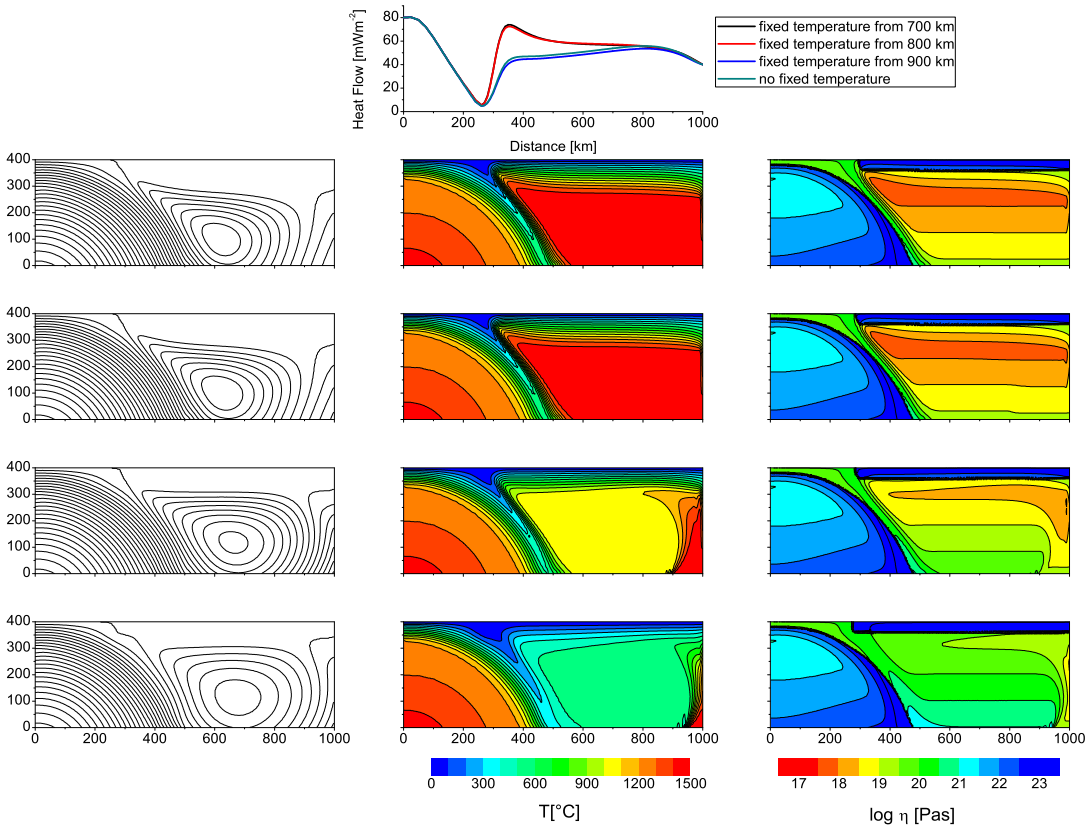

Figure 4.22: The same as Figure 4.21, but the pressure-dependence $K_p = 10^2$ was used.

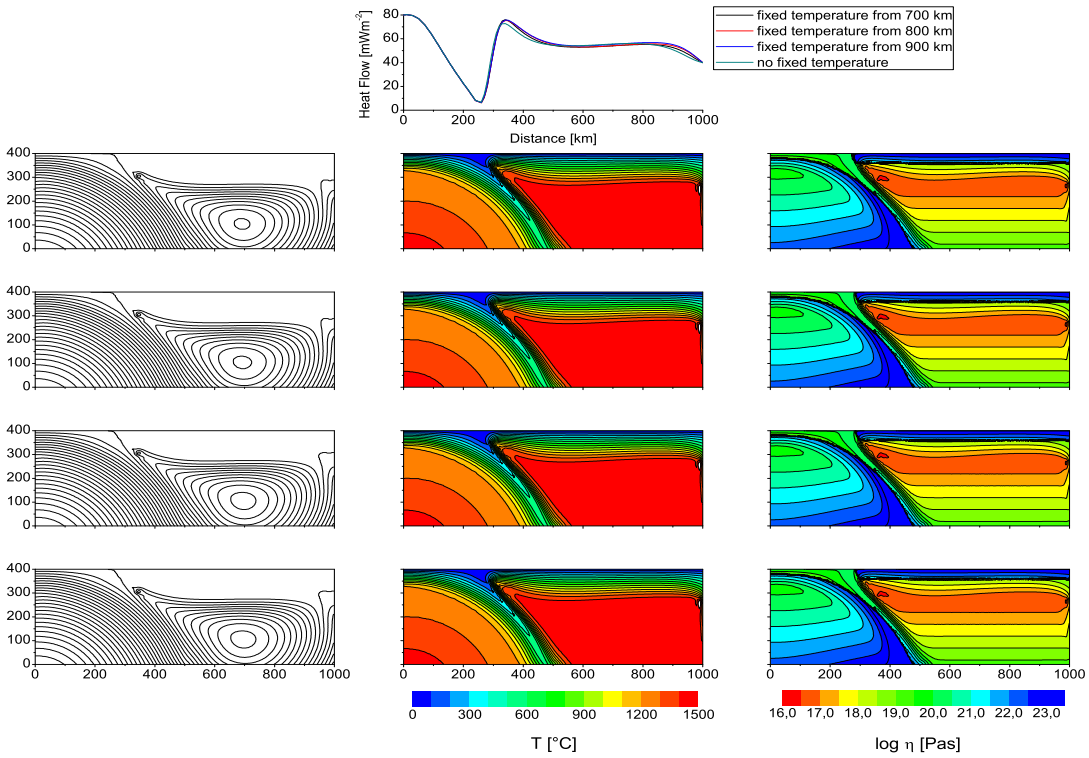

Figure 4.23: The same as Figure 4.21, but stronger temperature- and pressure-dependence $K_T = 10^5$ and $K_p = 10^4$ was used.

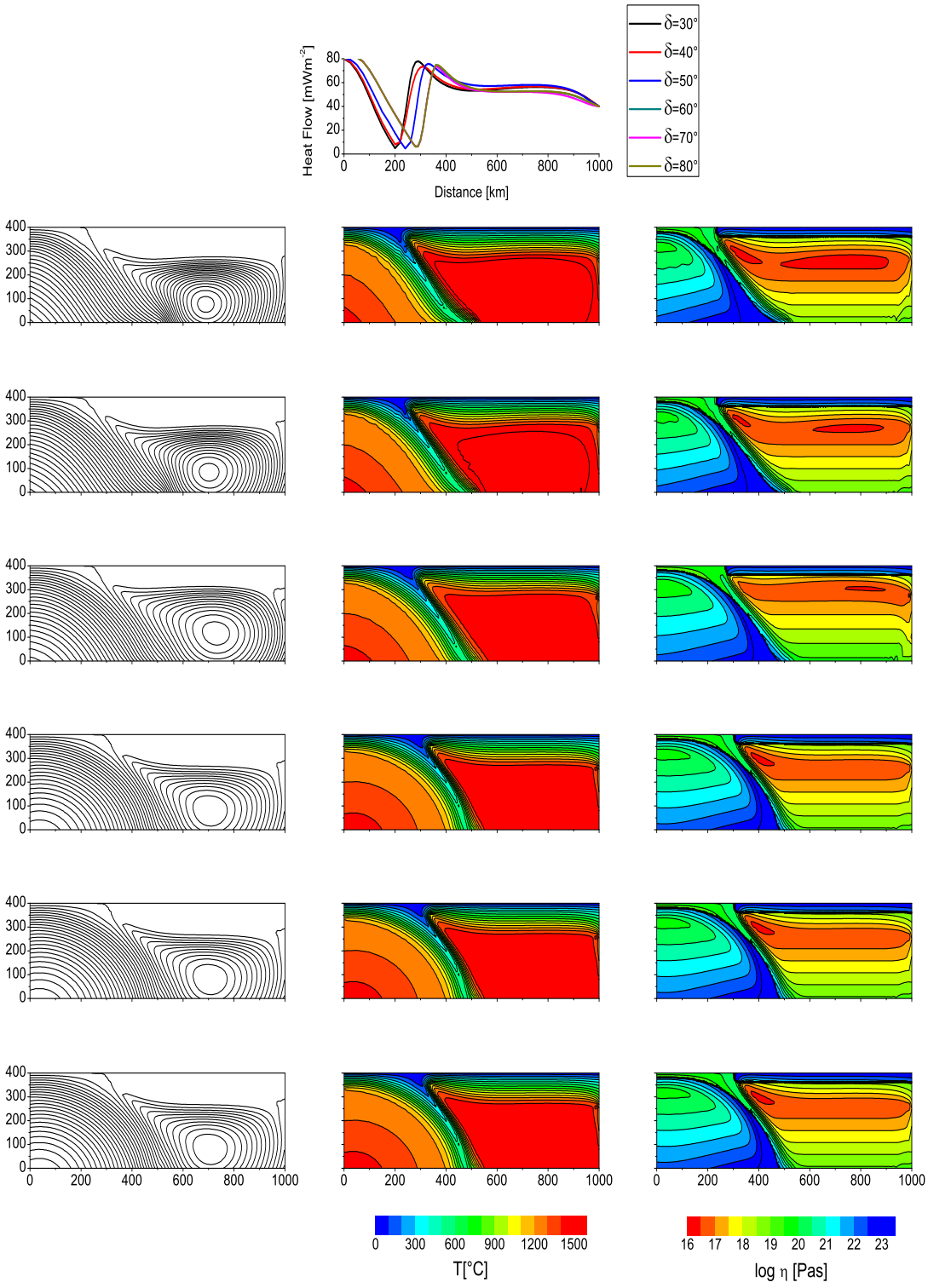

Figure 4.24: Temperature- and pressure-dependent viscosity ($K_T = 10^5$, $K_p = 10^4$) with the adiabatic temperature gradient applied at the bottom for different dip angles δ changing from 30° to 80°.

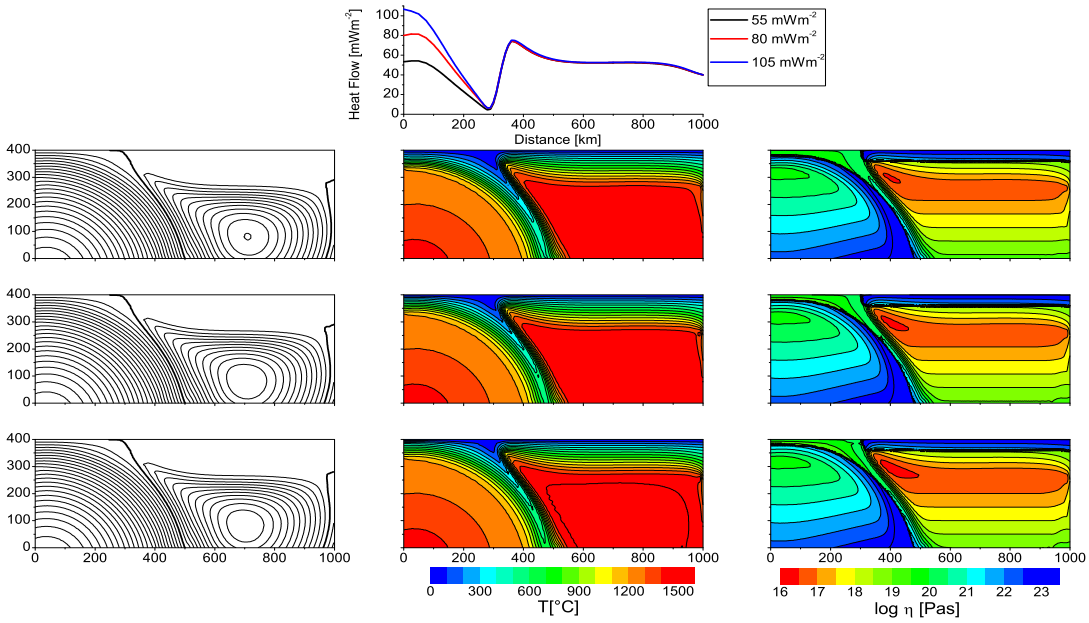

Figure 4.25: Temperature- and pressure-dependent viscosity ($K_T = 10^5$, $K_p = 10^4$) with the adiabatic temperature gradient applied for different oceanic geotherms giving the surface heat flow value in the range of $50 - 100$ mWm^{-2}.

4.5 Flow in Mantle Wedge

It has been shown that the thermal convection does not produce asymmetric downwelling even if weakening mechanisms are employed (Tackley, 2000b) and therefore, King (2001) emphasized the existence of subduction zones, asymmetric downwelling currents, as a major feature of the thermal convection in the Earth's mantle. The presented steady-state models demonstrated that a weak layer at the top of the subducting plate is the reason of this asymmetry. Quite recently it has also been demonstrated by Gerya et al. (2008) in an evolutionary model.

Since different subduction zones exhibit various dip angles, a considerable effort has been striven to identify the physical reasons for this phenomenon. Different studies have shown there is a lack of statistical correlation between observed dip angles and other measured quantities such as convergence rate or age of subducting plates (Jarrad, 1986; Cruciani et al., 2005). This study has demonstrated that the primarily cause of different dip angles is the viscosity weakening in the subducted oceanic crust (presumably caused by high water content), which is in a good agreement with the most recent results of dynamic models, which found that slab dip in the upper mantle depends primarily on slab strength and plate boundary coupling (Billen and Hirth, 2007; Manea and Gurnis, 2007). It thus explains why traditionally sought relations among the dip angle and other various parameters (including convergence rate and age) exhibit so poor correlations. From our results we may conclude that the slab dip is related to zones of weakening and therefore it might be correlated with zones of low seismic velocity and high attenuation. Results from Sections 4.2 and 4.3 show that the reduction in strength is likely the primary control of the subduction dip angle.

The presented results show a possibility that likely there are two induced eddies in the mantle wedge as depicted in Figure 4.26. The first one, localized in the weak serpentinized forearc, reaches depths of about 80 km and causes the exhumation of the eclogites and serpentinites from these depths to lover crustal levels. This forearc wedge flow is enabled by the presence of substantially weak serpentinites. The presented results show that the exhumation does not depend critically on the density of exhumed rocks and that buoyancy does not have to be the primarily cause of the exhumation as it has been thought so far (Ernst et al., 1997; Schwartz et al., 2001). Although serpentinites are less dense than peridotites, the inclusion of heavy eclogites may result in an increase in the average density of exhumed rocks so as it may be close to that of peridotites. In such a case buoyancy would not be a sufficient mechanism for exhumation but the presented models show that density contrasts are not necessary. The second eddy, which is induced in the mantle wedge, is the flow localized in the backarc and its most visible manifestation is the increase in surface heat flow observed in most backarcs (Hyndman et al., 2005). The presented models are able to reproduce a similar pattern of increase in surface heat flow if the viscosity beneath the continental crust is low. Since the stress and presumably also water content is high and temperatures are low in the tip of the wedge, where the exhumation occurs, it is likely that B-fabric olivine crystals are present there (Lassak et al., 2006). The transition from the trench-parallel (close to trench) to subduction parallel fast directions observed in several

subduction zones (Long and van der Hilst, 2005) thus may be another manifestation of the backward exhumation flow which is relatively strictly separated from the large-scale flow in the rest of the wedge induced by subduction traction.

It would be of interest to run a simulation in order to calculate both the circulation in the forearc and in the backarc in one model, however, it would require much denser mesh and consequently require considerably large CPU time.

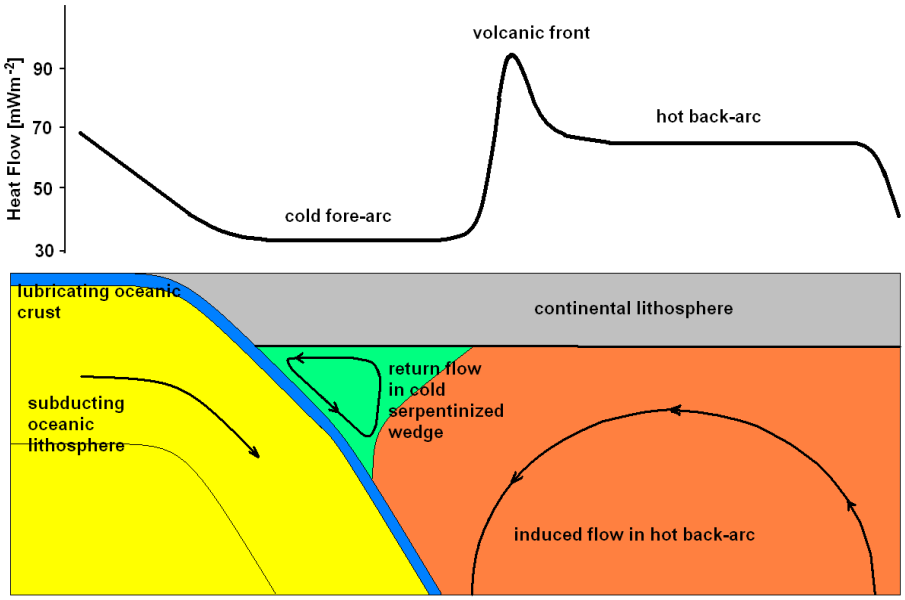

Figure 4.26: Schematic picture of possible flow in the mantle wedge shows the corner flow induced in the serpentinized forearc and the large-scale flow in backarc, which considerably affects surface heat flow.

Chapter 5

Conclusions

The main goal of this work was to develop a numerical model of a subducting lithospheric plate which would include a contact between the subducting plate and the overriding one without need for a geometric description of this contact. The self-consistent generation of subduction zones is one of the most important questions of plate tectonics (King, 2001), however, it has been mostly ignored in mantle wedge models. We have shown a way how the contact can be incorporated into the steady-state wedge models although its position is not set in advance. Consequently, the described principle has been implemented in a numerical model of the mantle wedge and it has been demonstrated that a weak oceanic crust acts as a lubricant and the viscosity weakening magnitude primarily controls the shape of the subducting slab in shallow depths.

The developed numerical model has been used to model two different effects connected with subduction zones. In the model of a generic forearc, a serpentinized tip of the wedge has been modelled as a low viscosity zone. This model demonstrated that exhumation of rocks may occur in the wedge if serpentinite rocks are weak enough. Moreover, the model showed that nearly isothermal exhumation may uplift the rocks from depths of about 80 km to a lower crustal level at temperatures close to 700°C, which is consistent with some observations (Herms, 2004).

The presented model has also been employed to model the flow in backarc regions. Since almost all backarcs exhibit an increase in surface heat flow (Hyndman et al., 2005), a rheology, which reproduces this feature under a wide range of possible thermal conditions, has been sought. This topic is currently widely discussed because numerical models used so far have not successfully modelled this feature (Currie et al., 2004b; Currie and Hyndman, 2006). It has been found that a purely temperature-dependent rheology is not able to reproduce the observed pattern in surface heat flow, however, a temperature- and pressure-dependent viscosity is able to fit the increase in surface heat flow if the pressure-dependency is strong enough. In such a case, an almost uniformly hot backarc is formed under a wide range of slab properties including various dip angles and convergence rates. The overall idea of the flow in the mantle wedge has been discussed in Section 4.5 and schematically summarized in Figure 4.26.

The presented work has shown that a self-consistent inclusion of the plate-wedge bound-

ary is possible in steady-state models and, moreover, it is a must-have feature of subduction models. In a simple steady-state model it has been demonstrated that inclusion of this contact may results in effects so far unforeseen by "classical" numerical models.

Acknowledgements

Here I would like to thank everyone who helped me during the long period of my doctoral study. First of all, I must express my thanks to my supervisor Ctirad Matyska for his valuable comments, constructive criticism, and huge patience. I also thank all the staff, particularly the "geodynamics group", of the Geophysical Department at MFF UK for the friendly atmosphere. Last, but certainly not least, I thank to my girlfriend Lenka for her help and encouragement, which kept me on the right track.

References

Andrews, D. J., Sleep, N. H., 1974. Numerical Modelling of Tectonic Flow behind Island Arcs. *Geophys. J. Int.*, 38: 237–251.

Abers, G. A., van Keken, P. E., Kneller, A. E., Ferris, A., Stachnik, J. C., 2006. The thermal structure of subduction zones constrained by seismic imaging: Implications for slab dehydration and wedge flow. *Earth. Planet. Sci. Lett.*, 241: 387–397.

Aki, K., Richards, P., 1980. Quantitative Seismology. W. H. Freeman and Company, San Francisco.

Baldwin, S. L., Monteleone, B. D., Webb, L. E., Fitzgerald, P. G., Grove, M., Hill, E. J., 2004. Pliocene eclogite exhumation at plate tectonic rates in eastern Papua New Guinea. *Nature*, 431: 263–267.

Barazangi, M., Isacks, B. L., 1971. Lateral variations of seismic-wave attenuation in the upper mantle above the inclined earthquake zone of the Tonga Island Arc: deep anomaly in the upper mantle. *J. Geophys. Res.*, 76: 8493–8515.

Baranzagi, M., Isacks, B., Oliver, J., Dubois, J., Pascal, G., 1973. Descent of lithosphere below New Hebrides, Tonga-Fiji and New Zealand. *Nature*, 242: 98–101.

Barazangi, M., Isacks, B. L., 1979. Subduction of the Nazca plate beneath Peru: evidence from spatial distribution of earthquakes. *Geophys. J. Int.*, 57: 537–555.

Batchelor, G. K., 1967. An Introduction to Fluid Dynamics, Cambridge University Press, Cambridge.

Bevis, M., Taylor, F. W., Schutz, B. E., Recy, J., Isacks, B. L., Helu, S., Singh, R., Kendrick, E., Stowell, J., Taylor, B., Calmans, S., 1995. Geodetic observations of very rapid convergence and back-arc extension at the Tonga arc. *Nature*, 374: 249–251.

Benioff, H., 1954. Orogenesis and deep crustal structure: additional evidence from seismicity. *Geol. Soc. Amer. Bull.*, 65: 385–400.

Bercovici, D., 2003: The generation of plate tectonics from mantle convection. *Earth. Planet. Sci. Lett.*, 205: 107–121.

Bijwaard, H., Spakman, W., Engdahn, E. R., 1998. Closing the gap between regional and global travel time tomography. *J. Geophys. Res.*, 103: 30055–30078.

Billen, M. I., Gurnis, M., 2001. A low viscosity wedge in subduction zones. *Earth. Planet. Sci. Lett.*, 193: 227–236.

Billen, M. I., Gurnis, M., 2001. Comparison of dynamic flow models for the Central Aleutian and Tonga-Kermadec subduction zones. *Geophysics, Geochemistry, Geosystems*, 4: 2001GC000295.

Billen, M. I., Hirth, G., 2005. Newtonian versus non-Newtonian upper Mantle Viscosity: Implications for Subduction Initiation. *Geophys. Res. Lett.*, 32: doi:10.1029/2005GL023457.

Billen, M. I., Hirth, G., 2007. Rheologic controls on slab dynamics. *Geophysics, Geochemistry, Geosystems*, 8: 2007GC001597.

Blackwell, D. D., 2005. Subduction zone backarcs, mobile belts, and orogenic heat: comment. *GSA Today, , Comments and Replies*, 10:1130/10525173(2005)015.

Blankenbach, B., Busse, F., Christensen, U., Cserepes, L., Gunkel, G., Hansen, U., Harder, H., Jarvis, G., Koch, M., Marquart, G., Moore, D., Olson, P., Schmeling, H., Schnaubelt, T., 1989. A benchmark comparison for mantle convection codes. *Geophys. J. Int.*, 98: 23–38.

Bock, G., Kind, R., Rudloff, A., Asch, G., 1998. Shear wave anisoptropy in the upper mantle beneath the Nazca plate in the northern Chile. *J. Geophys. Res.*, 103: 24333–24346.

Borggaard, J., Iliescu, T., Roop., J.P., 2008. An improved penalty method for power-law stokes problem. *Journal of Computational and Applied Mathematics*, doi:10.1016/j.cam.2008.02.002

Bostock, M. G., Hyndman, R. D., Rondenay, S., Peacock, S. M., 2002. An inverted continental Moho and serpentinization of the forearc mantle. *Nature*, 417: 536–538.

Boussinesq, J. V., 1903. Theorie Analytique de la Chaleur, Volume 2. Gauthier-Villars, Paris.

Brdička, M., 1959. Mechanika kontinua, Academia Praha.

Brocher, T. M., Parson, T., Trehu A. M., Snelson, C. M., Fisher, M. A., 2003. Seismic evidence for widespread serpentinized forearc upper mantle along the Cascadia margin. *Geology*, 31: 267–270.

Buttles, J., Olson, P., 1998. A laboratory model of subduction zone anisotropy. *Earth. Planet. Sci. Lett.*, 164: 245–262.

Carlson, R. L., Miller, D. J., 2003. Mantle wedge water contents estimated from seismic velocities in partially serpentinized peridotites. *Geophys. Res. Lett.*, 30: 54.1–54.4.

Christensen, U., 1989. Mantle rheology, constitution, and convection. In: Peltier, W. R. (ed.), Mantle Convection: Plate Tectonics and Global Dynamics, Gordon and Breach, New York, 595–655.

Christensen, U., 1997. The influence of chemical buoyancy on the dynamics of slabs in the transition zone. *J. Geophys. Res.*, 102: 22435–22443.

Cloos, M., 1982. Flow melanges: Numerical modeling and geologic constraints on their origin in the Franciscian subduction complex, California. *Geol. Soc. Am. Bull.*, 93: 330-

345.

Cloos, M., 1993. Lithospheric buoyancy and collisional orogenesis: Subduction of oceanic plateaus, continental margins, island arcs, spreading ridges, and seamounts. *Geol. Soc. Am. Bull.*, 105: 715–737.

Cruciani, C., Carmitani, E., Doglioni, C., 2005. Slab dip vs. lithosphere age: No direct function. *Earth. Planet. Sci. Lett.*, 238: 298–310.

Codina, R., 1993. An iterative penalty method for the finite element solution of the stationary Navier-Stokes equations. *Computer Methods in Apllied Mechanics and Edgineering*, 110: 237–262.

Conder, J. A., 2005. A case for hot slab surface temperatures in numerical viscous flow models of subduction zones with an improved fault zone parameterization. *Phys. Earth Planet. Inter.*, 149: 155–164.

Currie, C. A., Cassidy, J. F., Hyndman, R. D., Bostock, M., G., 2004. Shear wave anisothopy beneath the Cascadia subduction zone and western North American craton. *Geophys. J. Int.*, 157: 341–353.

Currie, C. A., Wang. K., Hyndman R. D., He J., 2004. The thermal effects of steady-state slab-driven mantle flow above a subducting plate: the Cascadia subduction zone and backarc. *Earth. Planet. Sci. Lett.*, 223: 35–48.

Currie, C. A., Hyndman, R., D., 2006. The thermal structure of subductin zone back arcs *J. Geophys. Res.*, 111: doi:10.1029/2005JB004024.

Cuvelier, C., Segal, A., van Steenhoven, A. A., 1986. Finite Element Methods and Navier-Stokes Equations. Reidel Publishing Company, Dordrecht.

Čadek, O., van den Berg, A. P., 1998. Radial profiles of temperature and viscosity in the Earth's mantle inferred from the geoid and lateral seismic structure. *Earth. Planet. Sci. Lett.*, 164: 607–615.

Čadek, O., Ricard, Y., 1992. Toroidal/poloidal energy partitioning and global lithospheric rotation during Cenozoic time. *Earth. Planet. Sci. Lett.*, 109: 621–632.

Čížková, H., van Hunen, J., van den Berg, A., Vlaar, N. J., 2002. The influence of rheological weakening and yield stress on the interaction of slabs with the 670 km discontinuity. *Earth. Planet. Sci. Lett.*, 199: 447–457.

Čížková, H., van Hunen, J., van den Berg, A., 2007. Stress distribution within subducting slabs and their deformation in the transition zone. *Phys. Earth Planet. Inter.*, 161: 202–214.

D'Antonio, M., Kristensen, M. B., 2004. Serpentine and brucite of ultramafic clasts from the South Chamorro Seamount (Ocean Drilling Program Leg 195, Site 1200): inferences for the serpentinization of the Mariana forearc mantle. *Mineralogical Magazine*, 68: 887–904.

Davies, J. H., 1999. Simple analytic model for subduction zone thermal structure. *Geophys. J. Int.*, 139: 823–828.

De Franco, R., Govers, R., Wortel, R., 2007. Numerical comparison of different convergent plate contacts: subduction channel and subduction fault. *Geophys. J. Int.*, 171: 435-450.

de Vahl Davis, G., and Jones, I. P., 1983. Natural convection in a square cavity: A comparison exercise. *Int. J. for Numerical Methods in Fluids*, 3: 227–248.

Dietz, R. S., 1961. Continent and Ocean Basin Evolution by Spreading of the Sea Floor. *Nature*190: 854–857, doi:10.1038/190854a0.

Doglioni, C., Harabaglia, P., Merlini, S., Mongelli, F., Peccerillo, A., Piromallo, C., 1999. Orogens and vlabs vs. their direction of subduction. *Earth Sci. Rev.*, 45: 167–208.

Dziewonski, A. M., Anderson, D. L., Preliminary reference earth model. *Phys. Earth Planet. Inter.*, 25: 297–356.

Eberle, M. A., Grasset, O., Sotin, C., 2002. A numerical study of the interaction between the mantle wedge, subducting slab, and overriding slab. *Phys. Earth Planet. Inter.*, 134: 191–202.

Eiler, J. (ed.), 2003. Inside the Subduction factory, AGU Monograph 138, Washington.

England, P., Engdahl, R., Thatcher, W., 2004. Systematic variation in the depths of slabs beneath arc volcanoes. *Geophys. J. Int.*, 156: 377–408.

Ernst, W. G., 1988. Tectonic history of subduction zones inferred from retrograde blueschist PT paths. *Geology*, 16: 1081–1084.

Ernst, W. G., Maruyama, S., Wallis, S., 1997. Buoyancy-driven, rapid exhumation of ultrahigh-pressure metamorphosed continental crust. *Proc. Natl. Acad. Sci. USA* 94: 9532–9537 .

Escartin, J., Hirth, G., Evans, B., 2001. Strength of slightly serpentinized peridotites: Implications for the tectonics of oceanic lithosphere. *Geology*, 29: 1023–1026.

Fischer, K. M., Fouch, M. J., Wiens, D. A., Boettcher, M. S., 1998. Anisotropy and Flow in Pacific Subduction Zone Back-arcs. *Pure and Applied Geophysics*, 151: 463–475.

Forsyth, D., Uyeda, S., 1975. On the relative importance of the of the driving forces of plate motions. *Geophys. J. R. Astron. Soc.*, 43: 163–200.

Fouch, M. J., Rondenay, S., 2006. Seismic anisotropy beneath stable continental interiors. *Phys. Earth Planet. Inter.*, 158: 292-320.

Fowler, C. M. R., 2005. The Solid Earth: An Introduction to Global Geophysics. Cambridge University Press, Cambridge.

Frohlich, C., 2006. A simple analytical method to calculate the thermal parameter and temperature within subducted lithosphere. *Phys. Earth Planet. Inter.*, 155: 281–285.

Gerya, T. V., Stöckert, B., 2002. Exhumation rates of high pressure metamorhic rocks in subduction channels: The effect of rheology. *Geophys. Res. Lett.*, 29, doi:10.1029/2001GL014307.

Gerya, T. V., Perchuk, L. L., van Reenen, D. D., Smit, C. A., 2000. Two-dimensional numerical modeling of pressure-temperature-time path for exhumation of some granulite

facies terrains in the Precambrian. *J. Geodyn.*, 30: 17–35.

Gerya, T. V., Stöckert, B., Perchuk, A. L., 2002. Exhumation rates of high-pressure mathamorphic rocks in a subduction channel: A numerical simulation. *Tectonics*, 21:doi:10.1029/2002TC001406.

Gerya, T. V., Connoly, J. A., Yuen, D. A., 2008. Why is terrestrial subduction one-sided? *Geology*, 36: 43–46.

Gerya, T. V., Yuen, D. A., 2003. Rayleigh-Taylor instabilities from hydration and melting cold plumes at subduction zones. *Earth. Planet. Sci. Lett.*, 212: 47–62.

Gill, J., 1981. Orogenic Andesites and Plate Tectonics. Springer-Verlag, New York.

Giunchi, C., Ricard, Y., 1999. High-pressure/low-temperature metamorphism and the dynamics of an accreationary wedge. *Geophys. J. Int.*, 136: 620–628.

Godard, G., 2001. Eclogites and their geodynamic interpretation: a history. *J. Geodyn.*, 32: 165–203.

Gorbatov, A., Kostoglodov, V., 1997. Maximum depth of seismicity and thermal parameter of the subducting slab: general empirical relation and its application. *Tectonophysics*, 277: 165–187.

Grevemeyer, I., Kaul, N., Diaz-Naveas, J. L., Villinger, H. W., Ranero, C. R., Reichert, C., 2005. Heat flow and bending-related faulting at subduction trenches: Case studies offshore of Nicaragua and Central Chile. *Earth. Planet. Sci. Lett.*, 236: 238–248.

Guillot, S., Hattori, K. H., de Sigoyer, J., 2000. Mantle wedge serpentinization and exhumation of eclogites: Insight from eastern Ladakh, northern Himalaya. *Geology*, 28: 199–202.

Guillot, S., Hattori, K. H., de Sigoyer, J., Nägler, T., Auzende, A., 2001. Evidence of hydratation of the mantle wedge and its role in the exhumation of eclogites. *Earth. Planet. Sci. Lett.*, 193: 115–127.

Iidaka, T., Obara, K., 1995. Shear-wave polarization anisotropy in the mantle wedge above the subducting Pacific plate. *Tectonophysics*, 249: 53–68.

Han, L., Gurnis, M., 1999. How valid are dynamic models of subduction and convection when plate motions are prescribed? *Phys. Earth Planet. Inter.*, 110: 235–246.

Hanuš, V., Vaněk, J., 1978. Morphology of the andean wadati-benioff zone, andesitic volcanism, and tectonic features of the Nazca plate. *Tectonophysics*, 44: 65–77.

Hanuš, V., Vaněk, J., 1985. Structure of wadati-benioff zones and volcanism produced by the process of subduction. *Tectonophysics*, 112: 51–67.

Heaton, T. H., Kanamori, H., 1984. Seismic potential associated with subduction in the northwestern United States. *BSSA*, 74: 933–941.

Helffrich, G., Wiens, D. A., Vera, E., Barrientos, S., Shore, P., Robertson, S., Adaros, R., 2002. A teleseismic shear-wave splitting study to investigate the mantle flow around South America and implications for plate-driving forces. *Geophys. J. Int.*, 149: F1-F7.

Herman, J., Müntener, O., Scambelluri, M., 2000. The importance of serpentine mylonites for subduction and exhumation of oceanic crust. *Tectonophysics*, 327: 225–238.

Herms, P., 2004. Fluids in a 2 Ga old subduction zone – deduced from eclogite-facies rocks of the Usagaran belt, Tanzania. *Eur. J. Mineralogy*, 14: 361–373.

Hirth, G., Kohlstedt, D., 1996. Water in the oceanic upper mantle: implications for rheology, melt extraction and the evolution of the lithosphere. *Earth. Planet. Sci. Lett.*, 144: 93–108.

Hirth, G., Kohlstedt, D., 2003. Rheology of the upper mantle and the mantle wedge: a view from the experimentalist. In: Eiler, J. (ed.), Inside the Subduction factory, AGU Monograph 138, Washington.

Holmes, A., 1931. Radioactivity and Earth movements, 1932. *Geological Society of Glasgow*, 18: 559–606.

Holmes, A., 1944. Principles of Physical Geology. Ronald Press, New York.

Honda, S., Saito, M., 2003. Small-scale convection under the back-arc occurring in the low viscosity wedge. *Earth. Planet. Sci. Lett.*, 216, 703–715.

Hyndman, R. D., Wang, K., Yamano, M., 1995. Thermal constraints on the seismogenic portion of the southwestern Japan subduction thrust. *J. Geophys. Res.*, 100: 15373–15392.

Hyndman, R. D., Currie, C. A., Mazzotti, S. P., 2005. Subduction zone backarcs, mobile belts, and orogenic heat. *GSA Today*, 15: 4–10.

Hyndman, R. D., Wang, K., 1995. The rupture zone of Cascadia great eartquakes from current deformation and the thermal regime. *J. Geophys. Res.*, 100: 22133–22154.

Hyndman, R. D., Lewis, T. J., 1999. Geophysical consequences of the Cordillera-Craton thermal transition in southwestern Canada. *Tectonophysics*, 306: 397–422.

Hyndman, R. D., Peacock, S. M., 2003. Seprentinization of the forearc mantle. *Earth. Planet. Sci. Lett.*, 212: 417–432.

Ito, E., Katsura, T., 1989. A temperature profile of the mantle temperature zone. *Geophys. Res. Lett.*, 16: 425–428.

Iwamori, H., 1998. Transportation of H_2O and melting in subduction zones *Earth. Planet. Sci. Lett.*, 160: 65–80.

Iwamori, H., 2007. Transportation of H_2O beneath the Japan arcs and its implication for global water circulation. *Chem. Geol.*, 239: 182–198.

Jarrad, R. D., 1986. Relations among subduction parameters. *Rev. Geophys.*, 24: 217–283.

Jacoby, W. R., 2001. Successes and failures in geodynamics: from past to future. *J. Geodyn.*, 32: 3–27.

Jung, H., Katayama, I., Jiang, Z., Hiraga, T., Karato, S., 2006. Effect of water and stress on the lattice-preferred orientation of olivine. *Tectonophysics*, 421: 1–22.

Kameyama, M., Yuen, D. A., Karato, S., 1999. Thermal-mechanical effects of low-

temperature plasticity (the Peierls mechanism) on the deformation of a viscoelastic shear zone. *Earth. Planet. Sci. Lett.*, 168: 159–172.

Kamiya, S., Kobayashi, Y., 2000. Seismological evidence for the existence of serpentinized wedge mantle. *Geophys. Res. Lett.*, 27: 819-822.

Karato, S., 2003. Mapping water content in the upper mantle. In: Eiler, J. (ed.), Inside the Subduction factory, AGU Monograph 138, Washington.

Karato, S., Ogawa, M., 1982. Hight-pressure recovery of olivine: implications for creep mechanism and creep activation volume. *Phys. Earth Planet. Inter.*, 28: 102–117.

Karato, S., Wu, P., 1993. Rheology of the Upper Mantle: A Synthesis. *Science*, 260: 771–777.

Karato, S., Spetzler, H. A., 1990. Defect microdynamics and physical mechanism of seismic wave attenuation and velocity dispersion in the Earth's mantle. *Rev. Geophys.*, 28: 399–421.

Kaufmann, G., Lambeck, K., 2002. Glacial isostatic adjustment and the radial viscosity profile from inverse modeling. *J. Geophys. Res.*, 107, doi:10.1029/2001JB000941.

Kincaid, C., Hall, P. S., 2003. Role of back arc spreading in circulation and melting at subduction zones. *J. Geophys. Res.*, 108: doi:10.1029/2001JB001174.

King, S. D., 2001. Subduction zones: observations and geodynamic models. *Phys. Earth Planet. Inter.*, 127: 9–24.

Kirby, S., Stein, S., Rubie, D., Okal, E., 1996. Deep earthquakes and metastable phase changes in subducting oceanic lithosphere. *Rev. Geophys.*, 34: 261–306.

Kneller E. A., van Keken P. E., Karato S., Park J., 2005. B-type olivine fabric in the mantle wedge: Insights from high-resolution non-Newtonian subduction zone models. *Earth. Planet. Sci. Lett.*, 237: 781–797.

Kneller E. A., van Keken P. E., Katayama I., Karato S., 2007. Stress, strain, and B-type olivine fabric in the fore-arc mantle: Sensitivity tests using high-resolution steady-state subduction zone models. *J. Geophys. Res.*, 112, B004406, doi: 10.1029/2006JB004544.

Kneller, E. A., van Keken, P. E., 2007. Trench-parallel flow and seismic anisotropy in the Mariana and Andean subduction systems. *Nature*, 450: 1222–1225.

Křížek, M., and Neittaanmäki, P., 1990. Finite Element Approximation of Variational Problems and Application. Longman, New York.

Kohlstedt, D. L., evans, B., Mackwell, S. J., 1995. Strength of the lithosphere: Constrains imposed by laboratory expemiments. *J. Geophys. Res.*, 100: 17587–17602.

Koulakov, I., Sobolev, S. V., asch G., 2006. P- and S-velocity images of the lithosphere-asthenosphere system in the Central andes from local-source tomographic inversions. *Geophys. J. Int.*, 167: 106–126.

Kukačka M., Matyska C., 2004. Influence of the zone of weakness on dip angle and shear heating of subducted slab. *Phys. Earth Planet. Inter.*, 141: 243–252.

Lassak, T. M., Fouch, M. J., Hall, C. E., Kaminski, E., 2006. Seismic characterization of mantle flow in subduction systems: Can we resolve a hydrated mantle wedge? *Earth. Planet. Sci. Lett.*, 243: 632–649.

Leat, P. T., Larter, R. D., 2003. Intra-oceanic subduction systems: introduction. In: Leat, P. T., Larter, R. D. (eds.), Intra-Oceanic Subduction Systems: Tectonic and Magmatic Processes, Geological Society London, London.

Lefton, L., Wei, D., 2001. A penalty method for approximations of the stationary power-law stokes problem. *Electronic Journal of Differential Equations*, 7: 1–12.

Le Pichon, X. J., Francheteau, J., Bonin, J., 1973. Plate Tectonics. Elsevier, New York.

Le Pichon, X., Henry, P., Goffe, B., 1997. Uplift of Tibet: from eclogites to granulites – implications for the Andean Plateau and the Variscan belt. *Tectonophysics*, 273: 57–76.

Lewis, T., Bentkowski, W. H., Davis, E. E., Hyndman, R. D., Souther, J. G., Wright, J., 1988. Subduction of the Juan de Fuca plate: thermal consequences. *J. Geophys. Res.*, 93: 15207–15225.

Lin C.-H., 2000. Thermal modeling of continental subduction and exhumation constrained by heat flow and seismicity in Taiwan. *Tectonophysics*, 324: 189–201.

Liu, Z., Bird, P., 2006. Two-dimensional and three-dimensional finite element modelling of mantle processes beneath central South Island, New Zealand. *Geophys. J. Int.*, 165: 1003–1028.

Long, M. D., van der Hilst, R. D., 2005. Upper mantle anisotropy beneath Japan from shear wave splitting. *Phys. Earth Planet. Inter.*, 151: 206–222.

Long, M. D., van der Hilst, R., 2006. Shear wave splitting from local events beneath the Ryukyu arc: Trench-parallel anisotropy in the mantle wedge. *Earth. Planet. Sci. Lett.*, 155: 300-312.

Long, M. D., Hager, B. H., de Hoop, M. V., van der Hilst, R. D., 2007. Two-dimensional modelling of subduction zone anisotropy with application to southwestern Japan. *Geophys. J. Int.*, 170: 839–856.

Manea, V. C., Manea, M., Kostoglodov, V., Currie, C. A., Sewell, G., 2004. Thermal structure, coupling and metamorphism in the Mexican subduction zone beneath Guerrero. *Geophys. J. Int.*, 158: 775–784.

Manea V. C., Manea M., Kostoglodov V., Sewell G., 2005. Thermo-mechanical model of the mantle wedge in Central Mexico subduction zone and a blob tracing approach for the magma transport. *Phys. Earth Planet. Inter.*, 149: 165–186.

Manea, V., Gurnis, M., 2007. Subduction zone evolution and low viscosity wedges and channels. *Earth. Planet. Sci. Lett.*, 264: 22–45.

Marota, A. M., Mongeli, F., 1998. Flexure of subducted slabs. *Geophys. J. Int.*, 132: 701-711.

Matyska, C., 1996. Variational principles for the momentum equation of the mantle convection whit Newtonian and power-law rheologies. *Geophys. J. Int.*, 126: 281–286.

Matyska, C., Yuen. D. A., 2007. Lower-mantle material properties and convection models of multiscale plumes. *Plates, Plumes and Planetary Processes*, 430: 137–163.

McKenzie, D., 1969. Speculations on the consequences and causes od plate motion. *Geophys. J. R. Astr. Soc.*, 18: 1–32.

Meza-Figueroa, D., Ruiz, J., Talavera-Mendoza, O., Ortega-Gutierrez, F., 2003. Tectonometamorphic evolution of the Acatlan Complex eclogites (southerm Mexico). *Can. J. Earth Sci.*, 40: 27–44.

Mibe, K., Fujii, T., Yashuda, A., 1999. Control of the location of the volcanic front in island arcs by aqueous fluid connectivity in the mantle wedge. *Nature*, 401: 259–262.

Mizukami, T., Wallis, S. R., Yamamoto, J., 2004. Natural examples of olivine lattice preferred orientation patterns with a flow-normal *a*-axis maximum. *Nature*, 427: 432–436.

Mueller, R. D., Roest, W. R., Royer, J.-Y., Gahagan, L. M., Scalter, J. G., 1997. Digital isochrons of the world oceans. *J. Geophys. Res.*, 102, 3211–3214.

Molnar, P., Freedman, D., Shih, J. S. F., 1979. Length of intermediate and deep seismic zones and temperatures in downgoing slab of the lithosphere. *Geophys. J. Int.*, 56: 41-54.

Nakajima, J., Hasegawa, A., 2004. Shear-wave polarization anizotropy and subduction-induced flow in the mantle wedge of northern Japan. *Earth. Planet. Sci. Lett.*, 225: 365–377.

Nakajima, J., Takei, Y., Hasegawa, A., 2005. Quantitative analysis of the inclined low-velocity zone in the mantle wedge of northeastern Japan: A systematic change of melt-filled pore shapes with depth and its implications for melt migration. *Earth. Planet. Sci. Lett.*, 234: 59–70.

Nicholson, T., Bostock, M., Cassidy, J. F., 2006. New constraints on subduction zone structure in northern Cascadia. *Geophys. J. Int.*, 161: 849–859.

Oliver, J., Isacks, B., Deep earthquake zones, anomalous structure in the upper mantle, and in the lithosphere. *J. Geophys. Res.*, 72: 4259–4275.

Ono, S., Mibe, K., Yoshino, T., 2002. Aqueous fluid connectivity in pyrope aggregates: water transport into the deep mantle by a subducted oceanic crust without any hydrous minerals. *Earth. Planet. Sci. Lett.*, 203, 895–903.

Peacock, S. M., 1993. Large-scale hydration of the lithosphere above subducting slabs. *Chem. Geol.*, 108: 49–59.

Peacock, S. M., Rushmer, T., Thompson, A. B., 1994. Partial melting of subducting oceanic crust. *Earth. Planet. Sci. Lett.*, 121: 227–244.

Peacock, S. M., 1996. Thermal and petrlogic structure of subduction zones. In: Bebout, G., School, D., Kirby, S. (eds.), Subduction: Top to Bottom, AGU Monograph 96, AGU Washington, 119–133.

Peacock S. M., van Keken P. E., Holloway S. D., Hacker B. R., Abers G. A., Fergason R. L., 2005. Thermal structure of the Costa Rica – Nicaragua subduction zone. *Phys. Earth*

Planet. Inter., 149: 187–200.

Peyton, V., Levin, V., Park, J., Brandon, M., Lees, J., Gordeev, E., Ozerov, A., 2001. Mantle flow at a Slab edge: Seismic Anisotropy in the Kamchatka region. *Geophys. Res. Lett.*, 28: 379–382.

Platt, J. P., 1993. Exhumation of high-pressure rocks: a review of concepts and processes. *Terra Nova*, 5: 119–133.

Ponko, S. C., Peacock, S. M., 1995. Thermal modeling of the southern alaska subductuion zone: Insight into petrology of the subducting slab and the overlying mantle wedge. *J. Geophys. Res.*, 100: 22117–22128.

Pratt, D., 2000. Plate Tectonics: A Paradigm Under Threat. *J. Scient. Explorations*, 14: 307–352.

Raimbourg, H., Jolivet, L., Leroy, Y., 2007. Consequences of progressive eclogitization on crustal exhumation, a mechanical study. *Geophys. J. Int.*, 168: 379–401.

Ranali, G., 1998. Inferences on mantle rheology from creep Laws. *Georeseach Forum*, 3-4: 323–340.

Raleigh, C. B., 1967. Tectonic Implications of Serpentinite Weakening. *Geophys. J. Int.*, 14: 113–118.

Ricard, Y., Doglioni, C., Sabadini, R., 1991. Differential rotation between lithosphere and the mantle: a consequence of lateral viscosity variations. *J. Geophys. Res.*, 96: 8407–8415.

Rhodes, M., Davies, J. H., 2001. Tomographic imaging of multiple mantle plumes in the uppermost lower mantle. *Geophys. J. Int.*, 147: 88–92.

Rudnick, R. L., McDonough, W. F., O'Connell, R. J., 1998. Thermal structure, thickness and composition of continental lithosphere. *Chem. Geology*, 145: 395–411.

Rüpke, L. H., Morgan, J. P., Hort, M., Connolly, J. A. D., 2004. Serpentine and the subduction zone water cycle, 2004. *Earth. Planet. Sci. Lett.*, 223: 17–34.

Russo, R. M., Silver, P. G., 1994. Trench-Parallel Flow Beneath the Nazca Plate from Seismic Anisotropy. *Science*, 263: 1105–1111.

Schmidt, M. W., Poli, S., 1998. Experimentally based water budgets for dehydrating slabs and consequences for arc magma generation. *Earth. Planet. Sci. Lett.*, 163: 361–379.

Schubert, G., Turcotte, D. L., Olson, P., 2001. Mantle Convection in Earth and Planet. Cambridge University Press, Cambridge.

Schurr, B., Asch, G., Rietbrock, A., Trumbull, R., Haberland, C., 2003. Complex patterns of fluid and melt transport in the central Andean subduction zone revealed by attenuation tomography. *Earth. Planet. Sci. Lett.*, 237: 781–797.

Schwartz, S., Allemand P., Guillot, S., 2001. Numerical model of the effect of serpentinites on the exhumation of eclogitic rocks: insight from the Monviso ophiolitic massif (Western Alps). *Tectonophysics*, 342: 193–206.

Snider-Pellegrini, A., 1858. La Creation et ses Mysteres devoiles. Franck et Dentu, Paris.

Springer, M., Förster, A., 1998. Heat-flow density across the Central Andean subduction zone. *Tectonophysics*, 291: 123–139.

Stachnik, J. C., Abers, G. A., Christensen, D. H., 2004. Seismic attenuation and mantle wedge temperatures in the Alaska subduction zone. *J. Geophys. Res.*, 109, B10304, doi: 10.1029/2004JB003018.

Stein, C., Stein, S., 1992. A model for the global variation in oceanic depth and heat flow with lithospheric age. *Nature*, 359: 123–128.

Stein, S., Stein, C., 1996. Thermo-mechanical evolution of oceanic lithosphere: implications for the subducution process and deep earthquakes. In: Bebout, G., School, D., Kirby, S. (eds.), Subduction: Top to Bottom, AGU Monograph 96, AGU Washington, 1–17.

Stern, R. J., 2002. Subduction zones. *Rev. Geophys.*, 40(4), 1012, doi:10.1029/2001RG000108.

Stöckert, B., Gerya, T. V., 2002. Pre-collisional high pressure metamorthism and nappe tectonics at active continental margins: a numerical solution. *Terra Nova*, 17: 102–110.

Špičák, A., Hanuš, V., Vaněk J., 2004. Seismicity pattern: an indicator of source region of volcanism at convergent plate margins. *Phys. Earth Planet. Inter.*, 141: 303–326.

Tackley, P. J., 2000a. Mantle Convection and Plate Tectonics: Toward and Integrated Physical and Chemical Theory. *Science*, 288: 10.1126/science.288.5473.2002.

Tackley, P. J., 2000b. Self-consistent generation of tectonic plates in time-dependent, three-dimensional mantle convection simulations 1. Pseudoplastic yielding. *Geophysics, Geochemistry, Geosystems*, 1: 2000GC000043.

Tackley, P. J., 2000c. Self-consistent generation of tectonic plates in time-dependent, three-dimensional mantle convection simulations 2. Strain weakening and asthenosphere. *Geophysics, Geochemistry, Geosystems*, 1: 2000GC000044.

Tatsumi, Y., 1986. Formation of the volcanic front in subduction zones. *Geophys. Res. Lett.*, 17: 717–720.

Taylor, B., Martinez, F., 2003. Back-arc basin systematics. *Earth. Planet. Sci. Lett.*, 210: 481–497.

Temam, R., 2001. Navier-Stikes equations, theory and numerical analysis. Americal Mathematical Society, Chelsea.

Trubitsyn, V. P., Rykov, V. V., Jacoby, W. R., 1999. A self-consistent 2-D model for the dip angle of mantle downflow beneath an overriding continent. *J. Geodyn.*, 28: 215–224.

Tsujimori, T., Matsumoto, K., Wakabayashi, J., Liou, J. G., 2006. Franciscan eclogite revised: Reevaluation of the P-T evolution of tectonics blocks from Tiburon Peninsula, California, U. S. A. *Mineralogy and Petrology*, 88: 243–267.

Tsujimori, T., Sisson, V. B., Liou, J. G., Harlow, G. E., Sorensen, S. S., 2006. Very-low-temperature record of the subduction process: A review of worldwide lawsonite eclogites. *Lithos*, 92: 609–624.

Tosi, N., 2008. Numerical modeling of present-day mantle convection. PhD thesis, Prague.

Ulmer, P., Trommsdort, V., 1995. Serpentine stability to mantle depths and subduction-related magmatism. *Science*, 268: 858–861.

Uyeda, S., 1986. Facts, ideas and open problems in trench-arc-backarc systems. In Wezel, F. C. (ed.), The origin of arcs, Elsevier.

van der Hilst, R. D., 1995. Complex morphology of subducted lithosphere in the mantle beneath the Tonga trench. *Nature*, 374: 154–157.

van der Hilst, R. D., Widiyantoro, S., Engdahl, E. R., 1997. Evidence for deep mantle circulation from global tomography. *Nature*, 386: 578–584.

van Hunen, J., van der Berg, A. P., Vlaar, N. J., 2000. A thermo-mechanical model of horizontal subduction below an overriding plate. *Earth. Planet. Sci. Lett.*, 182: 157–169.

van Hunen, J., van der Berg, A. P., Vlaar, N. J., 2004. Various mechanisms to induce present-day shallow flat subduction and implications for the younger Earth: a numerical parameter study. *Phys. Earth Planet. Inter.*, 146: 179–194.

van Keken, P. E., 1993. Numerical Modelling of Thermochemically Driven fluid flow With Non-Newtonian Rheology. PhD thesis, Utrecht.

van Keken, P. E., 2003. The structure and dynamics of the mantle wedge, *Earth. Planet. Sci. Lett.*, 215: 323–338.

van Keken P. E., Kiefer B., Peacock S. M., 2002. High-resolution models of subduction zones: Implications for mineral dehydration reactions and the transport of water into the deep mantle. *Geophysics, Geochemistry, Geosystems*, 3: 2001GC000256.

Vine, F. J., Matthews, D. H., 1963. Magnetic Anomalies Over Oceanic Ridges. *Nature*, 199: 947–949, doi:10.1038/199947a0.

Wadati, K., 1935. On the activity of deep-focus earthquakes in the Japan islands and neighbourhoods. *Gephysical magazine*, 8: 305–325.

Wang, K., Hyndman, R. D., Yamano, M., 1995. Thermal regime of the Southwest Japan subduction zone: effects of age history of the subducting plate. *Tectonophysics*, 248: 53–69.

Wannamaker, P. E., Brooker, J. R., Jones, A. G., Chave, A. D., Filloux, J. H., Waff, H. S., Law, L. K., 1989. Resistivity cross section through the Juan de Fuca subduction system and its tectonic implications. *J. Geophys. Res.*, 94: 14127–14144.

Wegener, A., 1929. Die Entstehung der Kontinente und Ozeane. Friedr. Vieweg & Sohn Akt.-Ges., Braunschweig.

Wenner, D. B., Taylor Jr., H. D., 1971. Temperatures of serpentinization of ultramafic rocks based on O^{18}/O^{16} fractination between coexising serpentinite and magnetite. *Contributions to Mineralogy and Petrology*, 32(3): 165–185.

Wunder, B., Schreyer, W., 1997. Antigorite: High-pressure stability in the system MgO–SiO_2–H_2O(MSH). *Lithos*, 41: 213–227.

Yoshioka, S., Murakami, K., 2007. Temperature distribution of the upper surface of the subducted Philippine Sea Plate along the Nankai Trough, southwest Japan, from a three-dimensional subduction model: relation to large interplate and low-frequency earthquakes. *Geophys. J. Int.*, 171: 302–315.

Zeytounian, R. K., 2003. Joseph Boussinesq and his approximation: a contemporary view. *Comptes Rendus Mecanique*, 331: 575–586.

Zhang, S., Karato, S. I., 1995. Lattice preferred orientation of olivine aggregates deformed in simple shear. *Nature*, 375: 774–777.

Zhao, D. P., 2001. Seismological structure of subduction zones and its implications for arcs magmatism and dynamics. *Phys. Earth Planet. Inter.*, 127: 197–214.

Zhao, D., Hasegawa, A., 1993. P wave tomographic imaging of the crust and upper mantle beneath Japan Islands. *J. Geophys. Res.*, 98: 4333–4353.

Zhao, D. P., Kayal, J. R., 2000. Impact of seismic tomography on earth sciences. *Curr. Sci.*, 79: 1208–1214.

Zhao, D., Hasegawa, A., Kanamori, H., 1994. Deep structure of japan subduction zone as derived from local, regional, and teleseismic events. *J. Geophys. Res.*, 99: 22313–22329.

Zhao, D., Xu, Y., Wiens, D. A., Dorman, L., Hildebrand, J., Webb, S., 1997. Depth Extent of the Lau Back-Arc Spreading Center and Its Relation to Subduction Processes. *Science*, 278: 254–257.

Ziagos, J. P., Blackwell, D. D., Moser, F., 1985. Heat Flow in Southern Mexico and the Thermal Effects of Subduction. *J. Geophys. Res.*, 90: 5410–5420.

Zimmerman, M. E., Kohlstedt, D. L., 2004. Rheological properties of partially molten Lherzolite. *J. Petrol.*, 45: 275–298.

Zlatev, Z., Wasniewski, J., Schaumburg, K., 1981. Y12M, Solution of Large and Sparse System of Linear Algebraic Equations, Lecture Notes in Computer Science, Volume 121. Springer.